

**MULTIDISCIPLINARY ANALYSIS OF
CLOSED, NONPLANAR WING
CONFIGURATIONS FOR TRANSPORT
AIRCRAFT**

**ÉTUDE MULTIDISCIPLINAIRE DE
CONFIGURATIONS D'AILES NON
PLANES POUR AÉRONEFS DE
TRANSPORT**

A Thesis Submitted to the Division of Graduate Studies
of the Royal Military College of Canada
by

Stephen Arthur Andrews

In Partial Fulfillment of the Requirements for the Degree of
Doctor of Philosophy, Mechanical Engineering

April, 2016

© This thesis may be used within the Department of National Defence
but copyright for open publication remains the property of the author.

Acknowledgements

I would like to thank my supervisor, Dr. Ruben Perez, for the guidance he has given me throughout my studies. I have benefited immensely from the breadth and depth of his technical experience. I would also like to thank my parents for their support throughout my many years of schooling. My wife, Madison, has been a constant source of encouragement. Thank you for all the support and advice you have provided over the years we have been together.

Abstract

A multidisciplinary study of an unconventional aircraft configuration was undertaken to determine if such a design could decrease the environmental impact of civil air transportation through fuel burn improvements for given missions. The specific configuration examined was a box-wing. This is a nonplanar wing design where two parallel wings with some degree of streamwise separation were connected at their tips by a vertical wing segment. The box-wing design differs from a conventional aircraft in three key areas: it has the lowest induced drag of any wing design with the same projected area; it can achieve longitudinal stability without a horizontal tail; and the wings form a statically indeterminate truss structure. These three characteristics lead to improved performance in the respective disciplines of aerodynamics, stability and structures. For this reason, the box-wing has been investigated as a possible transport aircraft in several previous studies, each focusing on these disciplines independently.

Trends which improved the performance in one discipline, however, could decrease the performance of the others. A multidisciplinary analysis was required to resolve these interactions and understand the trends which led to reduced fuel consumption for a box-wing design. Novel models for predicting the aerodynamic performance, static longitudinal stability and structural weight of a box-wing aircraft were developed for such an analysis. Optimal box-wing designs were identified, which were compatible with existing transport aircraft certification requirements and operational guidelines. These designs were compared against optimized conventional aircraft to determine what advantage the box-wing configuration possessed.

These findings showed both the interactions between the three key disciplines of aerodynamics, stability and structures, as well as the effect which certification and operational constraints had on the design. Unconventional designs are critical to achieve the fuel burn reductions sought in the next generation of aircraft. The rigorous comparison made between box-wing and conventional configurations showed whether such a design should be pursued in the development of future transport aircraft. Understanding how the constraints and design choices affect a box-wing's performance helped identify alternate missions which best take advantage of this unconventional design.

Résumé

Une étude multidisciplinaire d'une configuration d'aile d'aéronef non-conventionnelle fut entreprise afin de déterminer s'il était possible de réduire la consommation de carburant requise pour entreprendre certains profils de vols. La configuration d'ailes sélectionnée pour ce projet était celle d'ailes en anneau, une configuration similaire à celle d'un avion biplan où les extrémités d'ailes horizontales sont rejointes par des segments d'ailes verticaux. Ce type de configuration se démarque des ailes conventionnelles par les trois principes suivants: la traînée par unité de surface induite est moindre que toutes autres configurations d'ailes conventionnelles, la présence d'une telle configuration élimine la nécessité des gouvernes de profondeurs et les ailes en anneaux forment une structure hyperstatique pour laquelle l'amélioration structurelle peut résulter dans la réduction du poids structurel. Ces trois facteurs ont le potentiel de produire de nettes améliorations dans les performances aérodynamiques et en stabilité ainsi que des réductions du poids structurel. Pour ces raisons, plusieurs scientifiques ont déjà poursuivi des études ciblées sur ces avancements potentiels de performance.

Malgré qu'il a été démontré avec succès que certains modèles peuvent en fait améliorer certains aspects de la performance, aucun des modèles d'ailes en anneau proposés à date ont su démontrer une amélioration de performance globale, pour les trois principes mentionnés ci-haut. Ainsi, ce projet a utilisé une étude multidisciplinaire avec l'objectif premier de produire un modèle structurel d'ailes en anneau possédant le potentiel d'amélioration de performance sur l'ensemble des trois principes.

De nouveaux modèles numériques innovants permettant l'amélioration de la performance aérodynamique, la stabilité statique longitudinale ainsi qu'une réduction du poids structurel de l'ensemble d'aile ont été développés avec succès. Ces modèles sont compatibles avec les normes et certifications existantes ainsi qu'avec les standards opérationnels pour les aéronefs de transport. De plus, ces modèles numériques ont été comparés avec des configurations d'ailes conventionnelles optimisées afin d'identifier et de quantifier leurs avantages. Les résultats de cette étude ont démontré que tout en respectant les contraintes opérationnelles et les besoins de certification, les modèles développés pouvaient en fait accroître la performance selon les trois critères mentionnées. Ces résultats démontrent que l'utilisation de configurations non-conventionnelles offre un niveau amélioré de performance pour de nouvelles configurations potentielles d'aéronefs. Grâce aux améliorations en performance, cette étude a aussi identifié de nouveaux types de missions de vols pour lesquelles les ailes en forme d'anneau pourraient être avantageuses.

Statement of Contributions

Developed novel engineering analysis methods

Two unique analysis methods for box-wing aircraft were developed. Chapter 3 used a unique modification of existing downwash models to account for two large interacting lifting surfaces. Additionally, the method developed in Chapter 5 to predict wing weight using a fully stressed aerofoil conforming cross section was a novel formulation and was applicable to both cantilevered and statically indeterminate wing structures.

Highlighted the interactions between static stability and aerodynamic performance

The parametric analysis in Chapter 4 showed that the aerodynamic penalty caused by static longitudinal stability requirements was negligible for box-wing designs with large streamwise and vertical separation between the wings. This analysis also identified trends in box-wing geometry which led to significant aerodynamic penalties when static longitudinal stability constraints were enforced.

Identified a design conflict between aerodynamic performance and structural weight of box-wings

The analysis of box-wing structures in Chapter 5 showed that trends which decrease wing weight also decreased aerodynamic performance, leading to a previously unexamined conflict between these disciplines for this unconventional wing configuration.

Performed a rigorous comparison of box-wing and conventional aircraft for regional-jet missions

Chapters 6 and 7 presented a multidisciplinary analysis of box-wings for different regional transport aircraft missions. This analysis showed how operational constraints and design requirements limited the performance of the box-wing aircraft. It also showed the trends in the design of a box-wing aircraft which led to superior performance relative to existing designs and identified missions best suited to the box-wing configuration.

Co-authorship statement

This thesis contains work which had been previously published by the author. The analysis and results shown in Chapter 4 were first presented by Andrews and Perez [1]. S. Andrews, performed the parametric study and analysed the results. S. Andrews wrote the paper, R. Perez advised on the project and edited the paper. The model developed in Chapter 5 and some of the results were first published by Andrews, Perez and Wowk [2]. S. Andrews developed the wing weight model as a modification to existing code provided by R. Perez. D. Wowk advised on the formulation of the model. S. Andrews wrote the paper and D. Wowk and R. Perez edited the paper.

Contents

Acknowledgements	ii
Abstract	iii
Résumé	iv
List of Tables	xi
List of Figures	xii
Nomenclature	xv
1 Introduction	1
1.1 Next generation aircraft configurations	2
1.2 Structure of the thesis	7
2 Literature Review	8
2.1 Box-wing aerodynamic performance	8
2.2 Box-wing stability and control	15
2.3 Box-wing structural design	18
2.4 Aircraft configuration issues	24
2.5 Other applications of closed nonplanar wings	25
2.6 Outstanding research questions	25
3 Analytic Model of Box-Wing Static Stability	26
3.1 Development of the model	27
3.1.1 Dual-wing geometry	27
3.1.2 Reference quantities	27
3.1.3 Steady, level flight equations	29
3.1.4 Effector model	30
3.1.5 Downwash model	30

3.1.6	Static longitudinal stability	31
3.1.7	Trimmed performance	32
3.1.8	Determining wing installation angles	34
3.1.9	Off-design performance	34
3.1.10	Verification	35
3.2	Parametric study	35
3.3	Longitudinal stability	40
3.3.1	Simplified stability model	40
3.3.2	Implications of the simplified model	42
3.4	Summary	46
4	Parametric Analysis of Box-Wing Stability and Performance	48
4.1	Design of the parametric study	48
4.2	Optimization problem	52
4.2.1	Optimizers	52
4.3	Results	53
4.3.1	Reference wing	53
4.3.2	Parametric study	55
4.3.3	Wing loading	59
4.4	Summary	61
5	Wing Weight Estimation for Box-Wing Configurations	62
5.1	Existing wing weight models	63
5.2	Fully stressed algorithm	64
5.2.1	Structural model	66
5.2.2	Aerodynamic model	67
5.2.3	Fully stressed hexagonal cross section	67
5.2.4	Allowable stresses	72
5.2.5	Secondary weights	72
5.2.6	Numerical details	73
5.3	Comparison of conventional aircraft weights	74
5.4	Details of box-wing internal structures	75
5.5	Other structural concerns	80
5.5.1	Aeroelasticity	80
5.5.2	Panel buckling	80
5.6	Comparison of box-wings to conventional	80
6	Multidisciplinary Aircraft Design Problem	82
6.1	Multidisciplinary analysis procedure	83
6.2	Disciplinary models	86
6.2.1	Geometry	86

6.2.2	Payload	87
6.2.3	Mission	88
6.2.4	Aerodynamic model	89
6.2.5	Aerofoil performance model	91
6.2.6	Aerodynamic meta-model	92
6.2.7	Performance	93
6.2.8	Propulsion	93
6.2.9	Fuel allocation	93
6.2.10	Wing structure	95
6.2.11	Weights	95
6.2.12	Centre of gravity and inertia	96
6.2.13	Stability	97
6.2.14	Landing gear	99
6.3	Test Cases	100
6.3.1	Variables	100
6.3.1.1	Box-wing analysis	101
6.3.1.2	Baseline aircraft analysis	103
6.3.2	Constraints	104
6.3.2.1	Exclusive box-wing constraints	105
6.3.3	Optimization algorithm	107
7	Comparison of Conventional and Box-Wing Aircraft	108
7.1	Comparison of reference aircraft to published results	108
7.2	Comparison of box-wing and conventional aircraft	109
7.2.1	Aerodynamics	116
7.2.2	Mission performance	120
7.2.3	Structures	124
7.2.4	Stability and control	125
7.3	Active variable bounds	126
7.3.1	Aspect ratio	126
7.3.2	Engine location	127
7.3.3	Wing leading edge station	127
7.4	Dominant constraints	127
7.4.1	Fuel volume	127
7.4.2	Takeoff constraints	129
7.5	Changes to make the box-wing preferable	129
8	Conclusions	131
	Bibliography	134

Appendices	144
A Model Validation Cases	145
A.1 Analytic model verification	145
A.2 Aerodynamic model validation	148
A.2.1 Mignet <i>pou-du-ciel</i>	148
A.2.2 NASA joined-wing research model	148
A.2.3 NASA supercritical-wing transport model	153
A.2.4 NASA span-loader aircraft in ground effect	157
A.3 Aerofoil model validation	160
A.3.1 NACA 6 series aerofoil	160
A.3.2 Reynolds number dependent polar	162
A.4 Weight model validation	162
B Curriculum Vitae	164

List of Tables

3.1	Reference aircraft characteristics	36
3.2	Reference aerofoil section properties	36
3.3	Aft wing elevator attributes	37
4.1	Ranges of the parameters used in the study	49
4.2	Variable bounds and initial values for the optimization problem	53
4.3	Properties of best and worst optimized box-wing designs	57
5.1	Numerical parameters for the structural analysis	74
5.2	Reference aircraft data	75
5.3	Comparison of wing weight between a cantilevered wing and various box-wing designs	81
6.1	Weight categories	96
6.2	Mission specifications	100
6.3	Design variable names and bounds for the box-wing problem	102
6.4	Design variable names and bounds for the baseline aircraft problem	104
6.5	Constraints common to baseline and box-wing aircraft	106
6.6	Design specific constraint bounds	107
7.1	Comparison of multidisciplinary optimization results with published data for baseline reference aircraft	109
7.2	Variables defining the optimized designs of the two baseline aircraft	110
7.3	Comparison of conventional (CRJ) and box-wing (NPL) aircraft for the 200- and 900-class mission	111
7.4	Variables defining the optimal designs for the two box-wing aircraft	113
7.5	Comparison of optimized 200-class box-wing and baseline aircraft with various structural cases	124
7.6	Comparison of a 900-class CRJ and box-wing aircraft with and without the fuel volume constraint.	128

List of Figures

1.1	Comparison of emission reduction strategies.	2
1.2	Unconventional aircraft concepts.	4
1.3	Nonplanar wing configurations.	6
2.1	Box-wing geometric parameters.	9
2.2	The Phillips multiplane.	10
2.3	Loading for minimum induced drag of a box-wing design.	11
2.4	Induced drag of various multiplane configurations.	12
2.5	Comparison of lift-to-drag ratio for monoplanes, biplanes and box-wings	13
2.6	Variation of fore to aft lift ratio as a function of aerodynamic parameters of the transonic biplane.	16
2.7	Truss plane for a joined-wing aircraft.	19
2.8	Effect of various operation constraints on the Direct Operating Cost (DOC)	21
2.9	Comparison of the structure of joined-wings and box-wings.	22
3.1	Dual-wing aircraft geometry.	28
3.2	Pressure distribution on a NACA23012 aerofoil.	37
3.3	Carpet plot of the parametric study results at cruise conditions.	38
3.4	Variation of the downwash function.	42
3.5	Effects of area ratio on the static margin and the sensitivity of static margin to stagger.	46
4.1	Representative box-wing geometries.	51
4.2	Geometry and loading of the planar reference wing.	54
4.3	Parametric study of box-wing geometry.	56
4.4	Sensitivity of the induced drag of a box-wing to changes in the relative lift force of the fore wing.	58
4.5	Loading of a box-wing configuration with a high lift-to-drag ratio.	60

5.1	Alternate wing-box internal structure idealizations.	65
5.2	Flowchart for the fully stressed structural weight prediction algorithm.	66
5.3	Details of the discretization of a typical cantilevered wing.	68
5.4	Details of the aerofoil conforming boom and skin hexagon.	68
5.5	Summary of validation data	76
5.6	Details of box-wing structure	79
6.1	Aircraft design analysis procedure for conventional and box-wing aircraft	85
6.2	Planform geometry of the box-wing aircraft showing the location of high lift devices.	87
6.3	Three-view drawings of the Bombardier CRJ-200 aircraft	88
6.4	Payload location for the baseline and box-wing aircraft.	89
6.5	Regional jet mission specification.	89
6.6	Examples of pyVORLIN discretization.	91
6.7	Performance map of a turbofan engine with the same thrust and bypass ratio as the CF34-3B1.	94
6.8	Example of fuel tanks placed in the fore and aft wings of a box-wing aircraft.	95
6.9	Forces acting on baseline aircraft during takeoff rotation.	98
6.10	Critical landing gear geometry.	99
7.1	Comparison of major performance metrics of the 200- and 900-class box-wings, relative to conventional designs	112
7.2	Comparison of optimized baseline and box-wing aircraft geometries	115
7.3	Sky-maps showing the Mach-lift-to-drag ratio of both aircraft sizes	117
7.4	Comparison of drag forces and drag coefficients of the box-wing to the baseline aircraft	118
7.5	Details of box-wing performance throughout the missions.	122
7.6	Sky maps showing the specific air range for both aircraft sizes. . .	123
7.7	Static margin relative to the value when out of ground effect . . .	126
A.1	Comparison of the current analytical aircraft stability model to the model of Phillips	147
A.2	Pitching moment of the Mignet <i>pou-du-ciel</i>	149
A.3	NASA joined-wing research models	150
A.4	NASA JW1 aerodynamic data	151
A.5	NASA JW3 aerodynamic data	152
A.6	NASA supercritical-wing transport research model.	154
A.7	NASA supercritical wing transport model, cruise aerodynamic data.	155

A.8 NASA supercritical wing transport model, takeoff aerodynamic data.156
A.9 NASA span-loader research model 157
A.10 NASA span-loader aircraft, lift coefficient in and out of ground
effect with and without flaps deployed. 159
A.11 Comparison of experimental and VGK results for an aerofoil 161
A.12 Example of Reynolds number dependent polar results. 162
A.13 Test of the pyACDT weight prediction model. 163

Nomenclature

Dimensionless Groups	
C_D	Total aircraft drag [-]
$C_{D,int}$	Interference drag [-]
C_{D_p}	Aircraft parasitic drag [-]
C_{D_i}	Aircraft induced drag [-]
C_{D_w}	Aircraft compressibility drag [-]
$C_{d_{p0}}$	Constant aerofoil section drag [-]
$C_{d_{p1}}$	Linear aerofoil section drag [-]
$C_{d_{p2}}$	Parabolic aerofoil section drag [-]
C_L	Aircraft lift [-]
C_l	Aerofoil section lift [-]
C_m	Aircraft pitching moment [-]
$C_{m,a.c.}$	Aerofoil section pitching moment [-]
C_{m_δ}	Aerofoil section moment sensitivity to elevator deflection [-]
C_p	Aerofoil pressure coefficient [-]
C_W	Weight coefficient [-]
Ma	Mach number [-]
Re	Reynolds number [-]

	Symbols	
α	Angle of attack	[rad]
$\hat{\alpha}$	Effective angle of incidence	[rad]
α_o	Zero-lift angle of attack	[rad]
δ	Elevator deflection angle	[rad]
Δ	Dimensionless centre of gravity offset	[—]
Δ_{cg}	Centre of gravity offset	[ft]
ϵ	Normalwash angle	[rad]
ϵ_e	Elevator effectiveness	[—]
$\eta_{a.f.}$	Normalized effective aerofoil thickness	[—]
$\eta_{a.s.}$	Normalized chordwise position of aft spar	[—]
$\eta_{c.p.}$	Spanwise station of wing centre of pressure	[—]
η_{cp}	Dimensionless spanwise position of wing centre of pressure	[—]
$\eta_{f.s.}$	Normalized chordwise position of fore spar	[—]
η	Aft wing dynamic pressure ratio	[—]
γ	Wing twist angle	[rad]
κ_b	Downwash vortex span factor	[—]
κ_ν	Downwash vortex strength factor	[—]
κ_p	Downwash position factor	[—]
κ_s	Downwash sweep factor	[—]
Λ	Sweep	[deg]
λ	Wing taper	[—]
Λ_{LE}	Leading edge sweep	[deg]
Φ	<i>Chapter 3 only.</i> Lift curve slope ratio	[—]
Φ	<i>Chapter 5 only.</i> Aerofoil boom area rate of change with distance from centroid	[—]
Ψ	<i>Chapter 3 only.</i> Fore wing area ratio	[—]
ρ	Air density	[slug/ ft ³]
ρ	<i>Chapter 5 only.</i> Material density	[lb _f / ft ³]
σ	Biplane interference factor	[—]
σ	<i>Chapter 5 only.</i> Normal stress	[lb _f / ft ²]

Nomenclature

τ	Shear stress [lb _f /ft ²]
Θ	Angle between aircraft centreline and ground plane..... [-]
Ω	Simplified model downwash factor..... [-]
ζ	Distance of aerofoil section boom to section centre of gravity [ft]

Variables	
\mathcal{R} Wing aspect ratio	[—]
A Effective area of aerofoil section boom	[ft ²]
a Speed of sound	[ft/s]
B <i>Chapter 5 only.</i> Length of equivalent beam finite element	[ft]
b Span	[ft]
\bar{c} Mean aerodynamic chord	[ft]
\hat{c} Reference chord	[ft]
c Local chord	[ft]
dA Area subtended by aerofoil skin section	[ft ²]
d_{fuse} Fuselage diameter	[ft]
D_{ind} Induced drag force	[lb _f]
E Loiter time	[s]
e Span efficiency factor	[—]
F Axial force	[lb _f]
g Acceleration due to gravity	[ft/s ²]
H <i>Chapter 3 only.</i> Normalizing factor	[—]
h Height difference between wing root quarter chord points	[ft]
I Mass moment of inertia	[slug ft ²]
I <i>Chapter 5 only.</i> Area moment of inertia	[ft ⁴]
J Polar moment of inertia	[ft ⁴]
K Induced drag constant	[—]
ℓ Moment arm	[ft]
ℓ <i>Chapter 5 only.</i> Length of aerofoil section skin	[ft]
$\ell_{1 \rightarrow 2}$ Stagger between lifting surfaces	[ft]
L Lift force	[lb _f]
l Aerofoil section lift	[lb _f]
l_{fuse} Fuselage length	[ft]
$\ell_{n.p.}$ Distance from centre of gravity to aircraft aerodynamic centre	[ft]
M Bending moment	[ft lb _f]
n_{mvr} Manoeuvre load factor	[ft]

n_{pan}	Total number of finite elements	[-]
\bar{q}	Normalized manoeuvre radius of curvature	[-]
q	Dynamic pressure	[lb _f /ft ²]
q_o	Open-section shear flow	[lb _f /ft ²]
q_i	Closed-section shear flow	[lb _f /ft ²]
R	Range.....	[nmi]
S	Area	[ft ²]
SFC_T	Thrust specific fuel consumption	[lb _m /lb _f hr]
T	Torsional moment	[ft lb _f]
t	Structural thickness	[ft]
U	Airspeed.....	[ft/s]
V	Volume	[ft ³]
V	<i>Chapter 5 only.</i> Shear force	[lb _f]
W	Weight	[lb _f]
x	Streamwise, axial, distance	[ft]
y	Spanwise station	[ft]
z	Vertical distance	[ft]
$\hat{x}, \hat{y}, \hat{z}$	<i>Chapter 5 only.</i> Element local coordinates	[ft]

Superscripts and Subscripts

1	Fore wing	[–]
2	Aft wing	[–]
α	Sensitivity to pitch angle	[/rad]
δ	Sensitivity to effector deflection angle	[/rad]
ac	Aerodynamic centre	[–]
alw	Allowable	[–]
max	Maximum allowable	[–]
$-$	Mean value	[–]
$fuel$	A property of the fuel	[–]
i, j	Indices	[–]
in	Assumed value for start of multidisciplinary analysis	[–]
$i \rightarrow j$	Effect of i on j	[–]
$m.g.$	Main landing gear contact point	[–]
$n.g.$	Nose landing gear contact point	[–]
mvr	At manoeuvring conditions	[–]
n	Sum of fore and aft wing	[–]
o	At zero lift condition	[–]
pan	Per vortex panel	[–]
req	Required for steady level flight	[–]
seg	Per wing segment	[–]
s	At the start of a mission segment	[–]
t	Centre of thrust position	[–]
y	Yield	[–]
xx, yy, zz	Moment about the x , y , or z axis	[–]

Abbreviations

Alt.	Altitude.....	[ft]
BFL	Balanced Field Length.....	[ft]
CAS	Calibrated Air Speed.....	[knots]
EAS	Equivalent Air Speed.....	[knots]
SAR	Specific Air Range.....	$[\frac{ft}{lb_f}]$
c.g.	Centre of Gravity.....	[ft]
MLD	Product of Mach number and lift-to-drag ratio.....	[-]
MTOW	Maximum Take-Off Weight.....	[lb _f]
NPL	NonPlanar Wing.....	[-]
C2OEICG	One Engine Inoperative second segment Climb Gradient....	[lb _f]
OEW	Operating Empty Weight.....	[lb _f]

1 Introduction

Transport aircraft are a mature technology which already have lower energy requirements per passenger-mile than many other transportation systems [3]. Both governments and the public, however, seek to reduce the products of combustion released into the atmosphere due to air travel. As hydrocarbon fuels will remain the dominant source of energy for aircraft for several decades [4, 5], the next generation of aircraft must reduce the amount of fuel required to complete a given mission.

Many approaches have been proposed to achieve this goal, and several of them have been investigated with respect to their potential fuel burn reduction, cost, and estimated entry to service [6]. Figure 1.1 shows seven such approaches: incremental improvements to existing aircraft configurations, termed “Intermediate-generation aircraft”; retrofits to existing aircraft; early replacement of old aircraft from the transport fleet; different airline operational strategies such as using more turboprops and reducing fuel tankering; next generation Air Traffic Management strategies, “ATM”; the use of bio-fuels rather than fossil fuel; and next-generation aircraft, including unconventional propulsion systems and aircraft configurations.

Of these approaches, next generation aircraft are “of paramount importance to outpace the anticipated growth in air transportation demand” [6]. The dotted line in Figure 1.1 shows the financial break-even point assuming a cost of 2 – 3 USD/gal for fuel. The shaded regions above this line yield a financial savings while those below the line represent an added cost for reducing emissions. These results indicate that unconventional aircraft present the possibility of not only reducing emissions but also reducing an airline’s costs.

This thesis focuses on one particular unconventional aircraft configuration, a box-wing aircraft, which consists of two main wings connected at their tips by a near vertical wing segment creating a closed wing structure. Such designs have been shown to have advantages with respect to aerodynamic [7] and structural [8] performance and are able to provide static longitudinal stability without the use of a horizontal tail [9]. In addition to box-wings, there are

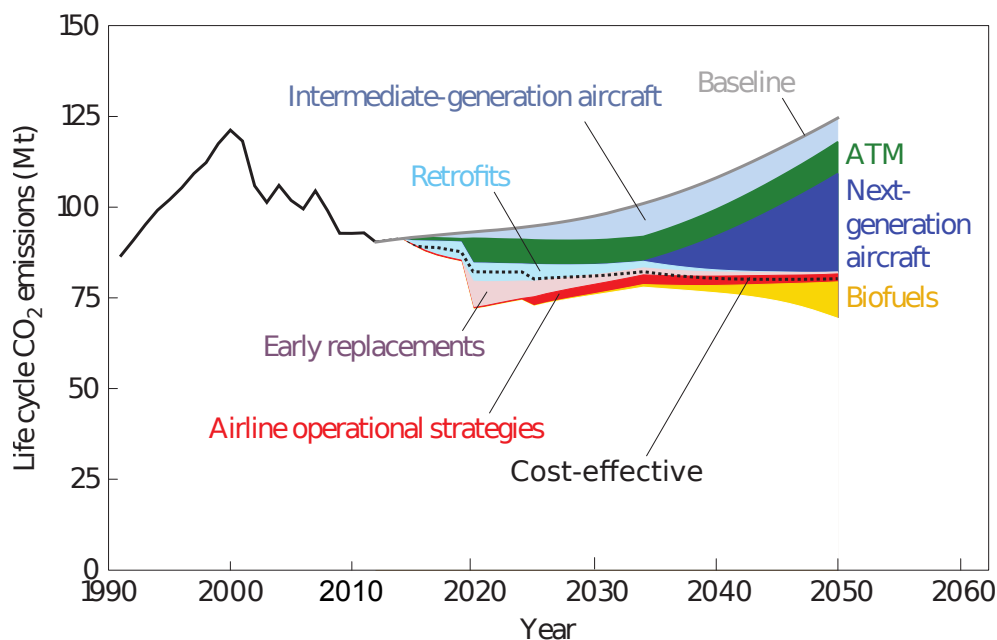


Figure 1.1: Comparison of the impact of various emission reduction strategies on the total life-cycle emissions of the transport aircraft fleet [6].

several other unconventional aircraft configurations which may enable the significant fuel burn reductions required by next-generation transport aircraft. The subsequent section will review other unconventional aircraft configurations and highlight the advantages of the box-wing design.

1.1 Next generation aircraft configurations

The impact of next-generation technologies and configurations on an aircraft's fuel consumption can be shown using equation (1.1), which determines the weight of fuel required to complete a mission of a specified range.

$$W_{fuel} = W_s \left(1 - \exp \left(\frac{-R \cdot SFC_T}{a \text{Ma}(C_L/C_D)} \right) \right) \quad (1.1)$$

For missions taking place at a constant airspeed, the fuel consumed can be reduced by: (i) reducing the weight at the start of the mission, (ii) reducing the thrust specific fuel consumption, and (iii) increasing the lift-to-drag ratio. The first of these goals can be achieved by next-generation structures and composite materials as well as potential weight savings from unconventional

wing configurations. The second approach could be realised by next generation engine designs such as geared turbofans and open rotor designs.

The third approach, increasing the lift-to-drag ratio, is the goal of most unconventional aircraft configurations. Such designs can also make use of advanced materials and propulsion concepts. Though the lift requirement of an aircraft varies depending on the weight of fuel required for the mission, increasing the lift-to-drag ratio is achieved primarily by reducing the drag generated at a fixed lift requirement. The major components of an aircraft's drag are shown in (1.2).

$$C_D = \underbrace{\overbrace{C_{D_p}}^{\text{Parasite drag}}}_{\text{Friction, Form, Interference}} + \overbrace{C_{D_i}}^{\text{Induced drag}} + \overbrace{C_{D_w}}^{\text{Wave drag}} \quad (1.2)$$

Friction Drag resulting from skin friction on wetted surfaces.

Form Drag resulting from the pressure distribution over the surface.

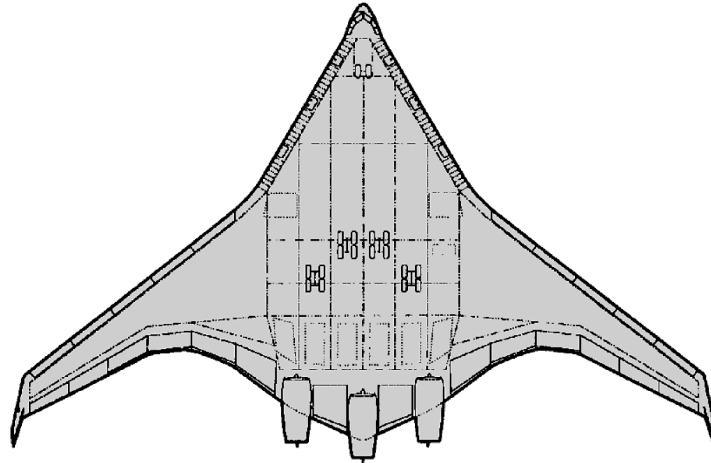
Interference Drag resulting from interactions between connected aircraft components such as wings and the fuselage.

Wave Drag resulting from shock waves occurring at transonic and supersonic speeds.

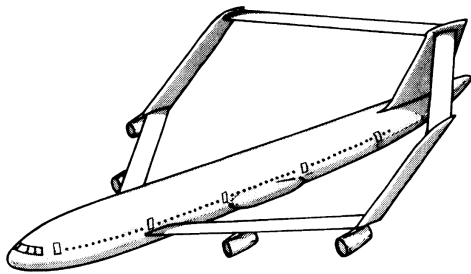
Induced drag Drag resulting from the generation of lift.

Four different unconventional aircraft designs are shown in Figure 1.2. These designs represent different approaches to drag reduction, focusing on reducing different components of the total drag. The Blended-Wing-Body design, Figure 1.2a, reduces friction and form drag by combining the wing and fuselage into one body, reducing wetted area and interference effects [10]. Box-wing designs, Figure 1.2b, reduce wave drag by allowing a smooth streamwise distribution of cross-sectional area without requiring the fuselage to taper or the addition of anti-shock bodies [9]. Such an 'area ruled' design reduces wave drag [11]. Many unconventional designs, including box-wings, increase the lift-to-drag ratio by reducing the induced drag. The induced drag coefficient is defined by (1.3), where \mathcal{R} is the aspect ratio of the main wing and e is an empirical factor termed the span-efficiency of the wing.

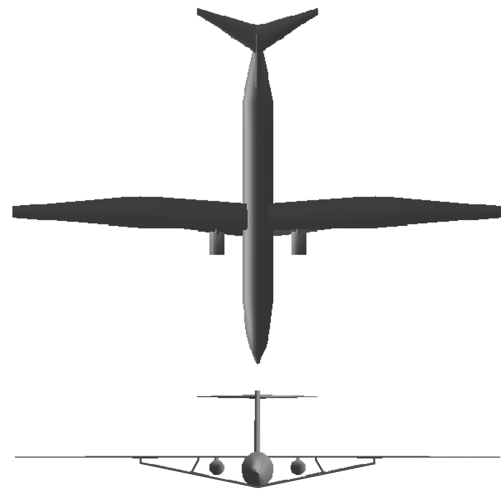
$$C_{D_i} = \frac{1}{e} \left(\frac{C_L^2}{\pi \mathcal{R}} \right) \quad (1.3)$$



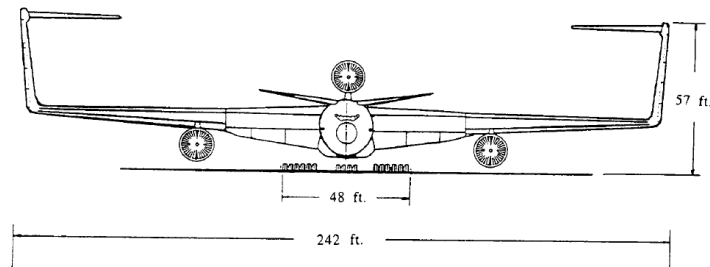
(a) Blended-Wing-Body design from Liebeck *et al.* [12]



(b) Box-wing design of Lange *et al.* [9]



(c) Truss-braced-wing of Gur *et al.* [13]



(d) 'C'-wing design of McMasters *et al.* [10]

Figure 1.2: Unconventional aircraft concepts.

For a given planform area, induced drag is inversely proportional to the wing's aspect ratio; this has led to research into aircraft concepts with very long, slender wings. However, there is a limit on the growth in aspect ratio. The weight of the structure required to resist the moments generated by such a wing will eventually eliminate any aerodynamic benefits. This has motivated investigations into braced wings which use additional structural members to reinforce the wing and allow much higher aspect ratios than conventional cantilevered wings. Gern *et al.* [14] examined various strut braced wing configurations and found that lift-to-drag ratios on the order of 23 could be achieved. Gur *et al.* [13] extended this analysis and used a truss structure rather than a simple strut to support wings with an aspect ratio of up to 14 with a lift-to-drag ratio of approximately 28; one such design is shown in Figure 1.2c. These truss braced wings, however, remain limited by the space available at airport runways and tarmacs. Airports are designed to FAA guidelines for the maximum span of aircraft [15], and a high aspect ratio aircraft may require changes to these regulations and new runways and terminals to be built, greatly reducing the number of airports such designs could service.

In the induced drag equation, (1.3), there is another independent variable which affects this drag term, the span-efficiency. Non-planar wings are a family of designs whose common element is that they are made up of two or more non-coplanar lift-generating surfaces and they achieve a higher span-efficiency than a planar wing with the same span and lift requirement [16]. Non-planar wings present an opportunity for reducing an aircraft's induced drag without violating any airport span constraints.

Of the designs shown in Figure 1.3, the 'C'-wing, Figure 1.2d, and box-wing have the lowest induced drag [16]. This reduction in induced drag not only reduces the fuel consumption during cruise but can reduce the required thrust at critical points of the mission such as takeoff and climb when the lift requirements of the aircraft are increased and induced drag is a dominant drag component. This could allow a smaller, and possibly lighter and more efficient, propulsion system to be used for such aircraft [16].

Though the 'C'-wing and box-wing have similar induced drag, the box-wing has the advantage of being a closed wing design and changing the wing structure from a cantilevered beam to a statically indeterminate structure, allowing possible reductions in weight. Closed wing designs affect many different disciplines which act together to reduce the fuel consumption of an aircraft. In order to understand the benefits of such a design, a multidisciplinary study is needed to understand the conflicting interactions between the disciplines including: aerodynamics, structures, stability, propulsion and

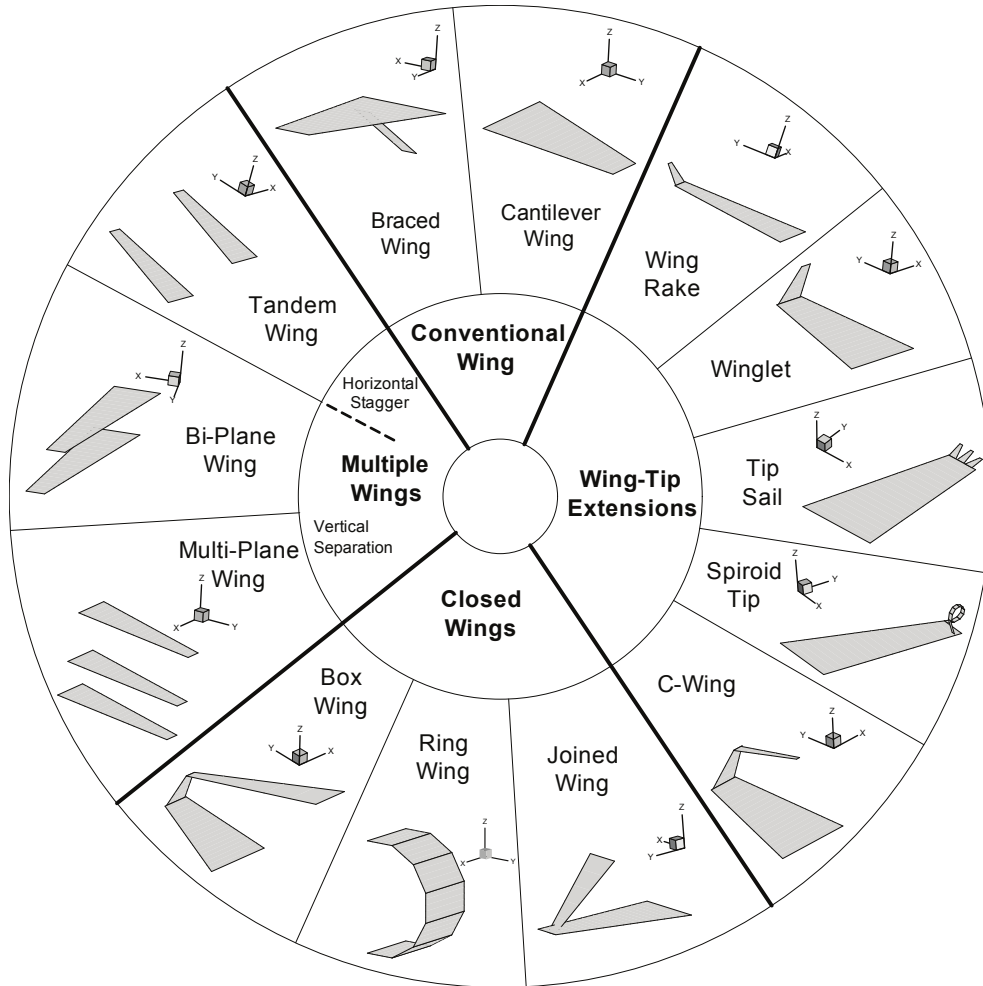


Figure 1.3: Nonplanar wing configurations [17]

mission performance.

Of the unconventional aircraft configurations shown in Figure 1.2, the box-wing has many unique characteristics, allowing an aircraft which makes use of such a wing to achieve a fuel burn advantage compared to existing aircraft designs. However, the design of such a wing is closely coupled to a wide range of disciplines, requiring a multidisciplinary study to determine the optimal box-wing configuration. This study would identify both the potential advantages of a box-wing aircraft as well as the design constraints which limit its performance. This would allow such a configuration to either be investigated further as a potential environmentally friendly transport aircraft, or be ruled out from such a role in favour of the other aircraft configurations discussed in this chapter. Though unconventional aircraft face technical, regulatory and public acceptance challenges, such designs must be considered to achieve the fuel savings required to limit the growth of air transportation emissions.

1.2 Structure of the thesis

To better understand how the disciplines of aerodynamics, stability and structures interact to enable fuel savings for box-wing aircraft, the multidisciplinary problem was investigated sequentially. The analysis first considered the constraints imposed by stability, with further disciplines added to the analysis in order to understand their impacts on the performance of a box-wing aircraft. Chapter 2 reviews previous studies on the performance of box-wings and other closed wing designs, focusing on studies which examined the aerodynamics, structures and stability and control of such configurations. Chapter 3 presents an analytic model for the static longitudinal stability of a box-wing aircraft and shows trends in the planform geometry which lead to stable, trimmable designs. These guidelines were used in a parametric study of box-wing aerodynamics in Chapter 4, where a vortex-panel model was used to predict the lift-to-drag ratio of box-wing configurations to help understand the conflicts between aerodynamic performance and static stability of the box-wing design. A new model to predict wing weight for closed wing configurations is presented in Chapter 5 and was used to investigate the structural consequences of the best wing designs identified in the parametric study. Chapter 6 discusses the problem formulation and disciplinary analyses for a multidisciplinary study of a box-wing aircraft which considers all the important disciplinary interactions discussed previously. The results of this study are discussed in Chapter 7 and compared to the results of a similar multidisciplinary analysis applied to a conventional aircraft.

2 Literature Review

The history of closed nonplanar wing designs extends back to some of the earliest investigations of optimal wing configurations, with the concept first proposed by Prandtl as early as 1918 [7]. Since then, closed nonplanar wings, both box-wings and joined-wings, have been investigated for a wide range of aircraft with varying missions [9, 18]. Such designs are of interest due to three main advantages: increased aerodynamic performance, reduced structural weight, and the ability to achieve longitudinal control and trim without the use of a horizontal tail. Previous studies of these three characteristics are discussed in Sections 2.1, 2.2 and 2.3 respectively. There are other unique advantages and challenges presented by closed-nonplanar wings which will be discussed in Section 2.4 and alternate missions for closed nonplanar wing aircraft will be discussed in Section 2.5.

2.1 Box-wing aerodynamic performance

The original closed nonplanar wing concept was the box-wing, proposed by Prandtl [7]. This design had two wings, of slight to zero dihedral, whose wing-tips were connected by a third, near vertical, wing segment. A characteristic box-wing design, as well as the main parameters which define this geometry, are shown in Figure 2.1. The height of the box-wing is defined as the vertical separation of the quarter chord points of the wings at their root and is labelled h in Figure 2.1. The stagger of the box-wing is the longitudinal, *i.e.* streamwise, separation of the wings' quarter chord point at their root and is labelled $x_{1 \rightarrow 2}$ in Figure 2.1.

Prandtl [7] described the box-wing as the configuration with the lowest induced drag for a given span and height. This result stemmed from an investigation of multiplane designs. The induced drag of multiplane configurations

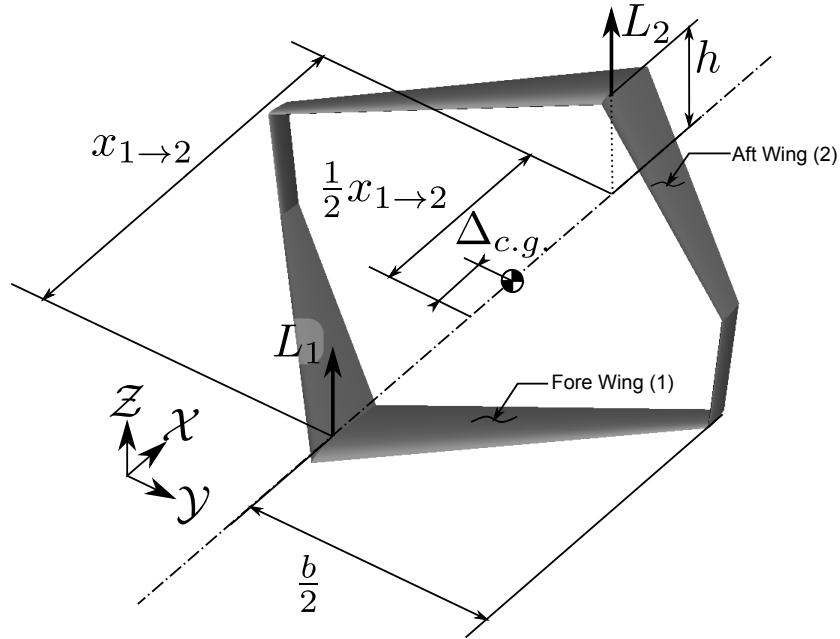


Figure 2.1: Definition of box-wing geometric parameters [1]

was given by:

$$D_{ind} = \frac{1}{\pi q} \left(\frac{L_1^2}{b_1^2} + 2\sigma \frac{L_1 L_2}{b_1 b_2} + \frac{L_2^2}{b_2^2} \right) \quad (2.1)$$

In this equation, the coefficient σ accounted for the drag due to interference between the wings. Its value was related to the wing geometry but this relationship took a different form if the multiplane were a biplane, triplane or box-wing.

It was shown that the minimum induced drag for a biplane with wings of equal spans occurred when each wing carried an equal share of the required lift. When a triplane system was investigated, however, it was found that the minimum induced drag of the triplane was both less than that of a biplane and occurred when the middle wing carried less than a one-third share of the required lift. The optimal fraction of the lift required by the middle wing was a function of the height-to-span ratio of the triplane rather than a fixed value as for the biplane. This behaviour, when extended to multiple wings, led to reduced induced drag for a lifting system made up of multiple wings when the lift carried by each wing decreased the farther it was located from the upper and lower extremities of the configuration. Such a configuration

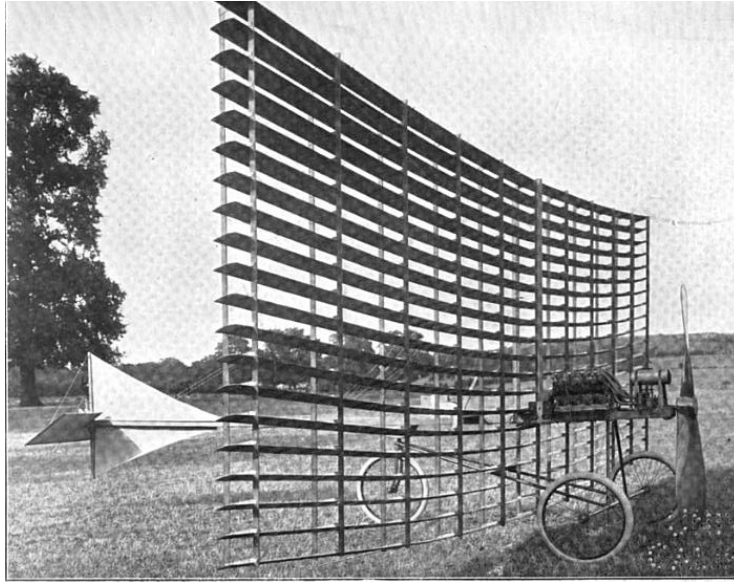


Fig. IV.

Figure 2.2: The Phillips multiplane of 1904, a precursor to the box-wing design [19].

was realised by the Phillips Multiplane [19], shown in Figure 2.2. However, Prandtl determined that the effect of an infinite series of parallel wings could be replicated by a pair of vertical wing segments joining the tips of two wings with the side-force of the vertical wings decreasing linearly until it vanished at the mid-point between the wings, as shown in Figure 2.3. The proof of why this is considered optimal is given in [20]. The induced drag of this box-wing configuration, compared to optimally loaded triplanes and biplanes, is also shown in Figure 2.4. The induced drag of the box-wing configuration was calculated as for a biplane, using a factor to account for the interference between wings (2.2). This equation was an approximation of behaviour of the analytic solution for the induced drag of optimally loaded box-wings of varying height [7]. The interference factor, σ , decreased continuously with increased vertical separation of the wings.

$$\sigma = 2 \left(\frac{1 + 0.45 \frac{h}{b}}{1.04 + 2.81 \frac{h}{b}} \right) - 1 \quad (2.2)$$

Many studies of box-wing aerodynamic performance consider that box-wings, like biplanes, require equal loading on the upper and lower wings for minimum induced drag [21, 22, 9]. However, it has been suggested that loading

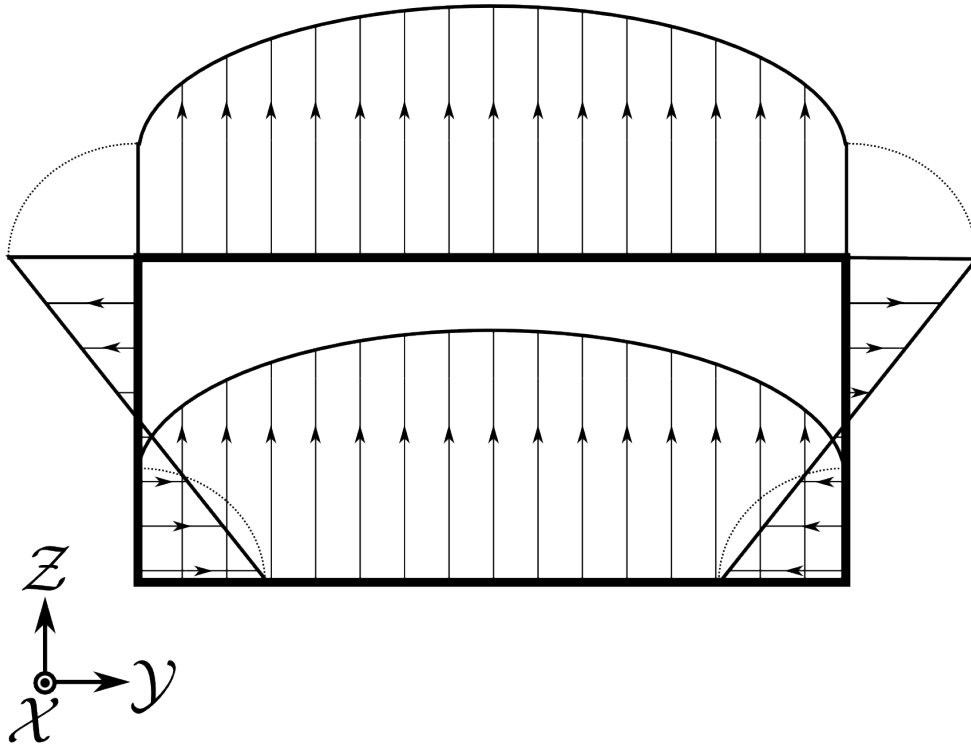


Figure 2.3: Loading for minimum induced drag of a box-wing design. Adapted from [20].

shown in Figure 2.3 is only one of a continuous range of possible loadings able to achieve the minimum induced drag. Demasi [23] proposed that the ideal box-wing loading could be modified by adding a constant circulation to the entire distribution, having the effect of increasing the lift on one wing and decreasing the lift on the other. Adding a constant circulation to the loading had no effect on the induced drag of the configuration [23, 16].

The preceding discussion of optimal lift distributions considered a box-wing with no stagger; however, Munk's stagger theorem [24] relates this design to those which have some degree of stagger. This theory states that the lifting surfaces of a multiplane may be staggered with no change to the induced drag so long as the loading on both wings does not vary with the stagger [24]. It is important to note that as the streamwise separation of the wings changes, the downwash of each wing will affect the loading of the other so both wings will have to be twisted in order to achieve the same loading.

Figure 2.5 shows a comparison of box-wings to biplanes in terms of induced

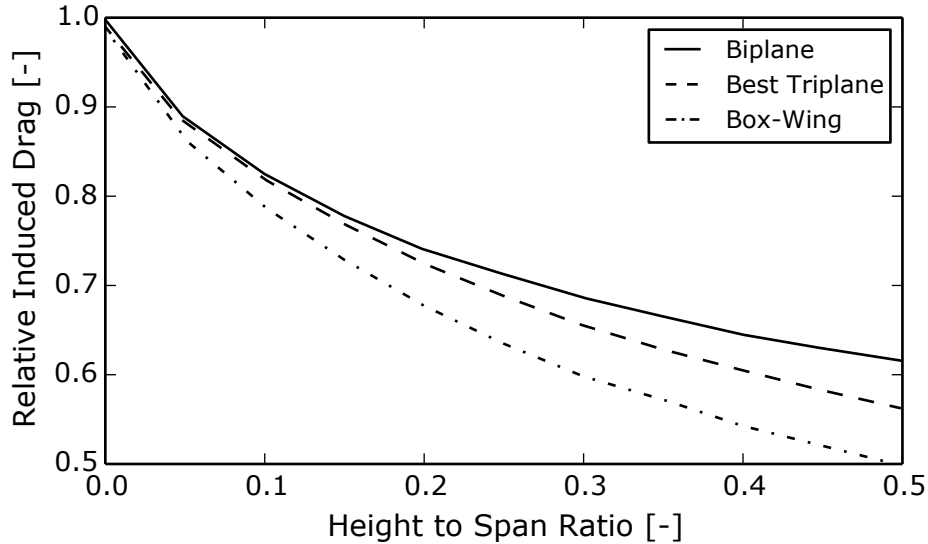


Figure 2.4: Induced drag of various multiplane configurations compared to a monoplane of the same span with the same total lift requirement. Adapted from [7].

drag. The box-wing has a slight advantage over the biplane but the drag reduction is small compared to the significant drag reduction of the box-wing and biplane compared to a monoplane of equal span [25]. The data shown in Figure 2.5 were obtained from a vortex panel model of a monoplane, biplane and box-wing. The vortex panel model used in this study showed good agreement to wind tunnel tests of the biplane and box-wing [25].

A closed non-planar wing configuration similar to the box-wing is the joined-wing. The distinction between these configurations was defined by Wolkovitch in his patent application [26]. The two main wings of a box-wing are connected by a third vertical wing surface [27] while the main wings of a joined-wing are connected either to each other or to some non-lifting body of negligible vertical extent [26]. The aerodynamic performance of a joined-wing is inferior to the box-wing though the joined-wing configuration does have some favourable structural characteristics which will be discussed in Section 2.3. In a parametric study of joined-wing configurations, Kroo *et al.* [28] showed that the best joined-wing aerodynamic performance was obtained when the wings were joined at the tip rather than at some inboard station. In a subsequent study of the span-efficiency factor of various opti-

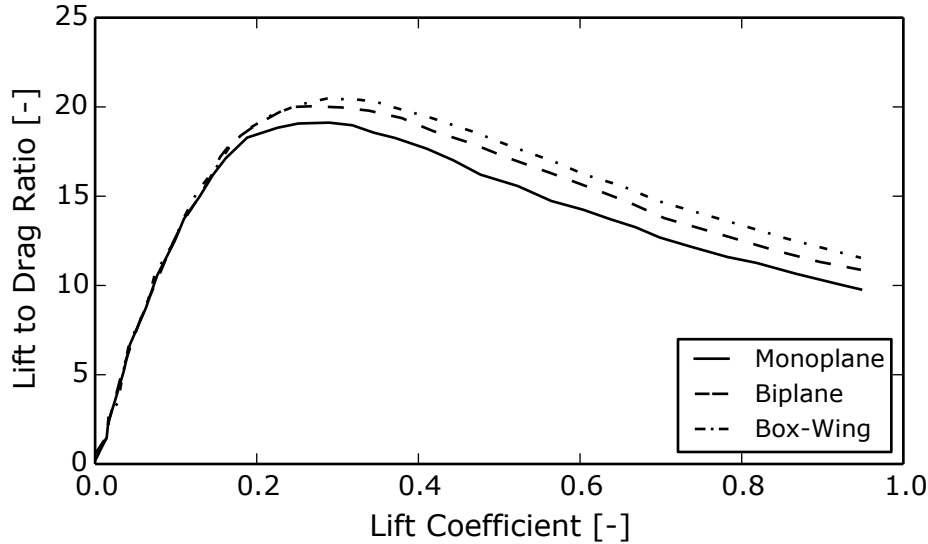


Figure 2.5: Comparison of lift-to-drag ratio for monoplanes, biplanes and box-wings over a range of target lift coefficients. Both the biplane and box-wing have a height-to-span ratio of 0.2. Adapted from [25]

mally loaded nonplanar wings of fixed span and vertical extent, it was found that the best span-efficiency of the joined-wing ($e = 1.05$) was inferior to the box-wing ($e = 1.46$) [16].

Despite the induced drag advantages of both joined- and box-wings, they were not the subject of serious investigation until the post-war period. The advent of high speed flight renewed interest in the joined-wing design as it was thought that such a configuration might reduce the pitch-up moments of swept wings at high angles of attack due to wing-tip stall [29, 30] and be more amenable to an area ruled design [11] for high transonic operations [9, 27]. Cahill and Stead [29] performed experiments on a joined-wing configuration at subsonic and transonic speeds and compared it to a monoplane with the same fore wing sweep and aspect ratio. They found that at high angles of attack, the monoplane became unstable and pitched up due to separation at the wing tips. In contrast, the joined-wing was stable and exhibited a pitch down moment under the same conditions. As the fore wing-tips stalled, the loss of lift on the fore wing led to a downward pitching moment as the aft wing experienced an effectively larger angle of attack due to the reduced downwash of the fore wing [29]. Though this investigation found that the joined-wing

designs eliminated the unstable post-stall behaviour of swept wings, the results showed only a slight advantage in induced drag and no structural advantage for the design.

A subsequent wind-tunnel investigation on a box-wing design by Henderson and Huffman [31] found stable post-stall behaviour on the highly swept wings. In addition, these authors found a slight advantage in total drag when compared to a conventional design [31]. This design was investigated further by Lockheed as a very high subsonic (Mach 0.95) civil transport. The box-wing design allowed the aircraft's cross-sectional area to follow an area-ruled profile without needing to locally change the fuselage diameter [9].

The box-wing was investigated more recently as a transport aircraft in a series of studies of a configuration referred to a 'Prandtlplane' [8, 21, 32, 33, 34, 35]. In addition to the aerodynamic advantages, the authors noted that the box-wing design allowed very large transport aircraft to operate on existing airport tarmacs. Closed wing designs enabled high lift-to-drag ratios with a projected span less than or equal to the largest monoplanes currently in service. The effects of shocks and other compressible flow phenomenon on the performance of a box-wing were assessed by Gagnon and Zingg [36] using an Euler solution. Their optimized box-wing geometry was shock free at the cruise Mach number of 0.78, indicating that such phenomenon should not preclude the box-wing designs from operating at transonic Mach numbers. The authors also noted that the minimum local Reynolds number at the wing-tips of the box-wing was much lower than the reference monoplane and may lead to a higher parasitic drag on the aerofoil unless laminar flow was maintained at the wing tips.

The aerodynamic savings of closed nonplanar wing configurations, when integrated into an aircraft design, were investigated by Rhodes and Selberg [37] in a study of a joined-wing business jet aircraft. The authors found that the most efficient two-dimensional arrangement of aerofoils were closely spaced both in stagger and height. The performance of the wings was highly dependent on the correct choice of the decalage angle, *i.e.* the difference in the installation angles of the two aerofoils. A closely staggered design, however, could not provide the moments necessary for longitudinal stability. A study of three-dimensional aerodynamics of both a closely spaced and highly staggered joined-wing showed that the aerodynamic performance of the staggered design in isolation was inferior to the closely spaced wing. However, when the performance of the entire aircraft was considered, including the drag of the empennage, it was found that the staggered joined-wing with no horizontal tail was superior [37]. These results show that in order to understand the aerodynamic advantages which closed nonplanar wings provide, the conditions

necessary for stability of the aircraft must be considered in addition to those required for reduced drag.

2.2 Box-wing stability and control

Removing the horizontal stabilizer from an aircraft can result in a significant reduction in wetted area and structural weight for the design. However, the horizontal stabilizer provides aerodynamic moments needed for both stability and control of the aircraft. Joined- and box-wing designs present the possibility of using two main lifting surfaces rather than a horizontal tail to provide these moments and this has motivated several investigations into the ability of such a design to provide both static longitudinal stability and the manoeuvrability required for a safe design.

An early attempt to make use of two main lifting surfaces for stability and control was a small general aviation biplane aircraft, the Mignet *Pou-du-ciel* [38]. This aircraft experienced a series of fatal crashes on landing, leading to several investigations into the stability and control authority of the configuration. Due to its small size, it was subject to one of the first campaigns of full scale wind-tunnel testing [39, 38]. These tests found that the aircraft required a centre of gravity position well forward of the midpoint between the fore and aft wings' aerodynamic centre in order to achieve longitudinal stability. This precluded the aircraft from operating at its most efficient point, showing a conflict between aerodynamic performance and static stability for this tailless biplane, *i.e.* dual wing, configurations.

The requirements for static stability of the box-wing configuration were investigated by Lange *et al.* [9] in their study of a high transonic transport aircraft. A parametric study of a box-wing with fore and aft wings of equal area, a static margin fixed at 5% and a constant streamwise stagger of $3\bar{c}$ is shown as a carpet plot in Figure 2.6. The ratio of fore to aft wing lift coefficient is the dependant variable; the two independent variables are the ratio of the zero-lift pitching moment to the target lift coefficient and an aerodynamic parameter, shown in Figure 2.6. The horizontal axis on the carpet plot is an arbitrary scale, lines of constant independent variable value show the trends of the dependant variable with respect to the two independent variables. As Lange *et al.* used (2.1) to predict the induced drag of the design, they sought configurations with equal lift on each wing. To reduce the effects of trim drag, they sought designs with a small, positive zero-lift pitching moment. Such a design could be achieved by varying the aerodynamic parameter. However, this parameter was not independent but rather a function of the box-wing's planform shape. The aerodynamic parameter was the product of the ratio of

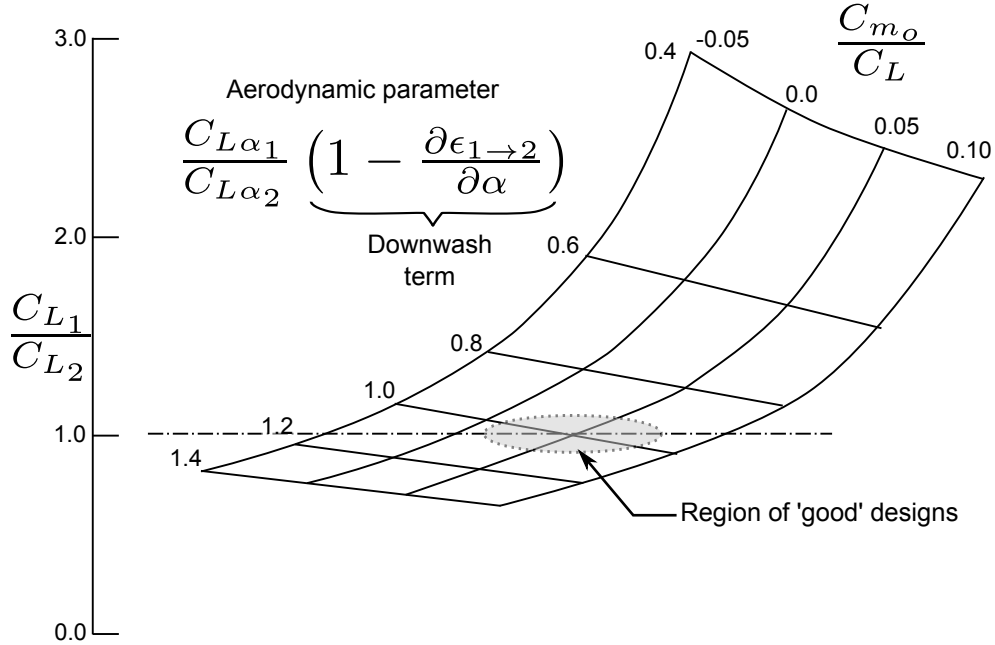


Figure 2.6: Variation of fore to aft lift ratio as a function of aerodynamic parameters of the transonic biplane. Static margin fixed at 5%. Taken from [9].

the fore to aft wing lift curve slope and a term accounting for the downwash of the fore wing on the aft. The effect of the upwash of the aft wing was not considered. For this configuration, the downwash term was less than one. In order to achieve equal loading on both wings, the sweep of the fore wing was made larger than that of the aft wing to obtain a value of the aerodynamic parameter of approximately unity, required for a good design. However this meant that the aft wing had a reduced sweep so that its contribution to the aircraft's wave drag increased. Like the *pou-du-ciel*, the requirement of static longitudinal stability incurred an aerodynamic penalty.

In a more recent study, Schiktanz and Scholz [22] also noted the conflict between stability and aerodynamic performance in box-wings. These authors used the same equation as Lange *et al.* [9], (2.1), to predict the induced drag of the wing and were unable to find a configuration which was stable and trimmed yielding optimal aerodynamic performance [22].

In the design of joined-wing aircraft, Wolkovitch [26] also sought to main-

tain equal loadings on the fore and aft wings. This was motivated not for reasons of aerodynamic performance but to ensure both wings were equally loaded and would stall near the same angle of attack. As was found for the *Pou-du-ciel*, static stability required the centre of gravity to be located forward of the midpoint of both wings' aerodynamic centres, leading to unequal wing loading when the aircraft was trimmed [40]. This forward shift of the centre of gravity was attributed to the destabilizing effect of the fore wing's downwash on the aft. Four recommendations were provided as to how this undesirable effect could be reduced: (i) decreasing the area of the fore wing, (ii) decreasing the sweep of the aft wing to increase the lift slope, (iii) increasing the vertical separation of the wings to reduce the effect of the downwash on the aft wing, (iv) allowing for some degree of static instability since the pitch damping of the joined-wing is large and the design is amenable to augmented stability systems [30].

Aircraft designs must be stable both statically and dynamically. Caja and Scholz [41] investigated the dynamic stability of a box-wing design using a combination of analytic methods and commercial software to predict stability derivatives. They found that the aircraft was dynamically stable with acceptable, stable, short-period longitudinal oscillations. They noted that, at the cruising altitude, the handling qualities related to long period longitudinal oscillations were slightly outside the most desirable range and the design would require a stability augmentation system for the highest level of handling qualities [41].

In addition to the requirement for static longitudinal stability, closed, non-planar wing designs must be controllable and have acceptable handling qualities. One unique feature of both joined- and box-wings is their direct control over lift and sideslip. That is, the vertical and horizontal forces can be controlled without inducing a change in incidence or sideslip. Since joined- and box-wings can have elevators on the fore and aft wing, both control surfaces can be deflected so as to generate lift without creating a pitching moment [30, 27]. The combination of the rudder and control surfaces on the vertical wing segment of the box-wing are also able to generate a side-force without inducing a sideslip [27]. However, the presence of multiple effectors on the wing means that there is a wide range of possible effector deflections which could produce the same change in forces and moments on the aircraft. This problem was investigated by van Ginneken *et al.* [42] who considered the best control allocation schemes for pitch and roll in a box-wing airliner [42]. These authors reported that the best strategy was to have separate effectors for pitch and roll but to have the fore and aft wings act in unison in creating pitching and rolling moments. In flight tests of a box-wing model using this control

allocation scheme, the aircraft had inherent static longitudinal stability, high pitch damping and was controllable [43].

2.3 Box-wing structural design

The structural weight of closed, nonplanar wing designs is a critical factor in determining what overall performance advantages such designs enjoy over conventional configurations. Previous studies have shown the possibility for both saving and penalties in structural weight depending on the details of the design.

Early tests of wind tunnel models found that the joined-wing design required thicker aerofoils than a cantilevered design to resist the aerodynamic loads at transonic speeds. The chord of the fore and aft wings, however, were smaller than an equivalent cantilevered wing, so the volume of material used in the joined-wing was slightly less than for a conventional design [29]. Wolkovitch noted that the joined-wing configuration creates a truss structure and loads can be divided into components which act either along or perpendicular to the plane of the truss [30] as shown in Figure 2.7. The most efficient allocation of material in the wing-box is to concentrate mass to resist the out of plane forces, as shown in Figure 2.7, which differs from the symmetric distribution of area in a conventional wing-box [26, 30]. It is unclear if Cahill and Stead [29] considered the effect of the joined-wing truss structure when designing their wind tunnel models of solid cross-section. Unlike the findings of Cahill and Stead, Wolkovitch determined that the aerofoils of a joined-wing could be thinner than for an equivalent cantilevered wing [30] and this finding has been corroborated in other studies of joined-wing aircraft configurations [44] and in wind tunnel tests [45].

In addition to the internal details of the wing-box structure, the structural advantages of joined-wings depend on the planform shape, specifically, the ratio of the span of the aft wing to the fore. Studies which varied this ratio found that the optimum ratio occurred between 0.5 [46] and 0.7 [28]. Designs with equal fore and aft spans had the highest structural weight [46, 28, 30], greater, in some cases, than for a cantilevered aircraft [30]. In Section 2.1 it was shown that the equal span design had the best aerodynamic performance, so there is a conflict between structural and aerodynamic performance in an optimal joined-wing design.

For these reasons, there have been several studies into the design of joined-wings of equal spans to determine if it is possible for such a configuration to have an advantage in structural weight compared to conventional aircraft. Samuels [44] modelled both a joined-wing and conventional design using com-

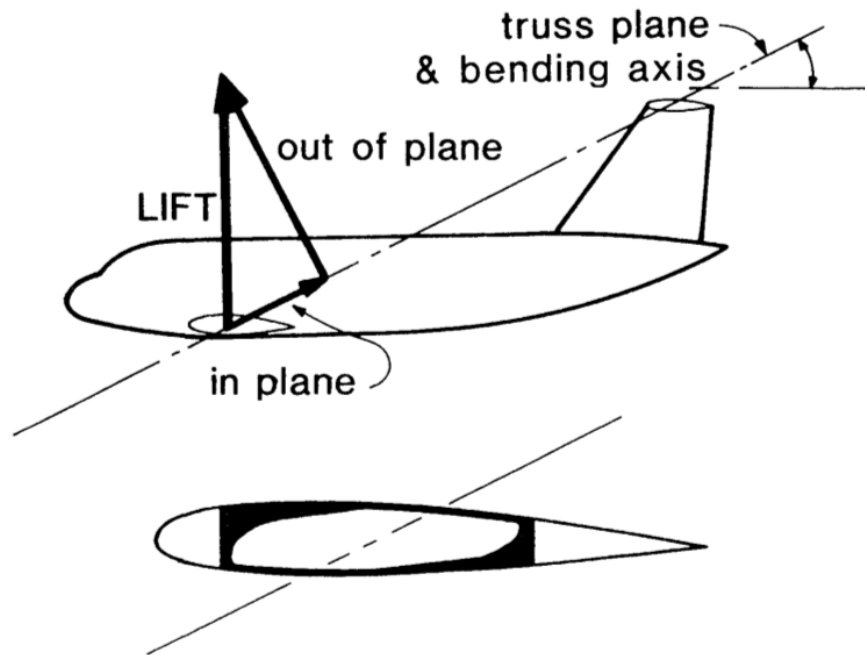


Figure 2.7: Truss plane for a joined-wing aircraft. Taken from [30]

mercial structural Finite Element Analysis (FEA) software and represented the wing-box as a series of quadrilateral elements representing the fore and aft spars and upper and lower skins [44]. The minimum weight design was found using a fully stressed approach where the thickness of each quadrilateral element was varied until it was either at the minimum gauge thickness or the stress level in the element was equal to the maximum allowable stress. This study found that when the conventional and joined-wing designs had the same minimum gauge thickness, the weight of the joined-wing was greater than that of the conventional design. However, the joined-wing enjoyed slight weight savings when the weight of the horizontal stabilizer, required by the conventional design for longitudinal stability, was considered. This was the same conclusion reached by another investigation [47] which also used a fully stressed approach to compare joined-wings and conventional designs. Samuels also claimed that the minimum gauge thickness of the joined-wing could be less than that of the conventional wing, making the joined-wing lighter than the conventional design [44]. The justification for reducing the minimum gauge

thickness was that, due to the reduction of the wing chord, a thinner skin panel could resist buckling if the number of ribs were kept the same.

As the planform shape for minimum drag and minimum structural weight differed, a series of investigations attempted to determine the optimum ratio of the aft wing to the fore wing span for minimum Direct Operating Costs (DOC) for joined-wing designs [28]. In this study, the aerodynamic forces were computed using a vortex lattice method and the internal structure of the wing was modelled using an equivalent beam model with an asymmetric cross-section similar to Figure 2.7. The authors examined the effect of varying the location of the wing joint while extending the span of the joined-wing until the joined-wing had the same structural weight as a conventional design. Designs with an aft wing 70% the span of the fore wing allowed the fore wing to have an aspect ratio much higher than the reference aircraft, leading to the total drag for the wing to be 5% less than the reference aircraft [28]. This design was then used as the starting point for a subsequent study looking into the optimum span and wing loading for a joined-wing aircraft subject to several operational constraints, shown in Figure 2.8 [48]. Though the joined-wing had a slight advantage over the conventional aircraft when only cruise conditions were considered, the joined-wing did not show any advantage once other constraints were added to the design. Most important was the constraint on buckling of the truss structure which increased the material needed by the aft wing to resist the significant axial forces resulting from the joined-wing truss structure [48]. These findings show that operation constraints for takeoff and climb performance as well as column buckling of the wing's truss structure must be considered for a true comparison between conventional and unconventional aircraft.

The interaction between nonplanar wing aerodynamics and structures was also investigated by Jansen and Perez [49], who considered the effect of different drag sources (induced, viscous, and wave drag) on the performance of a nonplanar wing. A medium range transport aircraft was considered and the wings were optimized for maximum range with a given engine and fixed volume of fuel. The box-wing was preferable when only induced and wave drag contributions were considered. The added wetted area of the box-wing penalized the design so that when viscous drag was added to the analysis, the 'C'-wing was preferred [49]. A subsequent study varied the mission requirements for the design and found that a box-wing aircraft was preferable for a regional jet mission because the structural weight of the regional jet was a greater fraction of the takeoff weight than for larger range designs. Therefore, the structural weight savings of the box-wing had a greater impact on reducing the takeoff weight and increasing the range for the regional-jet than for larger

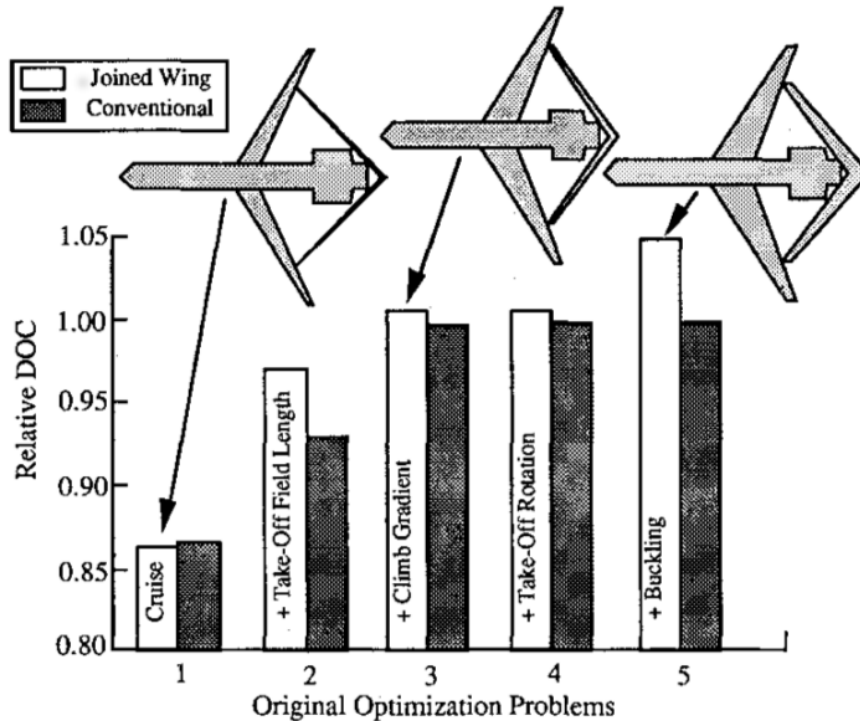


Figure 2.8: Effect of various operation constraints on the Direct Operating Cost (DOC) of both conventional and joined-wing aircraft. Taken from [48]

aircraft [17].

Other investigations of box-wing aircraft structures have focused on larger designs. Dal Canto *et al.* [8] investigated the structural details of the ‘Prandtl-plane’ design, discussed in Section 2.1. They investigated the effects of three different constraints independently: panel buckling, aileron reversal and static aeroelasticity. A subsequent study considered the effect of dynamic aeroelasticity on the design [35]. The panel buckling constraint had the largest impact on the design, increasing the structural weight by 8% [8]. The three aeroelastic constraints only increased the structural weight by 3.5%. Overall, the study found that the box-wing alone was not lighter than a conventional cantilevered design. However, as was noted with joined-wings [44, 47], when the weight of the horizontal tail was added to the weight of the conventional wing, the box-wing provided slight structural savings.

Aeroelastic concerns had a much more significant effect on the high speed box-wing airliner investigated by Lange *et al.* [9]. Before considering the flutter speed of the configuration, the study found that the box-wing was

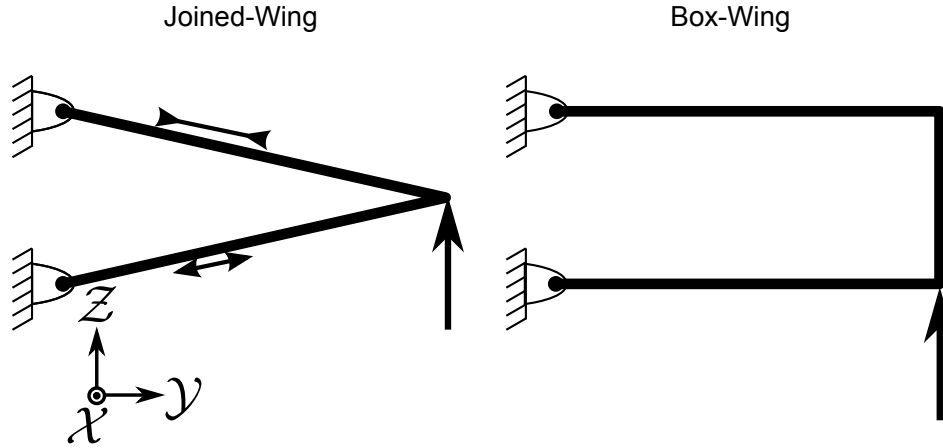


Figure 2.9: Comparison of the structure of joined-wings and box-wings.

lighter than the cantilevered wing alone. However, the aircraft's flutter speed was well below the cruising speed of 525 knots *EAS*. The authors considered alternate planform shapes to increase the flutter speed and though they were able to determine designs with significantly increased flutter speeds, they were not able to identify a configuration which met the flutter speed requirement without a prohibitive increase in structural weight. The more recent study of Divoux and Frediani made use of modern computation methods to assess the aeroelastic instabilities of a the Prandtlplane box-wing [35]. The design Mach number for this aircraft was 0.8, though flutter was found to be critical at the dive speed at sea-level conditions with a target flutter speed of 522 knots *EAS*, similar to the requirements of Lange *et al.* [9]. Divoux and Frediani found that the critical unstable mode was an in-phase 'flapping' motion of the fore and aft wings. By careful modification of the internal structure of the box-wing they were able to increase the speed at which this mode became unstable to the target flutter speed while only increasing the weight of the wing structure by 3.5%. The analysis of Lange *et al.* pre-dated that of Divoux and Frediani by almost 40 years. Modern advances in aeroelastic simulation allowed Divoux and Frediani to modify the structure so as to target only the most critical mode while maintaining a constant planform shape, significantly reducing the structural weight penalty caused by dynamic aeroelasticity on a box-wing design.

Investigations of the box-wing's internal structure have used a symmetric area distribution across the chord line rather than the area distribution shown

in Figure 2.7 [9, 8, 50]. The difference between joined-wing and box-wing internal structures can be understood by considering the joined-wing structure as a three node truss, shown in Figure 2.9. If each node of the joined-wing truss was a pinned rather than fixed connection, the structure could still resist vertical forces by converting them to axial loads in each truss element as shown in Figure 2.9. Though the most structurally efficient joined-wing designs use rigid connections [30], there is still a clear ‘strong’ axis to the joined-wing design, creating the truss plane shown in Figure 2.7. The box-wing structure is simplified to a four node statically indeterminate structure, as shown in Figure 2.9. Unlike the joined-wing, the structure could not resist any forces if it had pinned joint connections so the structure has no clear ‘strong’ axis like the joined-wing. For this reason, the distribution of material within the wing box of a box-wing is typically modelled as symmetric about the chord line.

This discussion shows that the type of connection between the three wing elements in a box-wing has a significant effect on how the loads are transferred through the statically indeterminate structure. Jemitola and Fielding looked at different joint configurations ranging from fixed connections which resisted moments about all axes to universal joints which resisted no moments. It was found that a fixed joint led to the lowest structural weight for the wing [50]. Another aspect of the box-wing design which could affect how loads are distributed through the structure was the sweep angle of the vertical wing segment. In a subsequent study, Jemitola and Fielding showed that the weight of the wing was insensitive to the sweep of the vertical segment [51]. These authors also modified empirical relations for predicting the weight of a cantilevered wing to predict the weight of a box-wing design [52]. As in previous studies, the resulting relationship for box-wings predicted structural weights slightly greater than for conventional design.

In studying joined-wings, Gallman *et al.* [48] noted that the structural weight increased significantly when the column buckling of the aft wing structure was considered. Due to the differences in the joined- and box-wing structure (see Figure 2.9) it was unclear how column buckling would affect the box-wing structure. Demasi *et al.* used both linear and non-linear buckling analysis to investigate a box-wing structure [53]. These authors found that buckling of the aft wing occurred below the design wing loading for box-wings with a short vertical segments joining the fore and aft wings, a configuration similar to a joined-wing. As the vertical separation between the wing-tips increased, the critical buckling load also increased until, past a height-to-span ratio of 0.069, the buckling of the aft wing occurred at a loading greater than the design loading. The authors also examined the effects that the sweep angle of the fore and aft wings had on the critical buckling load. The trend with

respect to sweep was less clear, with the linear analysis predicting a decrease in the critical buckling load and the non-linear analysis predicting a significant increase. The authors concluded that increased sweep was not desirable with respect to buckling as the non-linear analysis showed that, though the deflections did not diverge, the stiffness of the wing decreased significantly and this behaviour was not desirable in an aircraft structure. These findings show that column buckling of the aft wing is a concern in the design of box-wing aircraft, but that it can be mitigated by increasing the height-to-span ratio of the wing [53].

2.4 Aircraft configuration issues

Closed nonplanar wing configurations have unique effects on several other aspects of an aircraft's design. Since the fore and aft wings are not attached to the fuselage close to the centre of gravity, the landing gear for such configurations is typically mounted on the fuselage [9, 30, 21]. In addition, the vertically offset aft wing can place the vertical location of the centre of gravity higher than for a conventional aircraft. This can make it more challenging for the landing gear design to meet tip-over and tip-back constraints [30].

Another feature of joined- and box-wing designs is the reduced fuel storage capacity in the wing. Compared to a monoplane of a given projected span and planform area, a closed nonplanar will have half the volume available for fuel assuming the thickness-to-chord ratio of the aerofoils remains the same. There have been several approaches to addressing this deficiency of the design. Wolkovitch proposed increasing the distance between the fore and aft spars so that the internal structure of the wing was structurally non-optimal but allowed more fuel to be stored [30]. Rhodes and Selberg added additional internal fuel tanks to their joined-wing business jet design [37]. Other authors noted that the reduced fuel volume may still allow the aircraft to complete its primary mission but that the ferry range of a joined-wing aircraft would be reduced compared to a conventional design [54].

Gallman and Kroo showed the importance of considering takeoff performance on the design of a joined-wing aircraft [48]. Though, in their study, the joined-wing was not found to be preferable over a conventional design, closed nonplanar wings have the possibility of obtaining a performance advantage due to their takeoff performance. Kroo noted that though induced drag is not the dominant drag source at cruise, it contributes 80% of the drag during climb [16]. The reduced drag during takeoff and climb may yield benefits throughout the mission in terms of less installed thrust or reduced wing weight through smaller high lift devices. Though a joined- or box-wing design

required high lift devices on both fore and aft wings, previous studies have successfully developed high lift systems for such configurations [9, 21]

2.5 Other applications of closed nonplanar wings

Most of the previous studies considered the joined-wing aircraft for the role of transport aircraft. However, the unique planform shape and induced drag advantages of the joined-wing design have led to it being considered for a High Altitude Long Endurance (HALE) uninhabited aircraft by the US Airforce Research Laboratory [18]. The diamond planform shape of the joined-wing allows the entire wing system to house an antenna designed for low frequency operation [18]. The aircraft was required to operate at 50 – 60 thousand feet and loiter for up to 24 hours leading to a high required lift coefficient and prioritizing low induced drag. For these reasons, the joined-wing was investigated and found to be able to meet these challenging mission requirements [55].

Another application for closed nonplanar configurations is the design of aircraft with extremely short takeoff field lengths, of 3280 ft or less. This allows two runways to be installed diagonally across the area taken up by a typical runway. This could double the capacity of an airport to dispatch short range low capacity flights to better integrate it into a hub-and-spoke transport network [56].

2.6 Outstanding research questions

Previous work has investigated closed nonplanar wings, specifically box-wings, and determined the conditions necessary for such designs to achieve high aerodynamic performance, low structural weight and inherent longitudinal stability. However, these disciplines are tightly coupled and though some studies have considered the interactions between two disciplines, most studies have examined single point designs and considered neither the interactions between disciplines nor whether a design was optimal. In addition, there are many other disciplines which also affect the design and performance of box-wing aircraft including fuel volume and landing gear constraints as well as takeoff field length and climb gradient limits. The design choices necessary to meet these constraints have been shown to be different for box-wings than for conventional aircraft. The true performance advantage of such a design can only be determined by combining a multidisciplinary analysis with an optimization routine to find the best performing feasible configuration.

3 Analytic Model of Box-Wing Static Stability

Previous investigations using analytical models to predict the static stability of box-wing aircraft have determined that these configurations can achieve static stability but with an associated penalty in terms of aerodynamic performance [9, 22]. However, these studies did not investigate the sensitivity of the stability and aerodynamic performance to changes in the box-wing geometry. In addition, they did not account for the fact that both fore and aft wings induce a significant normalwash on each other. This chapter presents the development and implications of an analytic model for the longitudinal stability and aerodynamic performance of a biplane aircraft designed to provide both lift and longitudinal stability using only two main wings. This configuration is termed a dual-wing [38, 57]. Though the degree of static stability between a box-wing and dual-wing will differ, the magnitude of the difference can be estimated by considering the differences in induced drag between the designs. Both stability and induced drag are functions of the strength of the normalwash each wing induces on the other [58, 7]. The difference in the relative induced drag between a box-wing and biplane, shown in Figure 2.5, is 0.1 while the difference between a biplane and monoplane is twice as large. Therefore, the downwash of a dual-wing and box-wing could be considered similar, allowing the a mathematically simpler downwash model for conventional aircraft to be used.

The development of the analytical model is discussed in Section 3.1. This model was used in a parametric study of dual wing geometry, Section 3.2, to understand how changes in the dual wing design affect the static stability and aerodynamic performance of the configuration. The physical mechanisms leading to the behaviour observed in the parametric study were investigated in Section 3.3.

3.1 Development of the model

3.1.1 Dual-wing geometry

The geometry of the dual-wing configuration used in this study is shown in Figure 3.1. Though the two wings were not connected at the tips, as in a box-wing, the wings were swept so that the quarter chord point of the fore and aft wing-tips was at the same streamwise ($+x$) station. The sweep angles of the fore and aft wings were equal and opposite, so that the sweep angle was a function of the stagger of dual-wing design. Wolkovitch noted that changing the vertical separation of a joined-wing design can affect the stability of the design by reducing the strength of the normalwash generated by each wing on the other [30]. However, increased vertical separation reduced the induced drag of both dual- and box-wing designs [7] so that the separation should be maintained as large as possible to achieve high aerodynamic performance. For this reason, the vertical separation was not considered as a variable in this study but kept constant at a value of $h/b = 0.25$ which was representative of the separation which could be achieved in a typical aircraft design.

The aerodynamic model assumed that both untwisted wings achieved close to elliptical loading. To reflect this assumed loading, a linear taper ratio of 0.4 was chosen. All moment arms were measured from the spanwise and chordwise location of the aerodynamic centre of each wing, as shown in Figure 3.1. The stagger of the wings, however, was measured between the aerodynamic centres of their wing root.

3.1.2 Reference quantities

Since dual-wing aircraft generate significant lift on both wings, the reference quantities for normalizing force and moment coefficients differ for dual wings and conventional designs. The reference area was the sum of the fore and aft wing areas, (3.1). Previous studies which examined designs that carried significant lift on two lifting surfaces used either the sum of the two mean aerodynamic chords [40] or the streamwise distance of the two wing's aerodynamic centres [59] as the reference chord. For this study the former of these two definitions is used in (3.2), though the the choice of reference chord only affected the magnitude rather than the sensitivity of the results.

$$S_n = S_1 + S_2 \tag{3.1}$$

$$\hat{c}_n = \bar{c}_1 + \bar{c}_2 \tag{3.2}$$

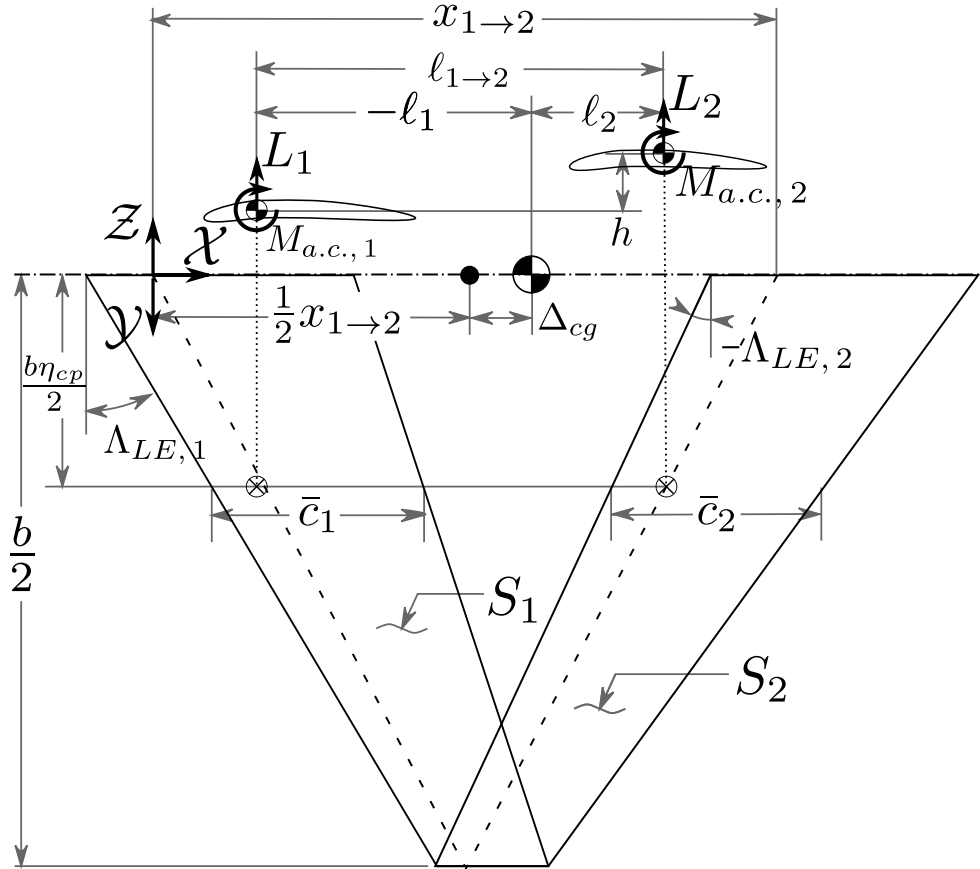


Figure 3.1: Dual-wing aircraft geometry.

Both fore and aft wings had the same projected span, which was used as the reference span. Using the reference span and area led to an uncharacteristically small aspect ratio. To allow meaningful comparisons between the dual-wing and conventional wings, any quantity which was dependent on aspect ratio was evaluated individually for each wing using the aspect ratio of that wing in isolation.

3.1.3 Steady, level flight equations

The balance of forces and moments of a dual-wing configurations are given by (3.3) and (3.4).

$$n_{mvr} C_W = n_{mvr} \left(\frac{W}{S_n q} \right) = \frac{S_1}{S_n} C_{L\alpha_1} \hat{\alpha}_1 + \eta \frac{S_2}{S_n} C_{L\alpha_2} \hat{\alpha}_2 \quad (3.3)$$

$$\begin{aligned} 0.0 = \frac{M}{S_n \hat{c}_n q} = & -\frac{\ell_1}{\hat{c}_n} \frac{S_1}{S_n} C_{L\alpha_1} \hat{\alpha}_1 - \frac{\ell_2}{\hat{c}_n} \eta \frac{S_2}{S_n} C_{L\alpha_2} \hat{\alpha}_2 \\ & + \frac{S_1 \bar{c}_1}{S_n \hat{c}_n} \left(C_{m a.c.1} + C_{m\delta_1} \delta_1 \right) \\ & + \eta \frac{S_2 \bar{c}_2}{S_n \hat{c}_n} \left(C_{m a.c.2} + C_{m\delta_2} \delta_2 \right) \end{aligned} \quad (3.4)$$

These quantities depend on the effective angle of attack, defined by (3.5).

$$\hat{\alpha}_i = \alpha + \gamma_i + \epsilon_e \delta_i - \alpha_{o,i} + \frac{2\ell_i \bar{q}}{\hat{c}_n} - \epsilon_{j \rightarrow i} \quad (3.5)$$

In (3.5), α was the aircraft angle of attack, γ_i was the wing's incidence relative to the aircraft centreline, $\epsilon_e \delta_i$ was the effective increase in incidence due to the elevator deflection, $\alpha_{o,i}$ was the effective incidence due to the aerofoil's camber and $\epsilon_{j \rightarrow i}$ was the normalwash induced by the other wing. The term \bar{q} represents the normalized pitch rate, given by:

$$\bar{q} = \frac{(n_{mvr} - 1) g \hat{c}_n}{2 (a \cdot \text{Ma})^2} \quad (3.6)$$

In (3.3) and (3.4), the lift curve slope of the wing was given by the relationship of Roskam [60] which is sensitive to both the sweep of the wing and Mach number and is given by:

$$C_{L\alpha_i} = \frac{2\pi \mathcal{R}_i}{2 + \sqrt{\left(\frac{\mathcal{R}_i \beta}{\kappa} \right)^2 \left(1 + \frac{\tan^2 \Lambda_{c/2}}{\beta^2} \right) + 4}} \quad (3.7)$$

where

$$\begin{aligned} \kappa &= \frac{C_{l\alpha_i}}{2\pi} \\ \beta &= \sqrt{1 - \text{Ma}^2} \end{aligned}$$

Several scaling factors, expressed in (3.8), were used to simplify the preceding equations. The aft wing dynamic pressure coefficient, η , represented the reduction of dynamic pressure on the aft wing due to the momentum loss in the wake of the fore wing. It was included for completeness, but for all calculations in this chapter was assumed as 1.0 [58].

$$\begin{aligned} H_{11} &= \frac{S_1}{S_n} & H_{12} &= \frac{\bar{c}_1 S_1}{\hat{c}_n S_n} \\ H_{21} &= \eta \frac{S_2}{S_n} & H_{22} &= \eta \frac{\bar{c}_2 S_2}{\hat{c}_n S_n} \end{aligned} \quad (3.8)$$

3.1.4 Effector model

The dual-wing was modelled as having independent control surfaces on the fore and aft wings. In this analysis they were used only to control pitch. The aerodynamic effects of these surfaces were modelled using the approach presented by Phillips [58, 61] and others [62], given in (3.9) and (3.10).

$$\frac{\partial C_L}{\partial \delta_i} = C_{L\alpha_i} \epsilon_{e_i} \quad (3.9)$$

$$\frac{\partial C_m}{\partial \delta_i} = \frac{\ell_i}{\hat{c}_n} C_{L\alpha_i} \epsilon_{e_i} + C_{m\delta_i} \quad (3.10)$$

3.1.5 Downwash model

This analysis used the downwash model developed by Phillips [58, 61]. This is a lifting-line model which estimates the downwash which one lifting surface induces on another. The model does not make use of any empirical corrections for lift or induced drag and it assumes steady, inviscid, incompressible flow over the wing.

$$\epsilon_{j \rightarrow i} = \frac{\partial \epsilon_{j \rightarrow i}}{\partial \alpha} \hat{\alpha}_j \quad i \neq j \quad (3.11)$$

This formulation differs slightly from that presented by Phillips [58], which included a constant plus a term proportional to incidence. In (3.11) this constant term is represented by the components of $\hat{\alpha}$ which are independent of angle of attack.

$$\frac{\partial \epsilon_{j \rightarrow i}}{\partial \alpha} = H_{j3} \frac{\kappa_\nu \kappa_p \kappa_s}{\kappa_b} \frac{C_{L\alpha_j}}{\mathcal{R}_j} \quad i \neq j \quad (3.12)$$

To account for cases when the fore and aft wing had different spans, such as the verification studies in Annex A, an additional normalizing factor was

introduced, (3.13). When a smaller wing induced a normalwash on a larger wing, only the fraction of the larger wing in the smaller wing's wake experienced the normalwash. When a smaller wing experienced a normalwash from a larger wing, the entire wing was affected. Equation (3.13) is an approximation of this behaviour.

$$H_{j3} = \begin{cases} \frac{b_j}{b_i} & b_j < b_i \\ 1.0 & b_j > b_i \end{cases} \quad (3.13)$$

In (3.12), the parameters κ_b and κ_ν were constants for an elliptical wing. The value κ_p was governed by (3.14), given as equation 4.5.6 in [58]. The sweep coefficient was calculated based on equation 4.5.12 given in [58].

$$\kappa_p \left(\frac{2x}{b}, \frac{2y}{b}, \kappa_b \right) = \frac{2\kappa_b^2}{\pi^2 \left(\left(\frac{2y}{b} \right)^2 + \kappa_b^2 \right)} \left(1 + \frac{\left(\frac{2x}{b} \right) \left(\left(\frac{2x}{b} \right)^2 + 2 \left(\frac{2y}{b} \right)^2 + \kappa_b^2 \right)}{\left(\left(\frac{2x}{b} \right)^2 + \left(\frac{2y}{b} \right)^2 \right) \sqrt{\left(\frac{2x}{b} \right)^2 + \left(\frac{2y}{b} \right)^2 + \kappa_b^2}} \right) \quad (3.14)$$

3.1.6 Static longitudinal stability

The static stability of the dual-wing configuration was a function of the sensitivity of lift and moment to the angle of attack, α . Taking the derivative of (3.3) and (3.4) led to an infinite series as the downwash strength of wing i was dependent on the lift of wing j which was itself dependent on the downwash strength of wing i .

$$C_{L_\alpha} = H_{11} C_{L_{\alpha_1}} \left(1 - \frac{\partial \epsilon_{2 \rightarrow 1}}{\partial \alpha} \left(1 - \frac{\partial \epsilon_{1 \rightarrow 2}}{\partial \alpha} \left(1 - \frac{\partial \epsilon_{2 \rightarrow 1}}{\partial \alpha} \left(1 - \frac{\partial \epsilon_{2 \rightarrow 1}}{\partial \alpha} (\dots) \right) \right) \right) \right) + H_{12} C_{L_{\alpha_2}} \left(1 - \frac{\partial \epsilon_{2 \rightarrow 1}}{\partial \alpha} \left(1 - \frac{\partial \epsilon_{1 \rightarrow 2}}{\partial \alpha} \left(1 - \frac{\partial \epsilon_{2 \rightarrow 1}}{\partial \alpha} \left(1 - \frac{\partial \epsilon_{2 \rightarrow 1}}{\partial \alpha} (\dots) \right) \right) \right) \right) \quad (3.15)$$

$$\begin{aligned}
 C_{m_\alpha} = & \\
 & \frac{\ell_1}{\hat{c}_n} H_{11} C_{L_{\alpha_1}} \left(1 - \frac{\partial \epsilon_{2 \rightarrow 1}}{\partial \alpha} \left(1 - \frac{\partial \epsilon_{1 \rightarrow 2}}{\partial \alpha} \left(1 - \frac{\partial \epsilon_{2 \rightarrow 1}}{\partial \alpha} \left(1 - \frac{\partial \epsilon_{2 \rightarrow 1}}{\partial \alpha} (\dots) \right) \right) \right) \right) \\
 & + \frac{\ell_2}{\hat{c}_n} H_{12} C_{L_{\alpha_2}} \left(1 - \frac{\partial \epsilon_{2 \rightarrow 1}}{\partial \alpha} \left(1 - \frac{\partial \epsilon_{1 \rightarrow 2}}{\partial \alpha} \left(1 - \frac{\partial \epsilon_{2 \rightarrow 1}}{\partial \alpha} \left(1 - \frac{\partial \epsilon_{2 \rightarrow 1}}{\partial \alpha} (\dots) \right) \right) \right) \right)
 \end{aligned} \tag{3.16}$$

To make this problem tractable, this series was truncated after the first term. This approach yielded equations for the sensitivity of lift (3.7) and pitching moment (3.18) to the angle of incidence.

$$\begin{aligned}
 C_{L_\alpha} \simeq & H_{11} C_{L_{\alpha_1}} \left(1 - \frac{\partial \epsilon_{2 \rightarrow 1}}{\partial \alpha} \left(1 - \frac{\partial \epsilon_{1 \rightarrow 2}}{\partial \alpha} \right) \right) \\
 & + H_{12} C_{L_{\alpha_2}} \left(1 - \frac{\partial \epsilon_{1 \rightarrow 2}}{\partial \alpha} \left(1 - \frac{\partial \epsilon_{2 \rightarrow 1}}{\partial \alpha} \right) \right)
 \end{aligned} \tag{3.17}$$

$$\begin{aligned}
 C_{m_\alpha} \simeq & \frac{\ell_1}{\hat{c}_n} H_{11} C_{L_{\alpha_1}} \left(1 - \frac{\partial \epsilon_{2 \rightarrow 1}}{\partial \alpha} \left(1 - \frac{\partial \epsilon_{1 \rightarrow 2}}{\partial \alpha} \right) \right) \\
 & + \frac{\ell_2}{\hat{c}_n} H_{12} C_{L_{\alpha_2}} \left(1 - \frac{\partial \epsilon_{2 \rightarrow 1}}{\partial \alpha} \left(1 - \frac{\partial \epsilon_{1 \rightarrow 2}}{\partial \alpha} \right) \right)
 \end{aligned} \tag{3.18}$$

The static longitudinal stability of an aircraft design is often quantified by the static margin. It is defined by:

$$\text{static margin} \equiv \frac{\ell_{n.p.}}{\hat{c}_n} = -\frac{C_{m_\alpha}}{C_{L_\alpha}} \tag{3.19}$$

3.1.7 Trimmed performance

The trimmed performance of the dual-wing can be determined by combining the two equations of motion, (3.3) and (3.4) along with a separate equation for the effective angle of attack (3.5) and downwash (3.11) on each wing. This yielded a system of six equations with nine unknowns, expressed in matrix as:

$$\mathbf{A} \begin{bmatrix} \alpha \\ \gamma_1 \\ \gamma_2 \\ \delta_1 \\ \delta_2 \\ \hat{\alpha}_1 \\ \hat{\alpha}_2 \\ \epsilon_{2 \rightarrow 1} \\ \epsilon_{1 \rightarrow 2} \end{bmatrix} = \underbrace{\begin{bmatrix} C_W \\ -H_{12}C_{m,a.c.1} - H_{22}C_{m,a.c.2} \\ \alpha_{o,1} - \frac{2\ell_1\bar{q}}{\hat{c}_n} \\ \alpha_{o,2} - \frac{2\ell_2\bar{q}}{\hat{c}_n} \\ 0.0 \\ 0.0 \end{bmatrix}}_{\mathbf{B}} \quad (3.20)$$

where:

$$\mathbf{A} = \begin{bmatrix} 0 & 0 & 0 & 0 & 0 & H_{11}C_{L\alpha_1} & H_{21}C_{L\alpha_2} & 0 & 0 \\ 0 & 0 & 0 & H_{12}C_{m\delta_1} & H_{22}C_{m\delta_2} & -\frac{\ell_1}{\hat{c}_n}H_{11}C_{L\alpha_1} & -\frac{\ell_2}{\hat{c}_n}H_{21}C_{L\alpha_2} & 0 & 0 \\ 1 & 1 & 0 & \epsilon_{e,1} & 0 & -1 & 0 & -1 & 0 \\ 1 & 0 & 1 & 0 & \epsilon_{e,2} & 0 & -1 & 0 & -1 \\ 0 & 0 & 0 & 0 & 0 & 0 & \frac{\partial \epsilon_{2 \rightarrow 1}}{\partial \alpha} & -1 & 0 \\ 0 & 0 & 0 & 0 & 0 & \frac{\partial \epsilon_{1 \rightarrow 2}}{\partial \alpha} & 0 & 0 & -1 \end{bmatrix} \quad (3.21)$$

In (3.20), the \mathbf{B} matrix was structured to solve for a balance of forces and moments. The matrix formulation allowed the lift and moment of each wing to be determined. The drag was determined using:

$$C_D = H_{11} C_{D_1} + H_{21} C_{D_2} + C_{D_{int}} \quad (3.22)$$

The induced drag caused by the dual-wing's mutual interference was calculated using (2.1) and (2.2). The drag for the individual wings is calculated using (3.23).

$$C_{D_i} = C_{D_{p_i}} + C_{D_{w_i}} + C_{D_{i_i}} \quad (3.23)$$

where:

$$C_{D_{p_i}} = C_{d_{p0}} + C_{d_{p1}}C_{L_i} + C_{d_{p2}}C_{L_i}^2 \quad (3.24)$$

$$C_{D_{i_i}} = \frac{1}{\pi \mathcal{R}_i} C_{L_i}^2 \quad (3.25)$$

The wave drag, $C_{D_{w_i}}$, for each wing was modelled using the Korn equation in the manner presented in [13]. The wave drag predicted by the Korn equation was dependent on an empirical technology factor. A value of 0.85 was used in this study as it was representative of conventional aerofoil section performance [13].

3.1.8 Determining wing installation angles

The system of equations given by (3.20) were under-defined with only six equations available to solve for nine unknowns. To solve these equations, it was assumed that the aircraft was designed for an operating condition where the aircraft would be trimmed at zero angle of attack with no control inputs. The wing installation angles were determined by solving (3.20) with all effector deflections and the angle of attack set to zero, as shown in (3.26).

$$\begin{bmatrix} \gamma_1 \\ \gamma_2 \\ \hat{\alpha}_1 \\ \hat{\alpha}_2 \\ \epsilon_{2 \rightarrow 1} \\ \epsilon_{1 \rightarrow 2} \end{bmatrix} = \mathbf{A} \begin{bmatrix} 0 & 0 & 0 & 0 & 0 & 0 \\ 1 & 0 & 0 & 0 & 0 & 0 \\ 0 & 1 & 0 & 0 & 0 & 0 \\ 0 & 0 & 0 & 0 & 0 & 0 \\ 0 & 0 & 0 & 0 & 0 & 0 \\ 0 & 0 & 1 & 0 & 0 & 0 \\ 0 & 0 & 0 & 1 & 0 & 0 \\ 0 & 0 & 0 & 0 & 1 & 0 \\ 0 & 0 & 0 & 0 & 0 & 1 \end{bmatrix}^{-1} \mathbf{B} \quad (3.26)$$

3.1.9 Off-design performance

After determining the wing installation angles, a different formulation was needed to predict the performance of the aircraft at any other operating point. There were infinite combinations for angle of attack and elevator deflections to maintain steady, trimmed flight. An analytical solution could be obtained by assuming either that the angle of attack was constant or that only the fore or aft elevator was used to trim the aircraft. A method to determine the combination of multiple control surface deflections and angle of attack which led to minimum trim drag was developed by Goodrich *et al.* [63]. This approach could also be applied to the dual-wing control problem. However, the focus of the present analysis is on the stability of the design rather than the trim drag so the problem has been simplified by assuming that longitudinal trim is achieved without the use of the fore wing effector.

Using (3.27) the angle of attack and aft effector deflection necessary for trimmed steady flight could be determined for a given set of wing installation

angles.

$$\begin{bmatrix} \alpha \\ \delta_2 \\ \hat{\alpha}_1 \\ \hat{\alpha}_2 \\ \epsilon_{2 \rightarrow 1} \\ \epsilon_{1 \rightarrow 2} \end{bmatrix} = \mathbf{A} \begin{bmatrix} 1 & 0 & 0 & 0 & 0 & 0 \\ 0 & 0 & 0 & 0 & 0 & 0 \\ 0 & 0 & 0 & 0 & 0 & 0 \\ 0 & 0 & 0 & 0 & 0 & 0 \\ 0 & 1 & 0 & 0 & 0 & 0 \\ 0 & 0 & 1 & 0 & 0 & 0 \\ 0 & 0 & 0 & 1 & 0 & 0 \\ 0 & 0 & 0 & 0 & 1 & 0 \\ 0 & 0 & 0 & 0 & 0 & 1 \end{bmatrix}^{-1} \begin{bmatrix} \mathbf{B} - \mathbf{A} \\ 0.0 \\ \gamma_1 \\ \gamma_2 \\ 0.0 \\ 0.0 \\ 0.0 \\ 0.0 \\ 0.0 \\ 0.0 \end{bmatrix} \quad (3.27)$$

3.1.10 Verification

In order to determine if the present aerodynamic model was able to capture the same behaviour as the model of Phillips [58], a verification study was performed. This study, shown in Annex A, compared the results from a conventional and canard aircraft using both the present model and results published by Phillips [58]. The present model showed good agreement with Phillips [58] for a conventional aircraft. In the case of the canard aircraft, the model captured important effects of the canard's downwash on the main wing, which Phillips did not model.

3.2 Parametric study

The sensitivity of the longitudinal stability and aerodynamic performance of a dual wing to changes in the planform geometry was investigated using a parametric study. There were three parameters of interest: the fraction of the total planform area used by the fore wing, the streamwise stagger of the fore and aft wings at their root, and the displacement of the centre of gravity from the midpoint between the two wings' aerodynamic centres. These parameters are shown in Figure 3.1.

Previous work has shown that a regional-jet aircraft is well suited to the box-wing design [17]. The dual-wing designs considered in this study used the same dimensions and weights as the Bombardier CRJ-200 aircraft [64], as shown in Table 3.1. Rather than maintain the same span as the reference aircraft, the projected span of the dual wing was chosen so that the aspect ratio of both wings was equal to that of the reference aircraft when fore and aft wings were of equal area. The manoeuvre altitude was determined as the altitude

at which the aircraft would have zero specific excess power when performing a maximum design manoeuvre of $2.5g$, typical of transport aircraft [65].

Table 3.1: Reference aircraft characteristics

Total wing area	587.1	ft ²
Aspect ratio	8.9	–
Maximum takeoff weight	47000	lb _f
Fuselage length	80.0	ft
Cruise Mach	0.74	–
Cruise altitude	37000	ft
Manoeuvre altitude	25000	ft

Both wings were assumed to have cambered aerofoil profiles with a constant thickness-to-chord ratio along the span. A NACA 23012 aerofoil was assumed and the section properties of this aerofoil were estimated at a fully turbulent Reynolds number of 1×10^7 and Mach 0.74 using the VGK aerofoil analysis tool [66]. These section properties are given in Table 3.2. The control surface on the aft wing was assumed to cover 25% of the chord and extend along the inner 25% of the aft wing span. The aerodynamic attributes of this elevator were calculated based on data for plain flaps and elevators given in [62]. These values are shown in Table 3.3. The pressure distribution over the NACA 23012 aerofoil, generated by VGK, is shown in Figure 3.2.

Table 3.2: Reference aerofoil section properties

Zero-lift incidence	–2.015	deg
Zero incidence lift	0.221	–
Section pitching moment coefficient	–0.0096	–
Constant parasitic drag coefficient	0.0081	–
Linear parasitic drag coefficient	0.0010	–
Quadratic parasitic drag coefficient	0.0059	–
Maximum section lift coefficient	1.2	–

Table 3.3: Aft wing elevator attributes

Elevator effectiveness	0.182	/rad
Elevator section moment coefficient	-0.2145	/rad

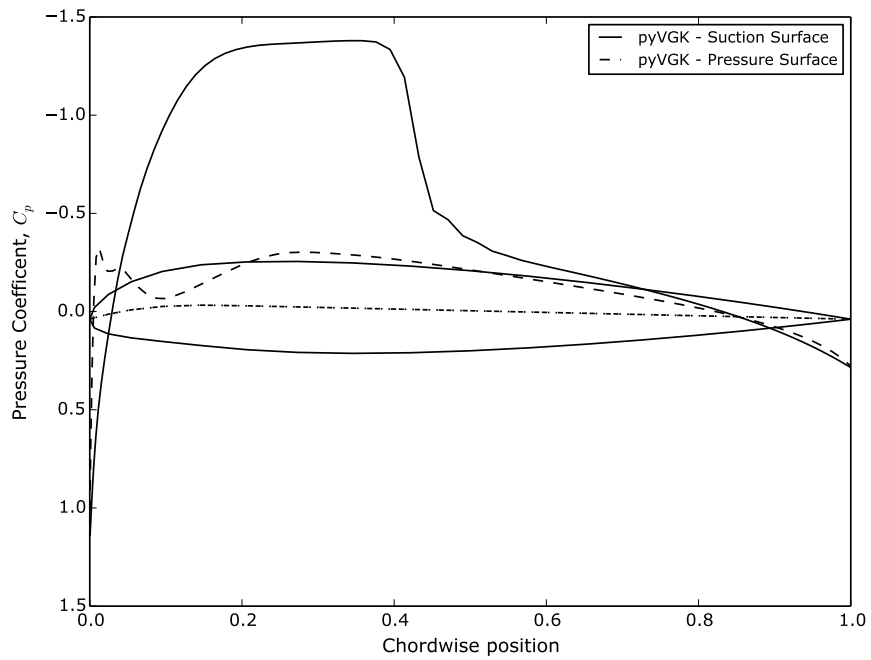


Figure 3.2: Pressure distribution on a NACA23012 aerofoil. $Ma = 0.74$, $Re = 1 \times 10^7$, $C_l = 0.4$.

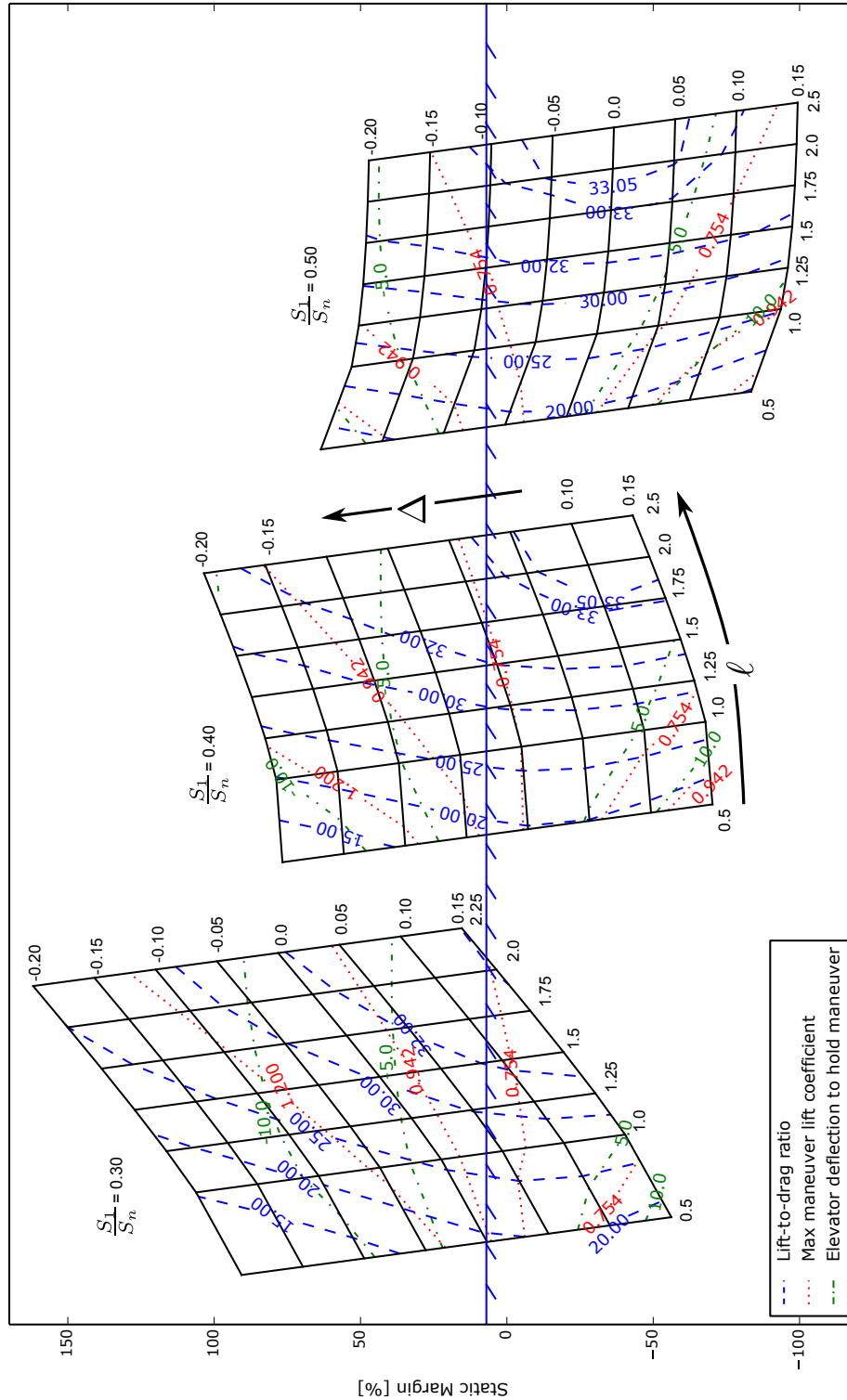


Figure 3.3: Carpet plot of the parametric study results at cruise conditions. The fore wing area ratio is shown as $\frac{S_1}{S_n}$. The dimensionless stagger is shown as $l = \frac{2x_{1 \rightarrow 2}}{b}$. The dimensionless c.g. offset is shown as $\Delta = \frac{2\Delta_{c.g.}}{b}$. The minimum acceptable static margin of 7.0% is shown as a hatched line.

The results of the parametric study are shown in Figure 3.3. The lower limit for the static margin was 7%, shown as a hatched line. Designs with a static margin less than zero were longitudinally unstable. The design with the centre of gravity located midway between two wings of equal areas was unstable for all wing separations investigated; the magnitude of the instability increased with increasing separation between the two wings. The equal area design could only be made stable by a forward shift in the centre of gravity, leading to an increased lift force required by the fore wing. By reducing the area of the fore wing, the aircraft could be made stable with a smaller forward displacement of the centre of gravity, as has been noted in previous studies [30, 40].

Movement of the centre of gravity or reducing the fore wing area impacted the ability of the dual-wing to perform a $2.5g$ manoeuvre. The requirement for the aircraft to remain in trim meant that a forward shift in the centre of gravity led to the fore wing generating a larger lift force. The maximum section lift coefficient for the wing's aerofoil profile was 1.2. Assuming the wing was elliptically loaded and had a linear taper of 0.4, the outer segments of the wing would exceed the aerofoil section's maximum lift coefficient when the wing's lift coefficient was greater than 0.754. If the taper were increased to unity, the wing would stall locally at the wing-root at a lift coefficient of 0.942. There was a small design space of where the aircraft could be made stable and avoid stall during the $2.5g$ manoeuvre. This feasible design space decreased as the fore wing area was reduced to the point that almost all designs with a fore wing area ratio of 0.3 would experience local stalling unless the fore wing's taper were increased. The aft wing elevator deflections required to maintain (but not initiate) the $2.5g$ manoeuvre are also shown in Figure 3.3. For all feasible designs, the required deflection was less than 5 deg which would leave sufficient deflection to initiate the manoeuvre. Manoeuvre control authority did not constrain the dual-wing design.

Contours of lift-to-drag ratio were used as a metric of aerodynamic performance for the dual-wing. The previous observations have been applicable to both dual-wings and box-wings. However, as the asymmetric lift distribution between the fore and aft wings has been shown to have a much more significant effect on biplanes [7] than on box-wings [23], observations related to aerodynamic performance apply only to dual-wings. The highest lift-to-drag ratio achieved in the parametric study occurred for the configuration with equal area wings and without a centre of gravity offset. This configuration, however, was longitudinally unstable. The changes to the design required to achieve static stability, a forward shift of the centre of gravity or reduction of the fore wing area, increased the drag of the aircraft as they led to a higher fore

wing loading. This aspect of dual wing performance was also observed in the wind tunnel tests of the *pou-du-ciel* [39, 38]. Though no stable design could achieve the maximum possible aerodynamic performance, a slight reduction of the fore wing area ratio to 0.4 allowed an acceptable degree of stability to be achieved with a much smaller forward shift of the centre of gravity, leading to the best aerodynamic performance in the feasible design region. Aerodynamic performance also tended to increase with increased wing separation. The separation of the wings reduced the influence of each wing's normalwash on the other and allowed the moments necessary to trim the aircraft to be generated with a smaller change in the loading between the two wings. However, there was a physical limit on the allowable separation of $2.21\frac{b}{2}$ which corresponded to the length of the reference aircraft fuselage.

The results of the parametric study showed several important trends of how changes to the planform shape of a dual-wing affected stability and manoeuvrability. Decreasing the fore wing area of the dual-wing allowed the aircraft to achieve static stability with a smaller shift in the centre of gravity but with an increase in the fore wing loading, leading to a reduced design space where the aircraft could perform a $2.5g$ manoeuvre. Aerodynamic performance was also degraded by a reduction of the fore wing area. However a slight reduction of the fore wing area allowed the best aerodynamic performance for a stable design. Increasing the stagger of the wings increased aerodynamic performance but led to a decrease in longitudinal stability. The reason for this counter-intuitive behaviour will be examined in the following section.

3.3 Longitudinal stability

3.3.1 Simplified stability model

The parametric study presented in Section 3.2 noted two unusual trends in the performance of dual wings: the best aerodynamic performance could not be achieved by a stable design, and the degree of instability in the design increased with increasing separation. These behaviours are not observed in conventional aircraft where separation of the main wing and horizontal tail increases the stability of the design. To better understand the reasons for these trends, the equations for the lift and moment sensitivities of the dual wing, (3.17) and (3.18), were simplified by making several assumptions. The first assumption was that the normalwash of each wing was independent of the normalwash of the other. The normalwash of both surfaces was still considered but its strength was not dependent on the other surface. The second assumption was

that the two wings were unswept so that κ_s was neglected. The wings were also assumed to have no vertical separation. Finally, the following quantities were introduced to simplify the expression. The fore wing area ratio was redefined as, Ψ . The distance between the centre of gravity and the fore wing, x_1 , and aft wing, x_2 , were each functions of the separation between the two wings' aerodynamic centres, $x_{1 \rightarrow 2}$, and the centre of gravity offset, $\Delta_{c.g}$. These two quantities were made dimensionless by ℓ and Δ , respectively.

$$\Psi = \frac{S_1}{S_n} = H_{11} \quad (3.28)$$

$$x_1 = -\left(\frac{1}{2}x_{1 \rightarrow 2} + \Delta_{c.g}\right) \quad (3.29)$$

$$x_2 = \left(\frac{1}{2}x_{1 \rightarrow 2} - \Delta_{c.g}\right) \quad (3.30)$$

$$\ell = \frac{2x_{1 \rightarrow 2}}{b} \quad (3.31)$$

$$\Delta = \frac{2\Delta_{c.g}}{b} \quad (3.32)$$

As the area ratio of the wings changed, their respective aspect ratios differed; (3.33) shows the effect this had on the lift curve slope, Φ_i , of each wing. This equation is based on the lift curve slope of a subsonic, unswept elliptical wing as found in [58] rather than on (3.7).

$$\Phi_i = \frac{C_{L,\alpha_i}}{2\pi} = \frac{b^2}{b^2 + 2\frac{S_i}{S_n}S_n} \quad (3.33)$$

Making these substitutions yields (3.34):

$$\begin{aligned} \frac{\ell_{np}}{\hat{c}_n}(\ell, \Delta, \Psi) &= \frac{\frac{x_1}{\hat{c}_n}\Psi C_{L\alpha_1} \left(1 - \frac{\partial \epsilon_1}{\partial \alpha}\right) + \frac{x_2}{\hat{c}_n}(1 - \Psi)C_{L\alpha_2} \left(1 - \frac{\partial \epsilon_2}{\partial \alpha}\right)}{\Psi C_{L\alpha_1} \left(1 - \frac{\partial \epsilon_1}{\partial \alpha}\right) + (1 - \Psi)C_{L\alpha_2} \left(1 - \frac{\partial \epsilon_2}{\partial \alpha}\right)} \\ &= \frac{b\ell}{4\hat{c}_n} \left(\frac{(1 - \Psi)\Phi_2\Omega_2(\ell, 0, \Psi) - \Psi\Phi_1\Omega_1(-\ell, 0, 1 - \Psi)}{(1 - \Psi)\Phi_2\Omega_2(\ell, 0, \Psi) + \Psi\Phi_1\Omega_1(-\ell, 0, 1 - \Psi)} \right) + \frac{b\Delta}{2\hat{c}_n} \end{aligned} \quad (3.34)$$

where the downwash function at each wing, Ω_i is:

$$\begin{aligned} \Omega_i(\ell, y, \Psi) &= \left(1 - \frac{C_{L\alpha_j}}{A_j} \frac{\kappa_\nu}{\kappa_b} k_p \left(\frac{1}{2}b\ell, y, \kappa_b \right) \right) \\ &= \left(1 - 2\pi\Phi_j \left(\frac{\Psi S_n}{b^2} \right) \frac{\kappa_\nu}{\kappa_b} k_p \left(\frac{1}{2}b\ell, y, \kappa_b \right) \right) \end{aligned} \quad (3.35)$$

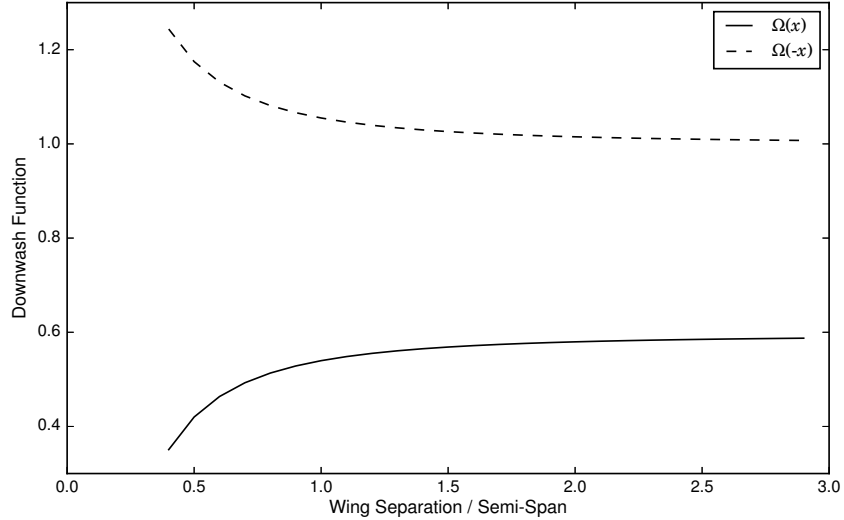


Figure 3.4: Variation of the downwash function for aft ($+\ell$) and fore ($-\ell$) relative spacings of the lifting surfaces. Zero vertical offset.

3.3.2 Implications of the simplified model

Using this simplified stability model, some of the unusual trends observed in Section 3.2 can be better understood and attributed to physical phenomena. The most significant observation from the parametric study was that the configuration with equal area wings and a centre of gravity located midway between the fore and aft wings' aerodynamic centres was inherently unstable. The source of this instability can be understood by examining (3.34) with an area ratio, Ψ , of 0.5 and zero centre of gravity offset, Δ . The static margin of such a configuration will only be positive if the downwash factor of the aft wing Ω_2 is greater than that of the fore wing Ω_1 . This will never be the case as the aft wing is subject to the downwash of the fore wing, decreasing its lift, while the fore wing is subject to the upwash of the aft wing, increasing its lift. This behaviour is illustrated by Figure 3.4 which plots the downwash function for both fore and aft wings over a range of staggers showing that, for all stagger positions, the aircraft is unstable.

Examining (3.34) there are three approaches to counteract the destabilizing effects of the persistent difference between the two downwash terms: (i) a

forward shift of the c.g. relative to the midpoint of the wings, decreasing Δ , (ii) decreasing the area ratio Ψ so that the fore wing has less influence and (iii) increasing the lift curve slope ratio, Φ_2/Φ_1 to make the lift on the aft wing more sensitive to the angle of attack. These approaches are among those identified by Wolkovitch [30] to promote equal loading on the fore and aft wings of joined-wing aircraft [30], see Section 2.2. In Lange *et al.*'s study of box-wing aircraft, the third of these approaches was used to design a stable box-wing aircraft with equal loading on the fore and aft wings. However, the lift curve slope was altered by varying the sweep angles of the fore and aft wing, leading to at least one wing not being swept sufficiently for optimal performance with respect to wave-drag effects. Therefore, this study has focused on how to use the first two approaches to achieve stability.

In a conventional aircraft, the longitudinal stability of an aircraft is positively influenced by increasing the separation between the wing and the horizontal tail. Increasing this separation reduces the effects of downwash on the horizontal tail and increases its moment arm, thereby increasing longitudinal stability. However, in Figure 3.3, the opposite trend was observed in the equal area wing design, with increased stagger of the box-wing making the aircraft *less* stable. The origin of this unexpected behaviour can be better understood by taking the derivative of (3.34) with respect to the dimensionless stagger, ℓ :

$$\frac{\partial \ell_{np}}{\partial \ell} = \underbrace{\left(\frac{b}{4\hat{c}}\right) \frac{(1-\Psi)\Phi_2\Omega_2 - \Psi\Phi_1\Omega_1}{\Psi\Phi_1\Omega_1 + (1-\Psi)\Phi_2\Omega_2}}_{f(\ell)} + \ell \underbrace{\frac{\partial}{\partial \ell} \left(\left(\frac{b}{4\hat{c}}\right) \frac{(1-\Psi)\Phi_2\Omega_2 - \Psi\Phi_1\Omega_1}{\Psi\Phi_1\Omega_1 + (1-\Psi)\Phi_2\Omega_2} \right)}_{\frac{\partial}{\partial \ell} f(\ell)} \quad (3.36)$$

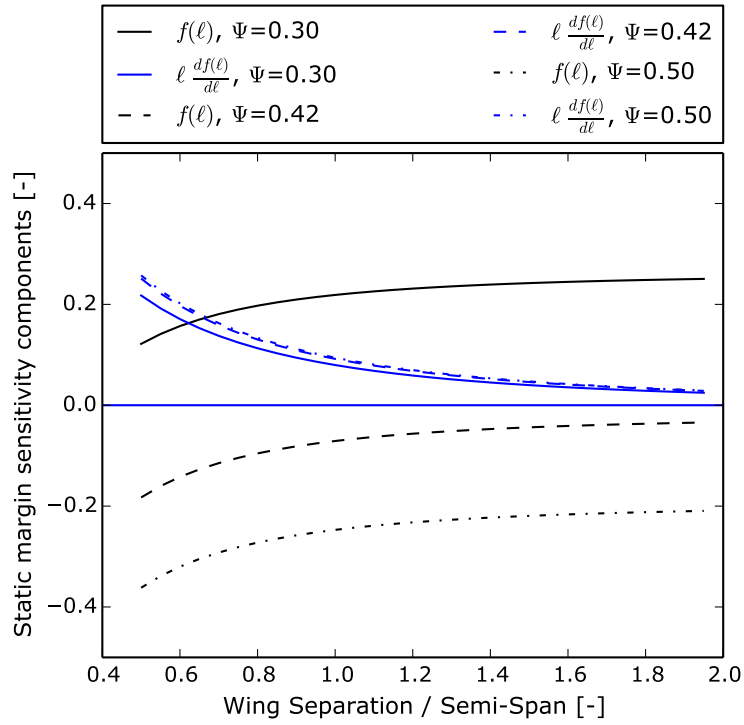
Since the Ω_i terms are an involved function of ℓ , the partial derivative of $f(\ell)$ is not expanded but its behaviour can be inferred from Figure 3.4. The difference between Ω_2 and Ω_1 is initially large and negative with a decreasing magnitude with increasing ℓ as both terms trend to a constant value. The derivative of this function takes the form of a positive value decreasing towards zero with increasing stagger. The physical mechanism underlying this behaviour is that each wing is increasingly less influenced by the normal wash of the other as the stagger increases. It is important to note that though the rate of change of $f(\ell)$ decreases towards zero, the value of $f(\ell)$ does not. This is due to the asymmetric nature of the expression for κ_p , (3.14). The limits of κ_p as ℓ goes to positive and negative infinity are different.

$$\begin{aligned} \lim_{\ell \rightarrow \infty} \kappa_p(\ell, 0) &= \frac{4}{\pi^2} \\ \lim_{\ell \rightarrow -\infty} \kappa_p(\ell, 0) &= 0 \end{aligned} \quad (3.37)$$

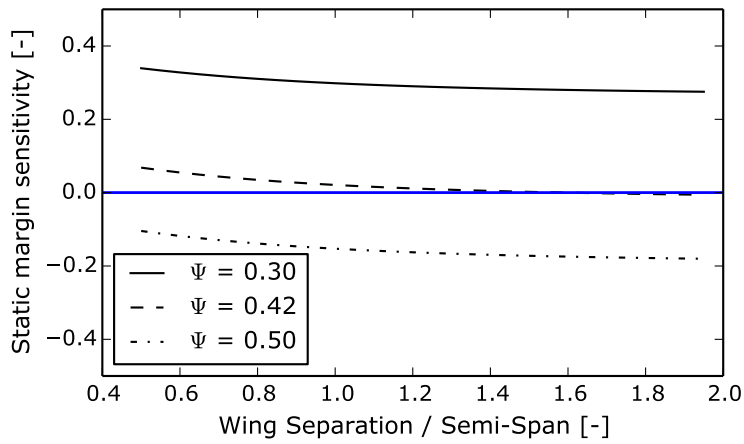
This behaviour has a physical meaning. The flow upstream is initially unperturbed but is influenced by the circulation of the wing as it approaches the leading edge. Downstream, the flow is both influenced by the wing's circulation as well as the circulation of the trailing vortices shed along the wing's entire trailing edge. In this inviscid and steady analysis, this causes a constant downwash persisting an infinite distance downstream, even once all the effects of the wing's circulation have dissipated. In reality, the downwash caused by the wing-tip vortices will decay to zero due to viscous and unsteady effects. However, this decay would be much slower than the rate of decrease of upwash so the behaviour of κ_p shown in (3.37) is a reasonable approximation of a real flow.

This behaviour can be related to the decrease of the static margin with increased separation. Considering the case where the wings are of equal area, $\Psi = 0.5$, the first term in (3.36) is non-zero and negative for all values of ℓ while the second term is positive for all values of ℓ and tends towards zero. The sensitivity of the neutral point will only be positive if the sum of both terms is greater than zero. For all values of ℓ , this is not the case, as shown in Figure 3.5a. Though the slope of $f(\ell)$ tends to zero with increasing ℓ , for designs with an area ratio greater than 0.42, the value of $f(\ell)$ tends towards a finite negative value as a result of the asymmetric downwash distribution. Though the magnitude of the instability and its sensitivity will be a function of the downwash model used in the analysis, these trends are independent of the downwash model.

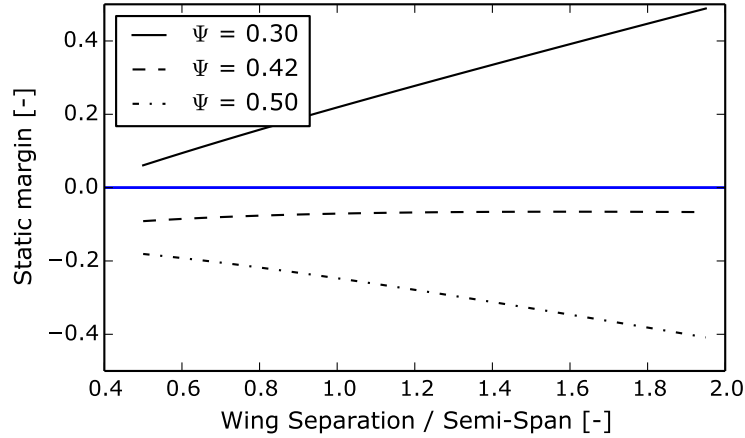
In taking the derivative of (3.34), the centre of gravity offset term, Δ disappears, leaving only the relative fore wing area and the ratio of lift curve slopes as variables to control the sensitivity of the static margin to stagger. As this analysis is constrained to designs with equal sweeps on both wings, the only parameter which can lead to a positive sensitivity is to decrease the relative fore wing area. The effect of changes to this ratio on the components of the sensitivity is shown in Figure 3.5a with the value of the sensitivity shown in Figure 3.5b. The resulting static margin for a design with zero centre of gravity offset is shown in Figure 3.5c. Decreasing the area of the fore wing decreases the downwash on the aft wing, decreasing the magnitude of the $f(\ell)$ term and allowing an increase of static margin with increasing separation for sufficiently small fore wing areas. The precise allocation of areas required for a positive sensitivity will be dependent on the aerodynamic model used. However, this behaviour has been related to a physical phenomenon, the asymmetric distribution of downwash upstream and downstream of a wing, so this trend should persist regardless of the details of the aerodynamic analysis used.



(a)



(b)



(c)

Figure 3.5: Effects of area ratio on the static margin and the sensitivity of static margin to stagger. (a) The two major components of the static margin sensitivity, shown in (3.36), $f(\ell)$ and $\ell \frac{\partial f(\ell)}{\partial \ell}$ (b) The total static margin sensitivity given by (3.36) (the sum of each curve in (a) for each area ratio). Area ratio of $\Psi = 0.42$ represents the division between positive and negative sensitivity. (c) The static margin for various values of area ratio, Ψ .

3.4 Summary

The analytic model for dual-wing stability was able to identify several important trends in the design of dual-wing configurations which should also be applicable to the design of box-wing aircraft. The distribution of area between the fore and aft wings was found to be an important parameter in the design. Reducing the area of the fore wing made the aircraft more stable but also increased the loading of the fore wing, making it more challenging to meet the manoeuvrability constraints on the design. Designs with wings of equal area required a forward shift in the centre of gravity location to achieve static stability which also increased the lift required from the fore wing, and impacted the ability for the aircraft to manoeuvre. The dual-wing configuration had a negative sensitivity of the static margin to increases in the separation of the two wings. This behaviour could be eliminated by reducing the relative area of the fore wing.

The trends in aerodynamic performance of the dual-wing were not necessarily applicable to the box-wing design as the induced drag caused by the

interference of the fore and aft wings was not predicted correctly by the biplane drag equation used in (3.22). For this reason, the aerodynamic performance of the box-wing must be examined using a more complex aerodynamic model to determine if there is a conflict between longitudinal stability and aerodynamic performance, as was observed for a dual-wing.

4 Parametric Analysis of Box-Wing Stability and Performance

The analytic study presented in Chapter 3 revealed several important trends in how the longitudinal stability of a box-wing was affected by changes to the planform geometry. However, the analytic study was limited in its ability to provide information on how the trim and stability requirements of a box-wing affected the configuration's aerodynamic performance. The analytic model used the biplane drag equation (2.1) to predict the induced drag due to the mutual interference of the wings. However, several studies have suggested that this model does not correctly model the induced drag of box-wing designs with different loads carried on each wing [16, 23, 36]. For this reason, a different aerodynamic model was needed, which is able to predict how the circulation distribution on a box-wing affects its aerodynamic performance. However, such a model requires significantly more detail about the wing's geometry. In particular, previous work has shown that the performance of joined-wing designs is dependent on the decalage angle between the wings [37], implying that there is an optimal distribution of the twist angle along both wings leading to the minimum drag design. In order to understand how the constraints of trim and stability affect the aerodynamic performance of a dual wing, a parametric study of box-wing geometries was performed using a vortex-panel aerodynamic model coupled to a gradient based optimizer to determine the optimal twist distribution for a feasible design.

4.1 Design of the parametric study

Three different parameters were considered for this study: the stagger of the wings, the height-to-span ratio, and the relative area of the fore wing. Unlike the investigation discussed in Section 3.2, the centre of gravity was not a

Table 4.1: Ranges of the parameters used in the study

Parameter	Bounds	
	Low	High
h/b	0.125	0.5
$2x_{1 \rightarrow 2}/b$	0.5	2.0
S_1/S_n	0.4	0.6

parameter in the study but was solved for during the optimization process to meet the minimum stability and trim requirements. The height-to-span ratio, however, was used as a parameter. Though analytic models are in agreement that the induced drag of a box-wing increases with increasing height-to-span ratio [7, 25], this does not consider the parasitic drag caused by the added wetted area introduced by the vertical wing segments. The trend of aerodynamic performance with height-to-span ratio when viscous effects are considered has not been the subject of previous aerodynamic investigations [7, 25].

The ranges of these three parameters are shown in Table 4.1. The bounds were chosen to encompass the range of wing designs which could be integrated into a transport aircraft design. The upper limit of stagger was chosen as the length of the reference aircraft's fuselage. The upper and lower limits on the area ratio were chosen based on the results of Chapter 3. Designs with area ratios less than 0.4 could not perform the required manoeuvre as the the fore wing was too highly loaded. The possibility also existed that designs with a smaller aft wing may have performance advantages. Therefore, the bounds of 0.4 and 0.6 were chosen as they would encompass the best box-wing configurations. The reference aircraft was based on the areas and weights of the Bombardier CRJ-200, as in Chapter 3. The box-wing designs considered in this parametric study had the same projected area and cruise weight as the reference aircraft, given in Table 3.1.

The aerodynamic forces and moments on the aircraft were evaluated by a vortex panel aerodynamic model which was able to solve for the induced drag of the nonplanar box-wing design. More details of this model are given in Section 6.2.4 and Annex A. The aerofoil section properties used in this analysis are given in Table 3.2.

The geometries used in the parametric study were similar to those used in Chapter 3 but with some minor modifications needed to properly model the vertical wing segment joining the fore and aft wings. Representative geometries spanning the range of parameters are shown in Figure 4.1. The wings were swept such that the leading edge, rather than quarter chord point, of both wing tips were at the same streamwise station. In all designs, the fore

4.1. Design of the parametric study

wing swept aft and the aft wing swept forward. The taper of the wing was variable in this analysis rather than fixed. The taper of the smallest wing was variable and the vertical wing had a taper of unity. The taper of the larger wing was calculated to have the same tip chord length as the vertical segment.

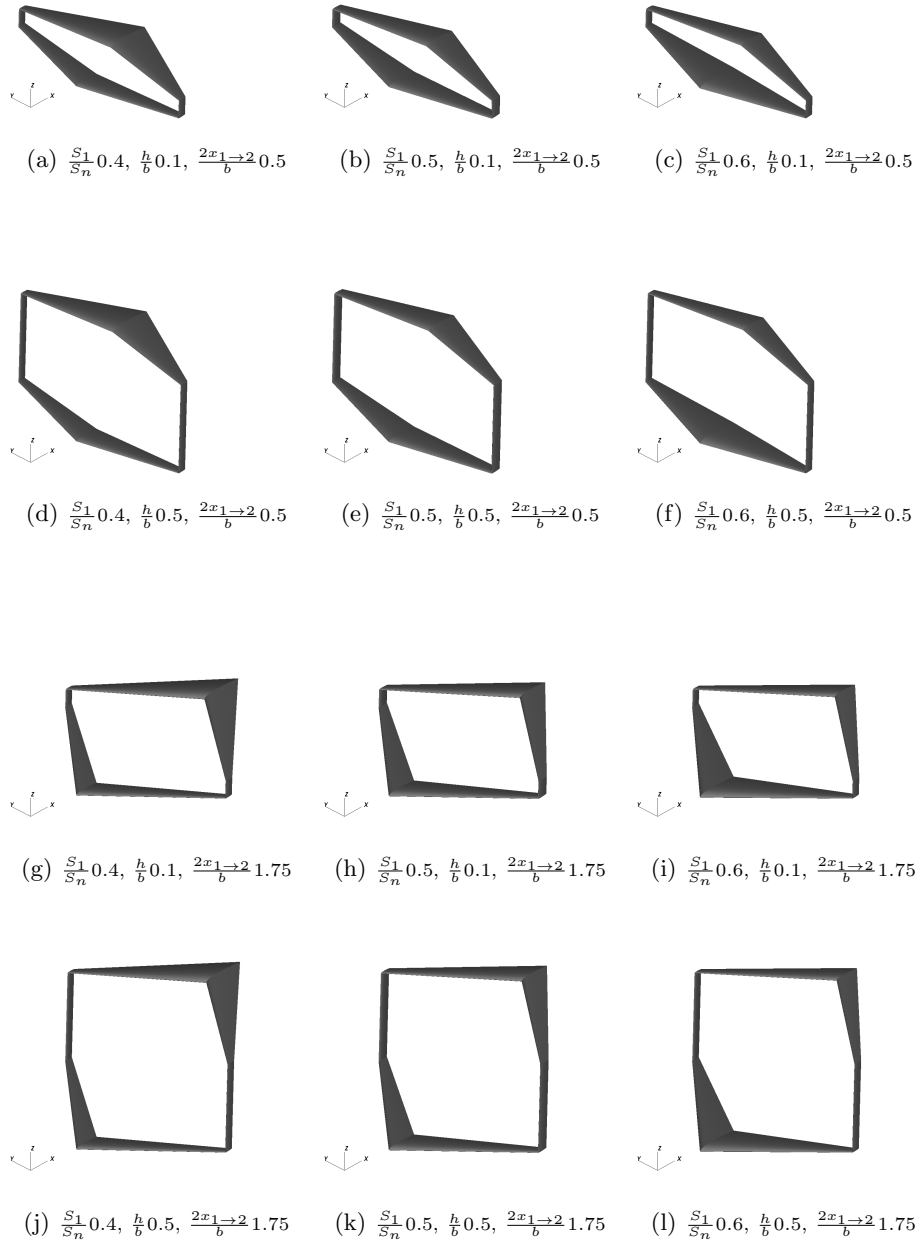


Figure 4.1: Representative box-wing geometries. Small wing taper of 0.325.

4.2 Optimization problem

Each geometry in the parametric study had a unique optimal twist distribution. Therefore, a constrained optimization problem was developed to determine this optimal distribution while maintaining static longitudinal stability and trim. The optimization problem formulation is:

$$\begin{aligned}
 & \max \frac{C_L}{C_D} \\
 & \text{such that } \begin{cases} 1.0g & \begin{cases} C_L & = & C_W \\ C_m & = & 0 \\ -\frac{C_{m\alpha}}{C_{L\alpha}} & > & 0.07 \end{cases} \\ 2.5g & \begin{cases} C_L & = & 2.5C_W \\ C_{l,i} & < & C_{l_{max}i} - 0.05 \end{cases} \end{cases} \quad \{i \in 1 \dots n_{pan}\} \\
 & \text{with respect to } \left\{ \gamma_i \{i \in 1 \dots n_{seg} + 1\}, \frac{\Delta_{c.g.}}{\bar{c}}, \alpha_{mvr}, \lambda \right.
 \end{aligned} \tag{4.1}$$

The box-wing model consisted of five lifting segments, n_{seg} , whose twist angle, γ_i , could be set at both the root and the tip. The twist distribution was continuous along the wing so there were six independent twist values. The first value set the twist of the fore wing at its root and the sixth value set the wing root twist of the aft wing. In addition to the wing twist angles, the optimization problem had three other variables. The centre of gravity offset, $\Delta_{c.g.}$, shown in Figure 2.1, was needed to meet the stability constraints. The taper, λ , of the smallest wing was varied to meet the manoeuvrability constraints which were critical at the wing tip. The manoeuvre incidence, α_{mvr} , was also a variable to reduce the execution time of the objective function. The ranges and initial estimates for these variables are shown in Table 4.2.

Longitudinal stability was enforced by constraining the design to have zero pitching moment at cruise and a static margin of 7%, typical of transport aircraft [58, 67]. The ability of the aircraft to perform a 2.5g manoeuvre was enforced by ensuring that no wing panel exceeded its maximum local lift coefficient.

4.2.1 Optimizers

The gradient based SQP optimization algorithm, SNOPT [68], implemented in the pyOpt optimization framework [69] was used to solve the optimization problem given by (4.1). The feasibility tolerance of the SNOPT algorithm was 2×10^{-6} and the optimality tolerance was 5×10^{-6} . Gradients were evaluated using a finite difference approximation.

Table 4.2: Variable bounds and initial values for the optimization problem

		Lower bound	Upper bound	Initial value
$\gamma_i \{i \in 1 \dots n_{seg} + 1\}$	[deg]	-20.0	20.0	1.0
$\frac{\Delta c.g.}{\bar{c}}$	[-]	-2.0	2.0	0.0
α_{mvr}	[deg]	0.0	20.0	2.5
λ	[-]	0.2	1.0	0.4

4.3 Results

4.3.1 Reference wing

The reference aircraft wing was modelled as a planar, trapezoidal planform. The three angles making up the reference wing’s twist distribution, as well as the wing’s taper, were optimized using the same problem formulation as the box-wing designs. The stability constraints were not enforced as the horizontal tail of the reference aircraft was not modelled. Figure 4.2b shows the spanwise distribution of the lift forces at cruise normalized by the total wing area, *i.e.* $\frac{C_l}{S_n}$. Figure 4.2c shows the lift forces during a manoeuvre normalized by the local chord, *i.e.* $\frac{C_l}{c}$. The spanwise distribution of total lift force along the wing at cruise followed the elliptical profile closely. During the 2.5 *g* manoeuvre, the local lift coefficient reached its maximum value at a spanwise station near the wing-tip. The wing was able to perform the manoeuvre without any local stalling. The lift-to-drag ratio of the wing in isolation was 25.88. However, the wing required a horizontal tail to maintain static stability which created both induced and parasitic drag. As the twist of the box-wing was designed to cruise with zero pitching moment, it was assumed that the reference aircraft was likewise designed so that, at the start of cruise, the horizontal tail would generate no lift. Therefore, only the parasitic drag of the horizontal tail was considered. This contribution to the wing’s total drag was estimated using the analytic method presented in [70]. The parasitic drag of the horizontal tail reduced the lift-to-drag ratio of the reference wing to 22.14.

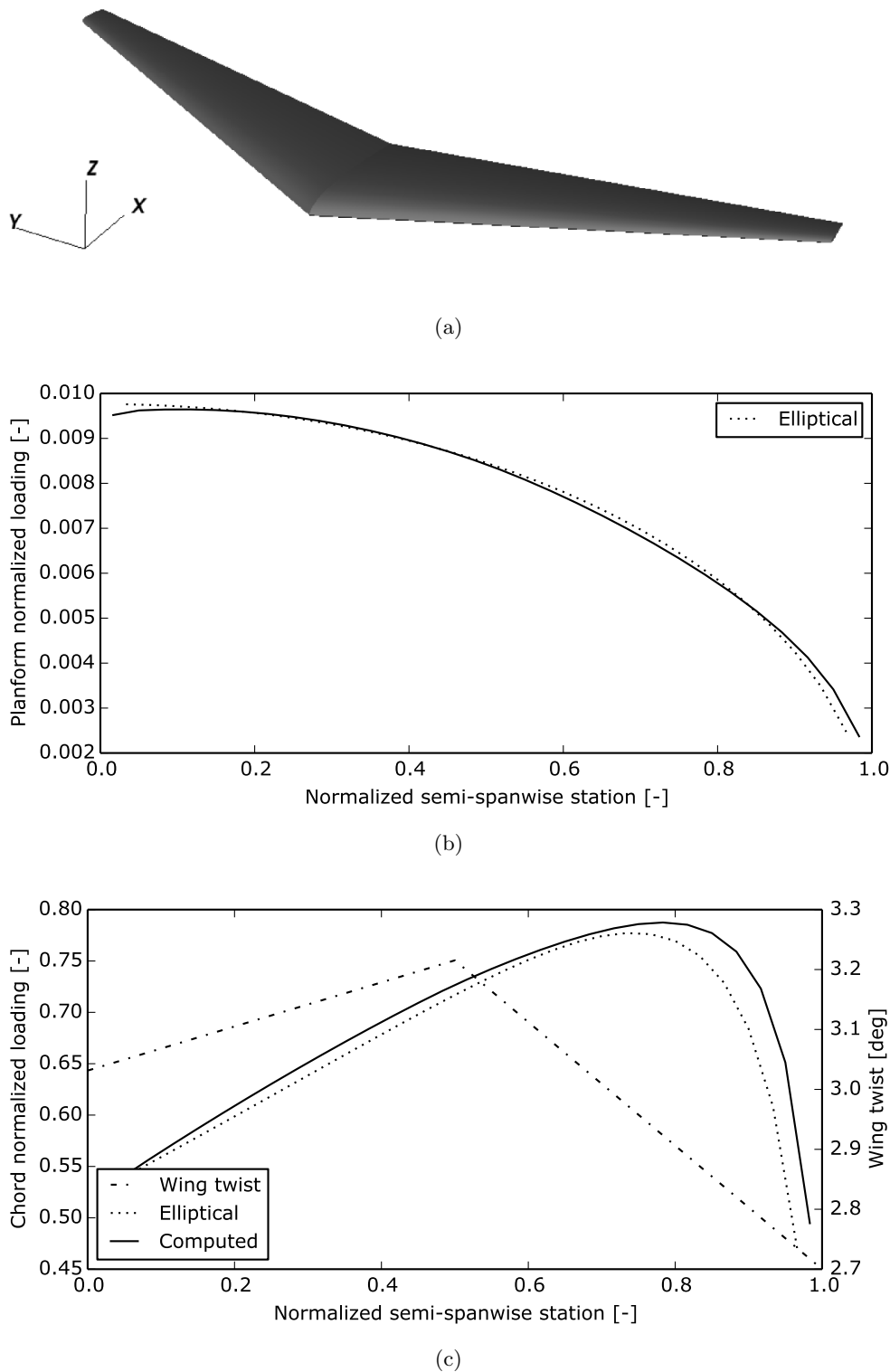


Figure 4.2: Geometry and loading of the planar reference wing. The optimized taper ratio was 0.2475. The planform normalized loading showed the local lift force generated by each vortex panel normalized by the total wing area during 1 g flight *i.e.* $\frac{l}{qS_n}$. The chord normalized loading showed the local lift force on each vortex panel normalized by the mean chord of that panel during a 2.5 g manoeuvre *i.e.* $\frac{l}{qc}$.

4.3.2 Parametric study

The results of the parametric study are shown in Figure 4.3 as a carpet plot. The single dependent variable was the lift-to-drag ratio of the box-wing designs. The lift-to-drag ratio of the reference wing and horizontal tail is shown as a hatched line. Designs with large stagger and a height-to-span ratio 0.25 or greater had superior aerodynamic performance to the reference aircraft, showing that even when the requirements of static stability were considered, many box-wing designs were superior to conventional aircraft.

Previous studies, which considered the effects of height-to-span ratio on the induced drag of a box-wing design, have concluded that the induced drag of a wing decreases continuously with increasing separation, asymptotically approaching half the induced drag of a monoplane [7]. The data in Figure 4.3 show a similar trend despite the increased wetted area introduced by the vertical wing segments as the height-to-span ratio increased. The increased wetted area only began to penalize the design at height-to-span ratios greater than 0.5.

To better understand the trends in stability and aerodynamic performance of the box-wing designs, additional data are provided in Table 4.3 for six wing designs which spanned the range of the three variable parameters; all designs presented in this table had a static margin of 7% and zero pitching moment. Since the static margin was fixed, the degree of static stability of the design was quantified by the shift in the centre of gravity required to achieve the desired static margin. The data in Table 4.3 show the same trends identified in the analytic study presented in Chapter 3. As the fore wing area was reduced, the aircraft became more stable, requiring a smaller shift in the centre of gravity to meet the static margin constraint. For designs with an area ratio greater than 0.4, increasing the stagger made the aircraft less stable, while for the 0.4 area ratio design, the aircraft became more stable with increased stagger. The origin of this behaviour is discussed in Section 3.3.

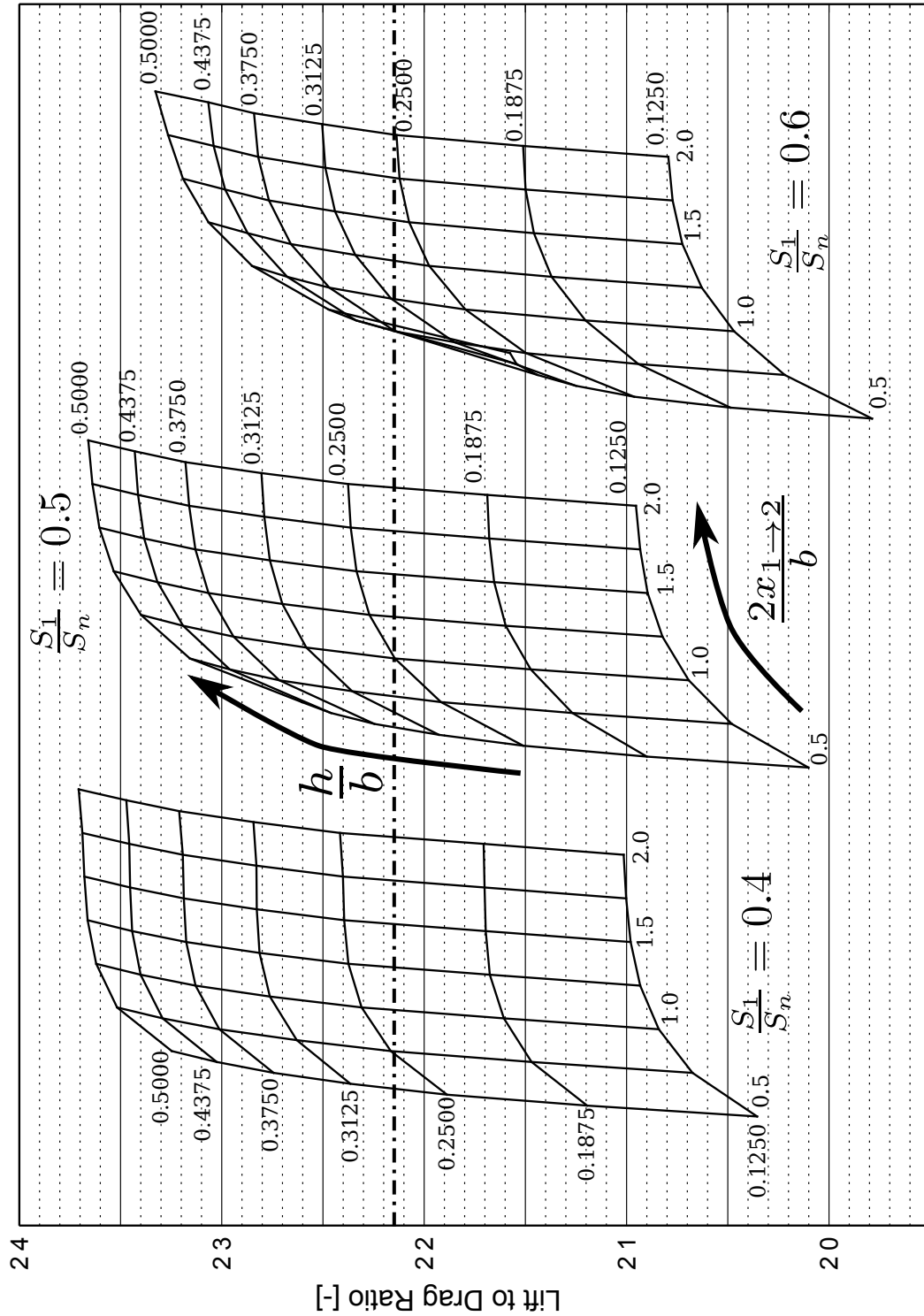


Figure 4.3: Parametric study of box-wing geometry with static longitudinal stability and trim constraints. Parameters are: Normalized fore wing area, $\frac{S_1}{S_n}$, Normalized quarter-chord stagger $\frac{2x_1-2}{b}$ and height-to-span ratio $\frac{h}{b}$.

Table 4.3: Properties of best and worst optimized box-wing designs

$\frac{S_1}{S_n}$ $2x_{1 \rightarrow 2}/b$	0.4		0.5		0.6	
	0.5	1.75	0.5	1.75	0.5	1.75
Height-to-span [-]	0.5	0.5	0.5	0.5	0.5	0.5
Lift-to-drag [-]	23.25	23.69	22.60	23.64	21.58	23.27
Offset of c.g. [\bar{c}]	-0.045	0.034	-0.097	-0.113	-0.148	-0.309
Fore to aft lift [-]	1.249	0.906	2.053	1.235	3.509	1.819
Induced drag [dct]*	82	84	84	81	92	85
Parasitic drag [dct]*	116	111	120	114	121	113

* ‘dct’ is a *drag count*, defined as $C_D \times 10^4$.

Decreasing the area of the fore wing and increasing the stagger both had the effect of making the lift forces carried by each wing more equal. The former made the aircraft more stable necessitating a smaller centre of gravity offset while the latter made each wing more effective in generating the moments needed to trim the aircraft. The more equal lift distribution between the wings led to higher aerodynamic performance. This was due both to changes in induced and parasitic drag. The parasitic drag of each aerofoil was parabolic with respect to the section lift coefficient to reflect the increased pressure drag as the aerofoil’s local angle of attack increased to produce larger lift forces. Designs with more equal loading between the wings avoided highly loaded aerofoil sections with high parasitic drag. If the biplane drag equation (2.1) is used to estimate the induced drag of a box-wing, the minimum occurs when the both wings carry equal lift [21, 22].

Though it has been shown that the minimum induced drag of biplane and box-wing designs occurs when the ratio of fore to aft wing lift forces is unity, the multiplane drag equation has a low sensitivity to small changes to this ratio. Figure 4.4 shows the variation of induced drag for ratios of fore to aft lift force between 0.5 and 2. Though optimized designs with a stagger of 1.75 did not maintain equal loading on fore and aft wings, the ratio of fore to aft lift forces was approximately 1.2 for the equal area configuration. From the trends shown in Figure 4.4, the induced drag would increase by only 2%, leading to only a 0.8% increase in total drag. The penalty incurred by maintaining trim and static stability was negligibly small. This was why the best aerodynamic performance of the 0.5 area ratio wing was almost the same as that of the 0.4 area ratio wing, though the latter configuration had been shown to be more stable in Chapter 3. However, the induced drag penalty

was a parabolic function of the lift imbalance. Designs with a greater lift imbalance between the wings, such as the 0.6 area ratio wings, incurred a more significant penalty due to the requirements of stability and trim. The inviscid analytic model of Demasi *et al.* [23] predicted that the induced drag of an unstaggered box-wing design would be independent of the fraction of the total lift generated by each wing. However, the results of the parametric study shown in Figure 4.3 indicate that Prandtl's original equation for predicting induced drag of box-wings and biplanes, (2.1) better represents the trends of a staggered box-wing design. These findings also show that the induced drag results from the parametric study in Chapter 3 were applicable to box-wing configurations as well as dual wings.

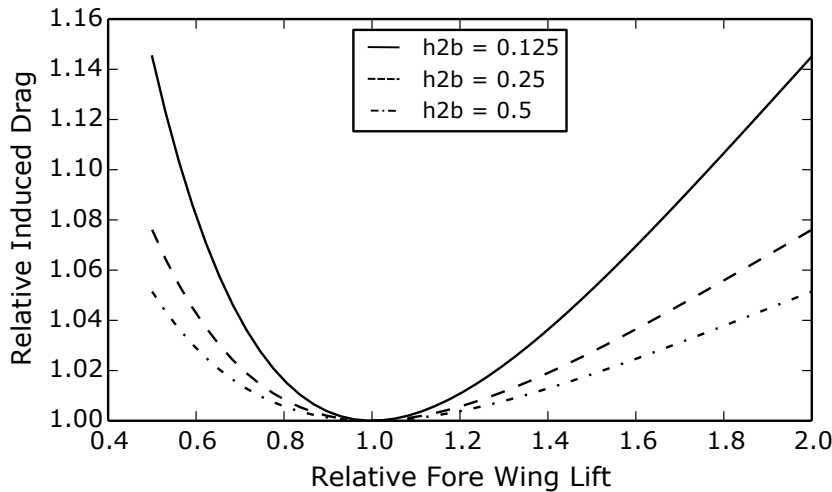


Figure 4.4: Sensitivity of the induced drag of a box-wing to changes in the relative lift force of the fore wing for a range of vertical separations of the wings, as predicted by Prandtl's multiplane drag equation.

The trends shown in Table 4.3 and Figure 4.3 demonstrate that the requirements of static stability and trim did impose an aerodynamic penalty on a box-wing aircraft. However, for highly staggered designs, the aerodynamic penalty was negligibly small. When the stagger of the wings was reduced, the required lift on each wing became less equal and the aerodynamic penalty imposed by stability and control made the box-wing design less preferable. These results indicate that box-wing aircraft can retain a significant performance advantage over conventional designs even when the constraints of static stability and trim are enforced.

4.3.3 Wing loading

The spanwise loading of one of the highest performing designs identified in Figure 4.3 is shown in Figure 4.5. The data are presented using two different normalizations. In Figure 4.5a, the local lift force at cruise for each panel is normalized by the reference area of the entire wing to show the distribution of the lift force along the wing. In Figure 4.5b, the local force is normalized by the local chord to show the local lift coefficient in a $2.5g$ manoeuvre on each aerofoil.

The spanwise distribution of lift force shown in Figure 4.5a follows an almost elliptical distribution except at the wing tips. On both the fore and aft wings, the local lift force was greater than for an elliptical distribution, as expected from the ideal box-wing circulation distribution shown in Figure 2.3 as the circulation does not need to decrease to zero at the wing tip.

The local lift coefficient during manoeuvre showed that the most critical aerofoil section for stall was located at the fore wing-tip. This was also where the wing had its minimum chord and thus Reynolds number. The effects of the low Reynolds number on the local maximum lift coefficient may be important at this location.

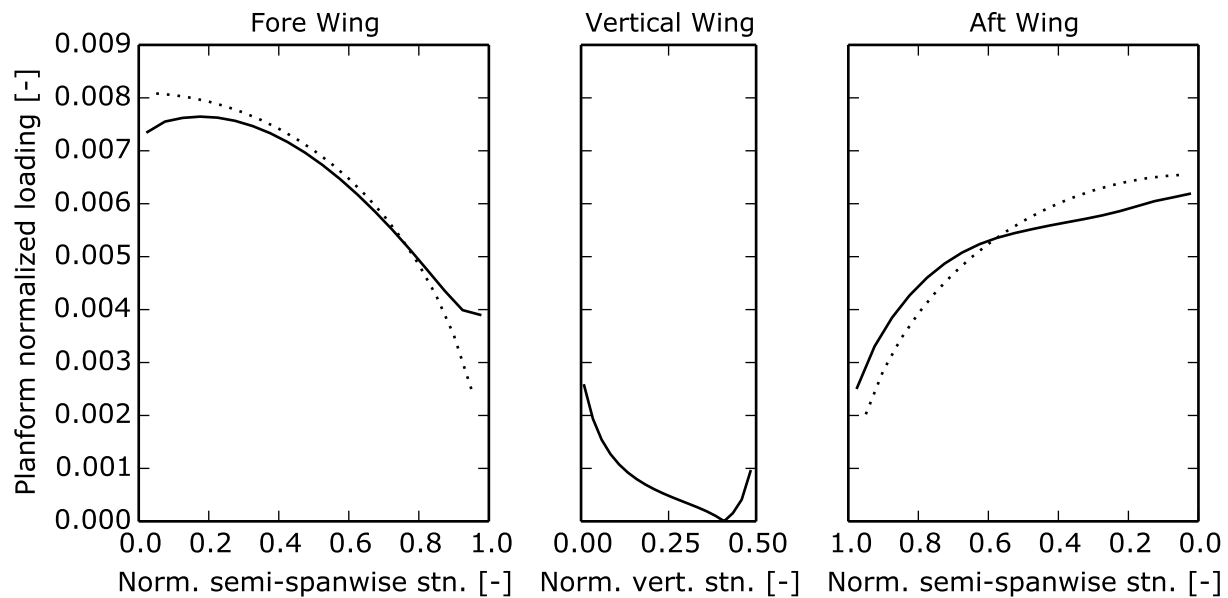
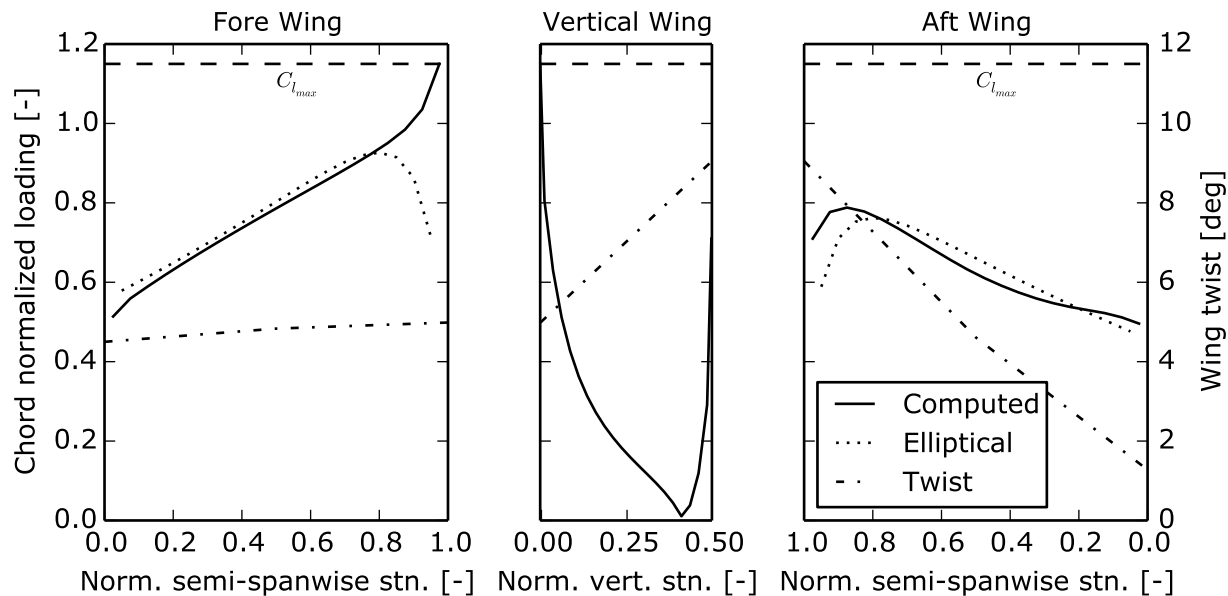
(a) Total loading at cruise, $L = W$ (b) Local loading at manoeuvre, $L = 2.5W$

Figure 4.5: Loading of a box-wing configuration with a high lift-to-drag ratio. Normalized fore wing area, 0.5. Normalized quarter-chord stagger, 1.75, height-to-span, 0.5. Fore wing taper, 0.2. The planform normalized loading showed the local lift force generated by each vortex panel normalized by the total wing area during $1g$ flight *i.e.* $\frac{l}{qS_n}$. The chord normalized loading showed the local lift force on each vortex panel normalized by the mean chord of that panel during a $2.5g$ manoeuvre *i.e.* $\frac{l}{qc}$. *Note:* The loading on the vertical wing is plotted as an absolute value as it changes sign along the span.

4.4 Summary

This parametric study highlighted important interactions between the disciplines of aerodynamics and stability in the design of box-wing aircraft. The trends observed in Chapter 3 between the planform shape of the wing and static longitudinal stability persisted in an analysis using a more detailed aerodynamic model. For highly staggered designs, the aerodynamic penalty incurred by maintaining static stability was negligibly small. This penalty grew, however, as the stagger was reduced, to the point where the box-wing had no aerodynamic advantage over a conventional wing. The trends indicate that the best box-wing designs have significant streamwise and vertical separation. The structural implications of such a configuration are unknown and a more detailed study of box-wing structures will be discussed in the following chapter to determine if such a design is structurally feasible. In addition, the centre of gravity location was a variable in this analysis while in a real aircraft configuration, the centre of gravity location will be highly influenced by other non-aerodynamic requirements on the design. For these reasons, the aerodynamics and stability of a box-wing design will be re-examined in a multidisciplinary study, presented in Chapters 6 and 7.

5 Wing Weight Estimation for Box-Wing Configurations

The parametric study in Chapter 4 identified box-wing planform geometries which had superior aerodynamic performance to conventional designs while also meeting the stability and trim requirements at cruise. However, this study did not consider what the structural implications of such designs are and whether the box-wing configuration has an advantage or penalty in terms of structural weight.

Previous investigations of box-wing aircraft have shown that this unconventional aircraft design does not increase the structural weight of the wing-system compared to a conventional cantilevered wing with a horizontal tail [9, 8, 52]. However, these studies investigated single point designs, and did not investigate the effect of changes to the box-wing's planform shape on structural weight of the wing. In these previous studies of box-wings, only one geometric parameter, the sweep of the vertical wing segment, was investigated with respect to its effect on the wing's weight, and the design was found to be insensitive to this parameter [51]. When investigating the design of conventional aircraft wings, there are several wing weight models, of varying complexity, which estimate the weight of the wing structure as functions of the wing's planform shape. However, the statically indeterminate structure of the box-wing is fundamentally different than a cantilevered monoplane as the relationship between external loads and internal forces is statically indeterminate. For this reason, relationships used for cantilevered aircraft wings cannot be easily extended to predict the weight of a box-wing aircraft. A comparison of different approaches for predicting aircraft wing weight is made in Section 5.1. A novel wing weight model is developed in Section 5.2. This model is validated against a set of existing conventional aircraft in Section 5.3. This model is then used to investigate the general structural behaviour of a box-wing in Section 5.4.

5.1 Existing wing weight models

Existing models for the weight of conventional aircraft wings vary in terms of the amount of information needed by the analysis. Class I models are based on historical trends for the weight of the wing relative to the maximum takeoff weight of the aircraft for various types of aircraft missions [65]. Class II models predict the weight of the wing based on a small set of high level parameters such as the planform area, aspect ratio and sweep. These models are appropriate for very early design stages; Raymer [67], Howe [71] and Roskam [65] provide such models for conventional aircraft.

There are more advanced class II models, termed class II- $\frac{1}{2}$ by some authors [72]. Such models require more details about the wing's design so the analysis is driven more by the underlying physics of the wing than by empirical modelling and the results are more sensitive to design choices. Examples of such models are those of Torenbeek [73], Ardema [74], Liu and Anemaat [75], Elham *et al.* [72] and Petermeier *et al.* [76]. Though the exact details of these models differ, they all follow a similar approach, itemized below:

- Determine the aerodynamic loads at one or more critical operational points.
- Calculate the resulting local bending moments and shear forces.
- Determine the allowable stresses.
- Create a relationship between the wing-box size and the maximum local stresses.
- Size the wing-box to be fully stressed at the most critical design point, with applicable safety factors.
- Add additional weight to account for structural components not associated with the primary structure.

More complex than these are Class III models, which model the individual structural members of the wing as separate structural finite elements. Aerodynamic loads are modelled using a solution of either the Euler or Navier Stokes equations of the flow over the aircraft. Such models are sensitive to small changes in the aircraft design and have been used to optimize the design of conventional aircraft [77]. However, due to the computational resources required, such models can only consider a small range of planform shape variations.

This chapter presents the development of a Class II- $\frac{1}{2}$ wing weight model which is able to solve the statically indeterminate structure of a box-wing configuration. This was accomplished using an equivalent beam finite element model which discretized the wing into a series of beam elements with cross-sectional properties derived from the aerofoil shape. Previous studies

have used various approaches to relate the internal structure of the wing-box to the properties of an equivalent beam element. Examples of some of the idealizations which have been used are shown in Figure 5.1.

The simplest wing-box idealization, shown in Figure 5.1a, is a hollow tube of variable thickness, used in a previous aerostructural study of nonplanar wing aircraft [49]. Other investigations have used two solid plates which are of unequal thickness but symmetrically offset from the aerofoil chord line by a characteristic displacement. This displacement is an empirical constant related to the aerofoil geometry and varies between investigations [72, 78]. This idealization of the wing-box cross section, shown in Figure 5.1b, is only able to predict the material required to resist bending forces. In order to predict the material needed to resist shear loads, other authors have included vertical segments to represent the fore and aft spars [79, 80]. This idealization shown in Figure 5.1c can resist shear, bending and torsion, though it is still dependant on empirical relations to determine the characteristic height of the wing-box. Other authors have divided the wing's structure into a four boom and four skin wing-box where the booms carry all the direct stress and the skins carry all the shear and torsion [28, 48, 81]. This idealization, shown in Figure 5.1d, allocates area to the cross section in a similar manner as a real wing-box but remains dependent on an empirical relation for the wing-box height.

The wing weight model developed in this chapter used an aerofoil conforming boom and skin hexagon to represent the wing-box structure, shown in Figure 5.1e. Other authors [78] considered a hexagonal cross section of uniform thickness and showed that it was the cross section best able to predict the ability of the wing-box to resist torsion, as well as direct and shear stresses [78]. By dividing the cross sectional area into direct stress carrying booms and shear stress carrying skins, the present aerofoil section uses the cross-sectional area more efficiently to resist the applied loads than the uniform thickness used in previous studies [78]. The geometry of the cross section is defined by the shape of the aerofoil itself, eliminating the need for an empirical factor for the thickness.

5.2 Fully stressed algorithm

The wing weight prediction model presented in this chapter differed from previous approaches as it was able to model the statically indeterminate structure of a box-wing and used an idealization of the wing-box cross section which was representative of the material distribution in a real wing and which did not depend on empirical coefficients. Rather than perform an optimization for minimum structural weight, a fully stressed approach was used to predict the

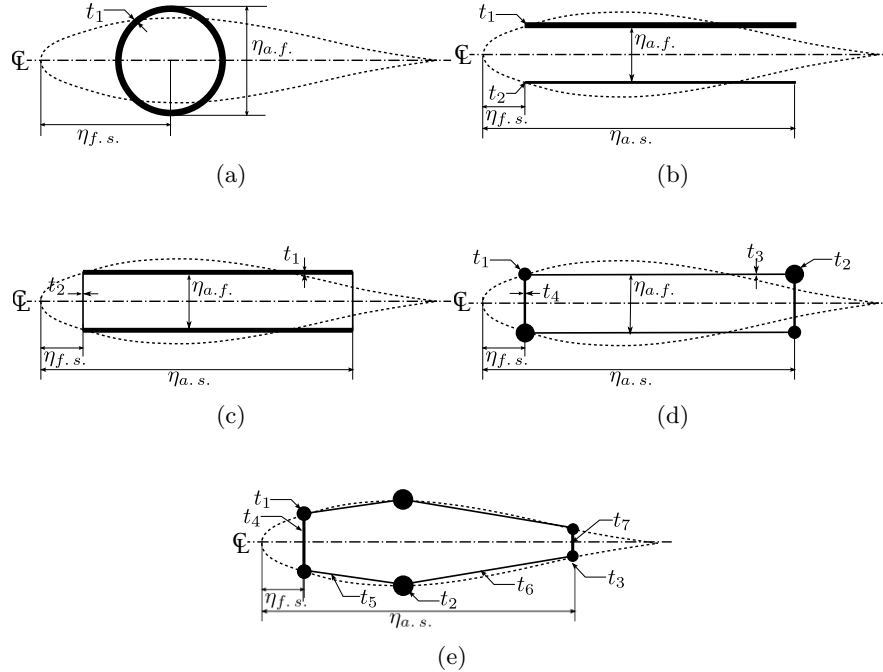


Figure 5.1: Alternate wing-box internal structure idealizations.

wing weight. Previous studies have compared a fully stressed solution to a minimum weight optimization and found that the solutions differed by only 2% with the minimum weight optimization while taking an order of magnitude more computational resources [81]. This made the fully stressed approach ideal for a conceptual design study.

The wing weight prediction algorithm followed the steps of a Class II- $\frac{1}{2}$ analysis, given in Section 5.1. A flowchart of the algorithm is given in Figure 5.2. Aerodynamic loads were computed once, at the start of the analysis, for each load case the model considered. Details of the aerodynamic model are given in Section 5.2.2. These loads were used by the structural finite element model, discussed in Section 5.2.1, to predict the internal forces and moments in each cross section. Based on these internal forces and moments, the seven variable thicknesses and areas of the cross section were sized to be as close as possible to their allowable stress using the methodology presented in Section 5.2.3. Since the structure was statically indeterminate, the changes to the cross-sectional properties changed the structural stiffness, so this process was repeated until the cross-sectional variables converged to a specified tolerance.

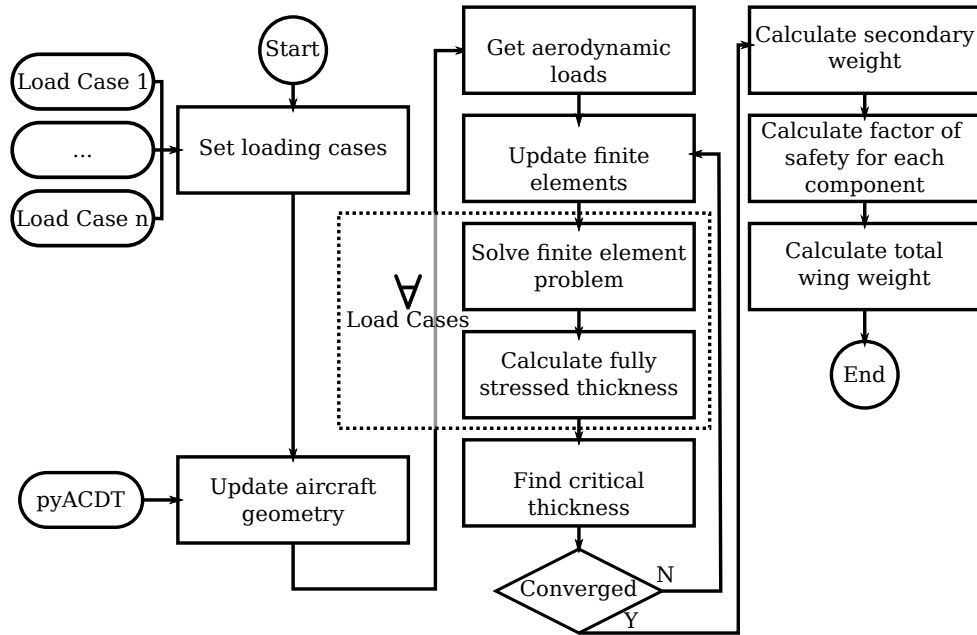


Figure 5.2: Flowchart for the fully stressed structural weight prediction algorithm. The aircraft geometry was defined by the pyACDT toolbox [82], discussed further in Chapter 6.

Once the size of the primary structure was determined, the weight of the secondary structure was estimated using empirical methods, Section 5.2.5, allowing the weight of the entire wing structure to be estimated. The following sections provide more detail on this analysis.

5.2.1 Structural model

A structural finite element model was used to determine the internal forces and loads of the statically indeterminate box-wing structure. The wing was modelled as a series of two-node beam elements, with six degrees of freedom per node. Each beam element passed through the elastic axis of the structural cross section. The section properties of the beam were derived from the aerofoil conforming boom and skin hexagon cross section which was itself a function of the aerofoil geometry as well as six variables for boom area and skin thickness. The present analysis used a custom finite element code, initially developed by Jansen *et al.* [49] and modified to make use of the unique cross section.

5.2.2 Aerodynamic model

The aerodynamic forces were predicted by the same vortex panel model used for the parametric study in Chapter 4. Validation studies of this model's ability to predict both conventional and unconventional aircraft are given in Annex A. The effects of viscous drag as well as aerofoil camber were accounted for by using aerofoil section data, computed *a priori*.

The aerodynamic model used the same spanwise discretization as the structural model to divide the wing into a series of vortex rings, spanning the wing chord, each paired to a wake vortex ring. The vortex panels and beam elements of a cantilevered wing are shown in Figure 5.3. The aerodynamic forces were represented as three force components located at the midpoint of the quarter-chord line of the vortex panel and aligned with the global coordinate system. The elastic axis of the structural cross section was located aft of the quarter-chord point so the combination of the aerofoil section pitching moment and the displaced aerodynamic forces created a torsional force on the beam element.

The aerodynamic loads were scaled by a gust-load coefficient which accounted for the additional loading by a standard gust. Only manoeuvre loading was considered in the present investigation so the gust loading was calculated for 2.5 *g* manoeuvre conditions using the relations presented by Torenbeek [73]. A gust relief factor of 0.8 was used in the calculation of the gust load.

5.2.3 Fully stressed hexagonal cross section

An aerofoil conforming boom-and-skin hexagon was used to model the internal distribution of the area within the wing-box. The properties of this cross section and the algorithm to determine the fully stressed thicknesses of the cross section will be discussed in this section. The boom-and-skin hexagon is shown in Figure 5.4. To make the analysis tractable, the hexagon was assumed to be symmetric along the chord line. Boom 6 was located at the point of maximum displacement from the chordline on the suction surface. In a symmetric aerofoil, this would make boom 3 conform to the aerofoil contour. In the case of a cambered aerofoil, boom 3 would not be located on the pressure surface of the aerofoil.

The centre of area of the section was calculated using (5.1). Since only the booms resisted the direct stress due to bending, the skins were not included

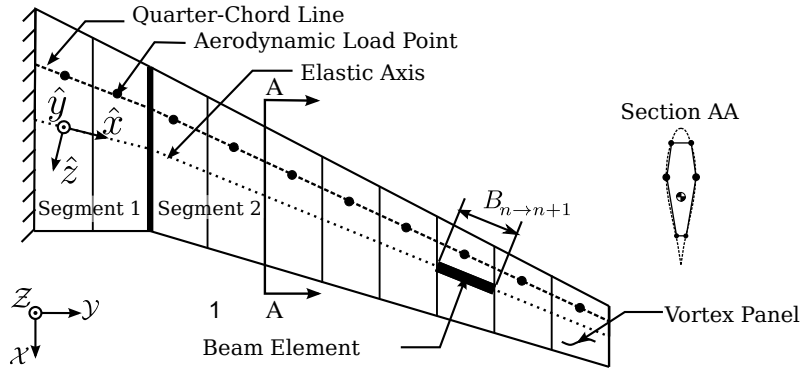


Figure 5.3: Details of the discretization of a typical cantilevered wing. Section AA shows an aerofoil conforming boom and skin hexagon cross section which is made up of seven structural thicknesses: three unique boom areas and four unique skin thicknesses. The aircraft coordinate system is shown in the lower left corner and the local element co-ordinate system is shown attached to the first equivalent-beam element.

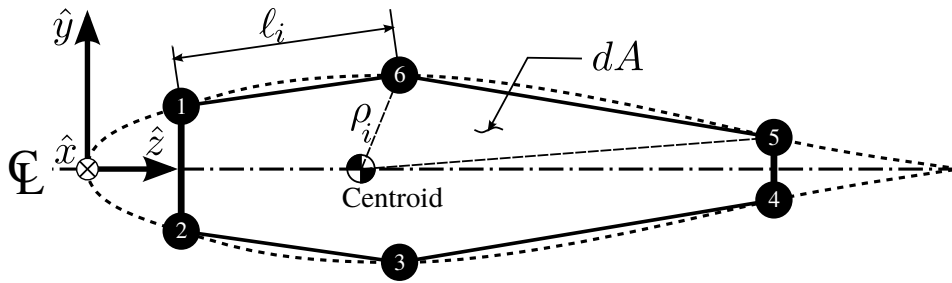


Figure 5.4: Details of the aerofoil conforming boom and skin hexagon. Booms are numbered as shown, skins are numbered with 1 as the fore spar and continuing counter-clockwise.

in the calculation of the centre of area.

$$\bar{z} = \frac{\sum_{i=1}^6 A_i \hat{z}_i}{\sum_{i=1}^6 A_i} \quad (5.1)$$

$$\bar{y} = \frac{\sum_{i=1}^6 A_i \hat{y}_i}{\sum_{i=1}^6 A_i} \quad (5.2)$$

The second moment of area in the local beam coordinates was given by (5.3). The booms were treated as concentrated areas located at a distance from the centre of area.

$$I_{zz} = \sum_{i=1}^6 A_i (\hat{y}_i - \bar{y})^2 \quad (5.3)$$

$$I_{yy} = \sum_{i=1}^6 A_i (\hat{z}_i - \bar{z})^2 \quad (5.4)$$

The effective torsional stiffness was calculated based only on the shear resisting material using thin-walled beam theory [83].

$$J = \frac{4 \left(\sum_{i=1}^6 dA_i \right)^2}{\sum_{i=1}^6 \ell_i / t_i} \quad (5.5)$$

The location of the elastic axis and shear centre were considered coincident with the centre of area. This was an approximation; in reality the shear centre could be displaced from the centre of area depending on the thickness distribution of the cross section. However, this level of complexity was not needed in the current analysis as neither static nor dynamic aero-elastic effects were considered.

The fully stressed structural thicknesses were determined in a two step process; the boom areas required to resist the normal and bending stress were calculated, then the shear flow resulting from this area distribution was calculated. This process is shown in Figure 5.2. The six-boom cross section presented a challenge as there was no unique solution to the allocation of area

between the booms to achieve a fully stressed structure. To make the problem tractable, it was assumed that the required boom area was proportional to the distance of the boom from the centre of area, as shown in (5.6).

$$A_i = \Phi \zeta_i \quad (5.6)$$

where Φ , in this chapter, was the rate of change of boom area with total distance from the centre of area, ζ , given by (5.7).

$$\zeta_i = \sqrt{(\hat{z}_i - \bar{z})^2 + (\hat{y}_i - \bar{y})^2} \quad (5.7)$$

This assumed area distribution was reasonable as the direct stress due to bending is proportional to the distance from the neutral axis which was coincident with the centre of area and, for this symmetric cross section, aligned with the principal axes shown in Figure 5.3. By substituting (5.6) and (5.7) into (5.3), (5.4) and the equation for direct stress due to bending from [83], the expression (5.8) can be obtained to determine the required value of Φ in each boom such that it was fully stressed in bending.

$$\Phi_i = \frac{1}{\sigma_{allow}} \left| \frac{|M_z|(\hat{y}_i - \bar{y})}{\sum_{i=1}^6 \zeta_i (\hat{y}_i - \bar{y})^2} + \frac{|M_y|(\hat{z}_i - \bar{z})}{\sum_{i=1}^6 \zeta_i (\hat{z}_i - \bar{z})^2} \right| \quad (5.8)$$

Equation (5.8) was evaluated for each boom in the cross section. The maximum value of Φ represented the required rate of change of area with distance from the centre of area such that no boom yielded in bending. This maximum Φ value was used to calculate the area of every boom in the cross section using (5.6).

This method did not lead to a true fully stressed solution as the aft spar was oversized for conventional wings. This spar was located aft of the centre of area but close to the neutral axis, leading to a large value of ζ . However, in conventional wings, the bending moment about the \hat{z} axis is much greater than that about the \hat{y} axis. Though the aft spar had a high value of ζ , it was not subject to large bending stresses. However, subsequent analysis of box-wing structures showed that it would be inappropriate to bias the value of ζ towards \hat{y} displacements as the moments about both axes were of similar magnitudes in these designs.

The determination of the best Φ value was an iterative process the six Φ_i values were each a function of the centre of area location which was a function of the area distribution. Therefore, the calculation was iterated until the

relative error in the centre of area location was reduced to below the specified tolerance.

The axial force was assumed to be uniformly distributed along the cross section. Adding a constant area component to the moment of inertia, (5.3) complicated the calculation of Φ . Therefore, the allowable bending stress was decreased to account for the axial load being carried equally throughout all booms. This updated value for allowable stress was used in the subsequent iteration to determine Φ .

$$\sigma_{allow} = \sigma_y - \frac{F_x}{\sum_{i=1}^6 A_i} \quad (5.9)$$

Knowing the area distribution required to resist bending and normal stresses, the closed section shear could be calculated by initially assuming that the section was cut in the fore spar and the shear flow in that skin was zero. The shear flow in the next skin was determined by (5.10), taken from [83].

$$q_i = q_{i-1} - \frac{V_z}{I_{yy}} A_i (\hat{z}_i - \bar{z}) - \frac{V_y}{I_{zz}} A_i (\hat{y}_i - \bar{y}) \quad (5.10)$$

The shear flows calculated in (5.10) represent the mean value of the shear flow between the two booms acting in the positive sense in the direction from boom i to $i+1$. The closed-section shear flow for the section could be calculated using (5.11); derived from expressions given in [83].

$$q_o = - \frac{\sum_{i=1}^6 2 q_i dA_i}{2 \sum_{i=1}^6 dA_i} \quad (5.11)$$

where: dA_i is the area of the triangle formed by connecting boom i and $i+1$ to the centre of area, as shown in Figure 5.3.

Knowing the shear flow due to the shear forces, a constant shear flow was added to resist the shear caused by torsion. The thickness of each skin was determined by:

$$t_i = \frac{1}{\tau_{allow}} \left(q_i + q_o + \frac{T_x}{2 \sum_{i=1}^6 dA_i} \right) \quad (5.12)$$

The skin thickness was constrained by the minimum gauge thickness of the skin material. This was chosen as $\frac{1}{16}$ in based on manufacturing, durability

and lightning strike concerns. If the required skin thickness was less than the minimum gauge thickness, then the minimum gauge thickness was used instead.

Once the algorithm determined the fully stressed values for all seven structural thicknesses, *i.e.* the three boom areas and four skin thicknesses, the weight of the wing's primary structure was calculated by:

$$W = \sum_{n=1}^{n_{pan}} \left(\rho_n B_{n \rightarrow n+1} \left(\sum_{i=1}^6 A_i + \sum_{i=1}^6 t_i \ell_i \right) \right) \quad (5.13)$$

5.2.4 Allowable stresses

The model used an isotropic allowable stress criterion. Other authors have noted that the allowable stresses in tension and compression differ due to the constraints of metal fatigue and panel buckling, respectively [73]. This level of detail was not compatible with the fully stressed section method so an isotropic value of allowable normal stress was used, based on the maximum tensile yield stress. The finite element model could support different material definitions. Only 7075-T6 and 2024-T3 aluminium were considered, though any isotropic metal could be added to the materials database. The yield stress in shear was tabulated for each material rather than derived from the allowable normal stress. The allowable stresses were modified by a factor of safety of 1.5.

5.2.5 Secondary weights

Though the beam section model accounted for the material required to resist the primary forces resulting from the aerodynamic loading, it did not account for secondary weights. These were treated as two categories: the weight of the wing ribs, and the weight of leading and trailing edges and high lift devices along with the material required to resist their additional aerodynamic loads.

Both of these load groups could not be predicted using the physics-based equivalent beam model. Considering the ribs, the primary purpose of these components was to resist torsional loads on the wing as well as to stiffen the wing skin against buckling and transmit the loads from the high lift devices, propulsion systems and landing gear into the wing-box structure. Rather than attempt to model these effects directly, they were accounted for based on an empirical relationship given by Torenbeek [73]. This rib weight model is sensitive only to the wing area and aerofoil thickness, not on the load distribution. All wing designs considered in this study used conventional wing construction but had unconventional loading. As this rib weight correlation was not sensitive to the unconventional loading, its use could be extended to unconventional

wing designs. More details about this rib weight model and the assumptions made in its derivation are given in [73].

The weight of the leading and trailing edge high lift devices was also taken from the Torenbeek [73] wing weight model. The weight of each of the following components was modelled as being proportional to its planform area and an empirical constant:

- Fixed leading and trailing edges
- Leading edge slats
- Trailing edge flaps (Plain, single- and double-slotted)
- Ailerons
- Spoilers

These relations accounted for the increased aerodynamic loadings caused by these components and the material required to resist them. They also accounted for the increased self-weight of the wing. In the case of trailing edge flaps and ailerons, an additional factor was added to the secondary weight to account for the increased rib weight required to transfer these loads to the wing structure. Full details of how this method was derived and implemented are given in [73].

5.2.6 Numerical details

Because the analysis discretized the wing and solved the fully stressed problem in an iterative manner, there were several numerical details which affected the accuracy of the results. Cantilevered wings were discretized with a minimum of 15 elements along the semi-span. The aerodynamic model was more sensitive to the discretization than the structural model. Using fewer than 15 elements led to discontinuities in the aerodynamic forces between wing sections. For closed wings, the number of panels was increased so that approximately 15 panels were present between the fuselage centre line and maximum spanwise extent of the wing.

There were two iterative processes in the analysis: one to determine the fully stressed area distribution within each cross section, the other to determine the critical structural thickness distribution along the semi-span. Each of these analyses were iterated until the result converged to within a specified absolute and relative tolerance; these values are given in Table 5.1. The total number of iterations was limited to stop the calculation in the case of an infeasible wing design. The stringent tolerances were necessary to ensure that some of the thinner skins were fully stressed. In order to allow smooth convergence of both iterative processes, the change in structural thicknesses between iterations was limited by a numerical damping constant. The value

Table 5.1: Numerical parameters for the structural analysis

Parameter	Value
Absolute tolerance	1×10^{-8}
Relative tolerance	1×10^{-5}
Maximum iterations	100
Spanwise elements	15
Numerical damping	0.5

given in Table 5.1 was not appropriate for all cases. Planar wings with no crank could have a value of 1.0 while values as low as 0.4 were required for some nonplanar designs to converge.

5.3 Comparison of conventional aircraft weights

Since there are no box-wing transport aircraft in service, the wing weight model was validated against a family of legacy transport aircraft designed for short to medium range civil transport. These aircraft are listed in Table 5.2.

Some of the data required to model the weight of the wing were not available in open literature and had to be estimated. The retracted area of high-lift devices, spoilers and ailerons was measured from 3-view drawings. Each aircraft was analysed with only one load case, that of a 2.5 *g* pull-up manoeuvre at cruise flight conditions with a gust. In the absence of other information, the fore-spar and aft-spar locations for each aircraft were 15% and 70% of the chord, respectively. Unless other information was provided about the aerofoil section, each wing had a NACA230xx profile where ‘xx’ referred to the aerofoil’s thickness to chord ratio which could vary along the span for each aircraft.

Four alternative wing weight models were used to predict the weight of these aircraft’s wings to show how the accuracy of the present model compared to other commonly used models for conventional aircraft wing weight. The four models and the design variables to which they were sensitive are described below.

Ramyer Class II. Sensitive to MTOW, area, sweep, taper, thickness and control surfaces. [67]

Howe Basic Class II. Sensitive to MTOW, area, sweep, taper, thickness and cruise speed. [71]

Torenbeek Class II- $\frac{1}{2}$. Sensitive to entire wing design. [73]

Table 5.2: Reference aircraft data

Name	Number of Passengers	Wing Area [ft ²]	Wing weight [lb _f]	Entry to Service	Sources
Fokker F28-2000	79	822	7526	1972	[84, 85]
BAC-111	79	1014	9817	1965	[84, 86]
DC-9-10	90	934	9366	1965	[84, 86]
DC-9-40	115	1001	11891	1966	[84, 86]
MD-83	172	1270	15839	1986	[74, 87]
Boeing 727-100	131	1700	17682	1964	[84, 86]
Boeing 727-200	163	1700	18529	1967	[84, 86]

Howe Complex Class II- $\frac{1}{2}$. Sensitive to entire wing design. [71]

The results of the validation study are shown in Figure 5.5. For all the aircraft, the model described in this chapter predicted the weight of the wing to within $\pm 10\%$. This performance is as good as the best wing weight models. However, unlike the other models used in this study, the fully stressed algorithm was able to predict the aerodynamic loading and internal forces and moments of a closed wing structure. These results indicate that this model will be able to accurately predict the weight of a box-wing aircraft wing.

5.4 Details of box-wing internal structures

The wing weight model developed in this chapter was able to not only predict the total weight of the wing but provide information about the design of the internal structure. The internal structure of a wing design from the the parametric study of Chapter 4 with a high lift-to-drag ratio was examined in more detail. The design had a fore area ratio of 0.5, dimensionless stagger of 1.75 and height-to-span ratio of 0.25. The unique characteristics of a box-wing's internal structure were most pronounced in this design. The planform shape of the wing is shown in Figure 5.6a and the aerodynamic loading resulting from a $2.5g$ manoeuvre, scaled to account for a gust, is shown in Figure 5.6c.

The internal forces and moments resulting from this aerodynamic loading are shown in Figure 5.6d. There were several key differences between the trends seen in this figure and those for a conventional aircraft. The principal bending moment for a conventional wing is about the \hat{z} axis and decreases monotonically to zero along the span, (the definition of the element local coordinate system is shown in Figure 5.6a). In the box-wing there were sig-

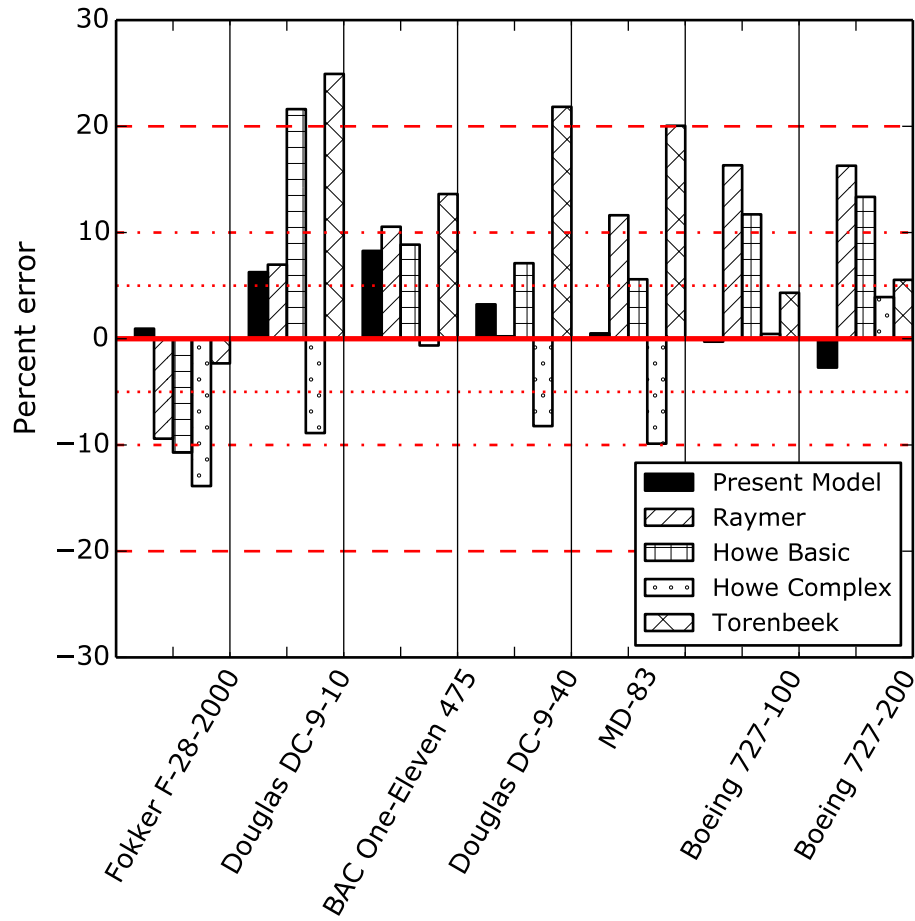
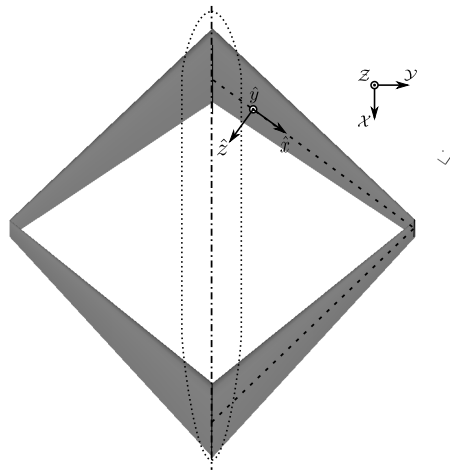
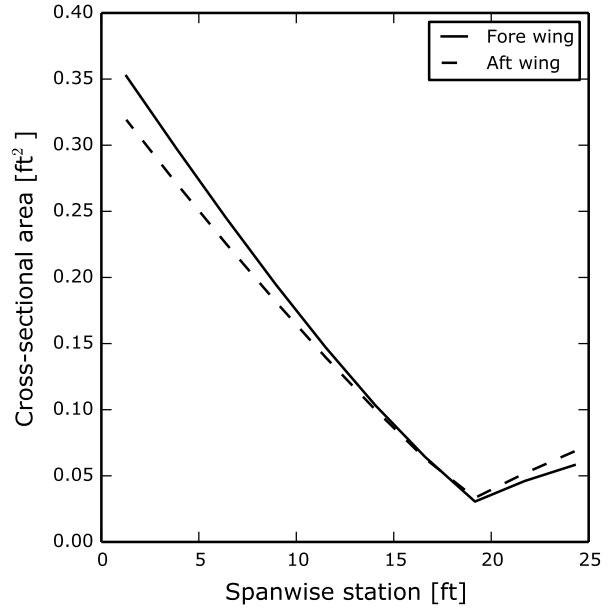


Figure 5.5: Summary of validation data. Percent error is the difference between the published weight of the wing and the weight predicted by each model.

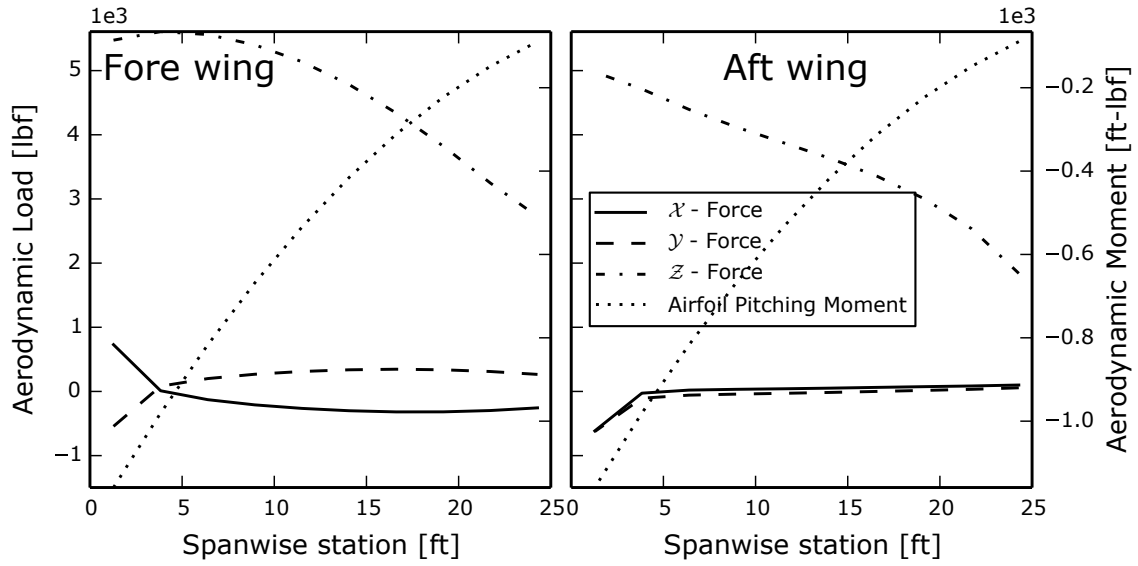
nificant moments about both the \hat{z} and \hat{y} axes showing the need for a finite element structural model to predict the internal loading as well as a detailed cross-sectional model able to distribute area between the three variable booms to resist significant moments about both principal axes of the cross section. Another unusual trend in the box-wing design was that the bending moment about the \hat{z} axis did not decrease monotonically to zero but rather reached zero at roughly $\frac{2}{3}$ of the span along both the fore and aft wings and then began to increase in magnitude but in the opposite sense as at the wing root. This behaviour was the result of the statically indeterminate box-wing structure and could not be predicted with conventional wing weight models. The sign reversal of the principal bending moment has also been observed in other box-wing structural studies [9, 8, 51]. The spanwise factor of safety for each cross-sectional element is shown in Figure 5.6e. As a consequence of the unusual distribution of internal moments, the critical boom in the wing changed along the span as the axis of the largest bending moment changed. This demonstrated why seven independent cross section variables were needed to determine the mass of material required to resist the applied loads. Most of the skin segments were under-stressed as this regional-jet design was limited by the minimum gauge thickness constraints, as in previous structural studies of joined-wings [44].



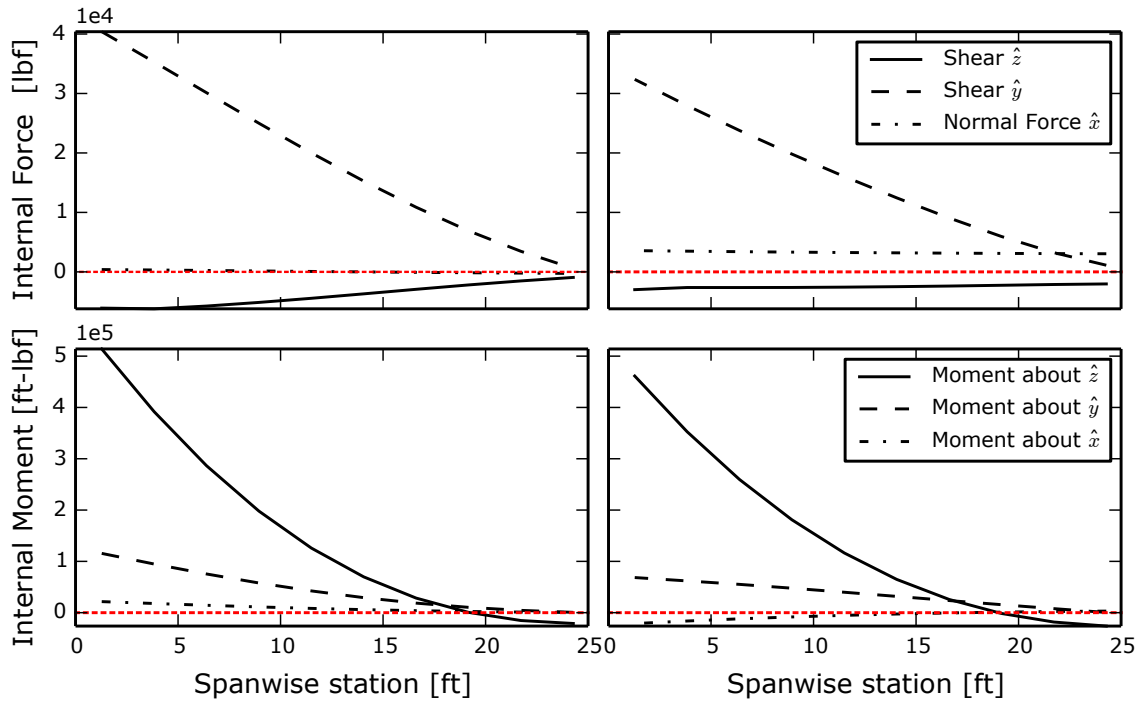
(a) Box-wing planform



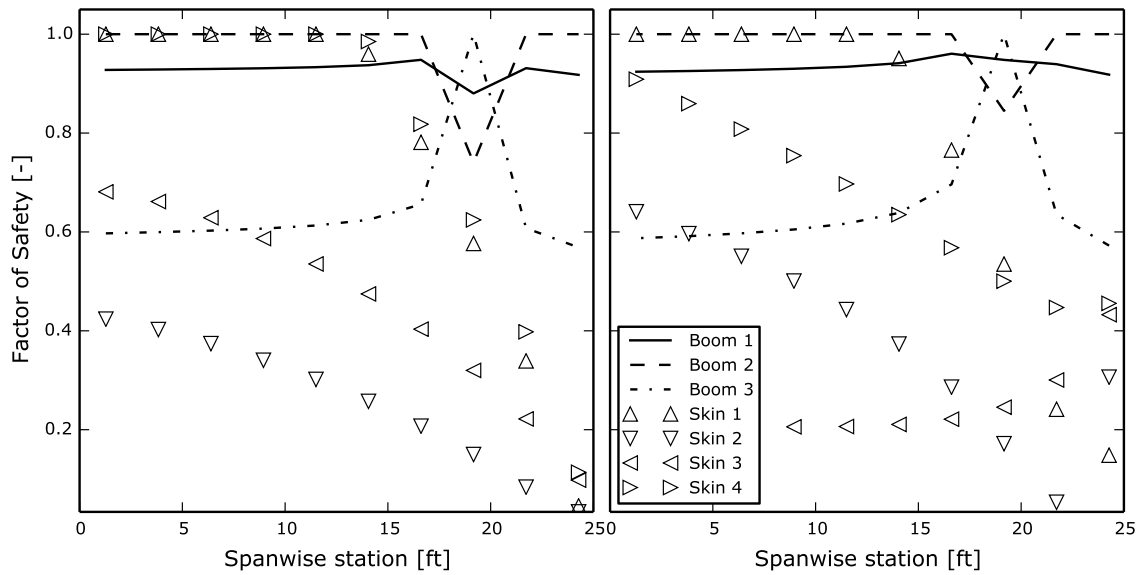
(b) Spanwise Area Distribution



(c) Aerodynamic forces



(d) Internal forces and moments



(e) Factor of safety

Figure 5.6: Details of box-wing structure for height-to-span ratio 0.25

5.5 Other structural concerns

5.5.1 Aeroelasticity

The wing weight model did not consider the weight of material required to prevent aeroelastic instabilities in the structure. Previous authors [8, 35] have investigated this effect for box-wing aircraft and were able to suppress such instabilities with an increase of only 2% in the wing weight.

5.5.2 Panel buckling

The structural model did not consider the added weight of the stiffeners required to resist the buckling of the wing skin panels. Previous work has noted that panel buckling constraints strongly influence the design of regional-jet aircraft [88]. As was shown in Figure 5.6e, the minimum gauge thickness constraint dominated the skin thickness distribution for the box-wing. However, previous studies of box-wing structures have examined the effects that buckling has on the weight of the wing and found that the effect was on the order of 8% [8]. Therefore, a 10% penalty was added to the results of the fully stressed analysis to represent the added weight required to resist buckling and aeroelastic concerns.

5.6 Comparison of box-wings to conventional

The optimized wing designs obtained from the parametric study presented in Chapter 4 were used to investigate what structural advantages, if any, box-wing designs had compared to a cantilevered wing. The wing weight model presented in this chapter was used to estimate the weight of the reference wing as well as three different box-wing designs. These designs were chosen from the family of equal area wings with a stagger of $2x_{1 \rightarrow 2}/b = 1.75$. Three different height-to-span ratios were chosen: $h/b = 0.5$, which corresponded to the best aerodynamic performance; $h/b = 0.25$, which corresponded to equal aerodynamic performance of the box-wing and reference wing; and $h/b = 0.375$, the midpoint between both extremes.

The results of this study are shown in Table 5.3. The box-wing with the smallest height-to-span ratio had a heavier main wing structure than the reference aircraft, but when the weight of the horizontal stabilizer was added to the reference wing, both wing systems had essentially the same weight. This confirms the findings of previous studies on joined- and box-wing structures [9, 44, 8]. As the height-to-span ratio of the box-wing increased, the weight of the box-wing structure exceeded that of the reference wing plus horizontal

Table 5.3: Comparison of wing weight between a cantilevered wing and various box-wing designs

Aircraft	reference		box-wing	
Height-to-span	n/a	0.25	0.375	0.5
Main wing [lb _f]	4156	4603	4733	4909
Horizontal stabiliser [lb _f]	430.6	0.0	0.0	0.0
Total wing weight [lb _f]	4587	4603	4733	4909
Difference rel. to ref.	n/a	+0.358%	+3.19%	+7.02%
Difference rel. to MTOW	n/a	+0.035%	+0.311%	+0.685%
L/D	22.14	22.36	23.16	23.64
L/D rel. to ref	n/a	+1.0%	+4.6%	+6.7%

tail. However, the fuel burn of an aircraft, estimated by equation (1.1), is dependent on the weight at the start of cruise and the lift-to-drag ratio. For the heaviest box-wing design the takeoff weight increased by 0.7%, while the lift-to-drag ratio increased by 7%. If the goal of the design was to achieve minimum fuel burn, maximizing the height-to-span ratio was still preferable for the overall design though it is inferior to the reference aircraft with respect to structural weight.

These results show that the disciplines of aerodynamic performance and wing structures were in conflict. This study only examined one parameter of the wing design, the height-to-span ratio. The true optimal wing design with respect to fuel burn would require a multi-disciplinary study which considers the interactions between these two disciplines. Such a study will be presented in subsequent chapters.

6 Multidisciplinary Aircraft Design Problem

Previous chapters have considered the effects of changes to a box-wing's geometry on stability (Chapter 3), aerodynamics (Chapter 4), and structures (Chapter 5). These single-discipline studies found that trends which maximised performance with respect to each discipline had the effect of decreasing the performance metric of at least one other discipline. The best design of a box-wing aircraft could not be determined through single discipline studies but rather required the couplings between these disciplines to be resolved. In addition, there were several disciplines critical to the design of a transport aircraft which were not considered in the previous single-discipline studies. This chapter presents a design procedure for a transport aircraft which considers five further disciplinary interactions: propulsion system integration, landing gear integration, mission fuel burn calculation, takeoff performance and derivation of the aircraft centre of gravity and moment of inertia from individual component geometries. This design procedure was coupled with an optimization routine to determine the best design of a box-wing aircraft for a regional jet mission.

To make a fair comparison of the box-wing to conventional aircraft, the same design procedure and optimization was performed on baseline aircraft whose geometry and mission matched in-service regional-jet aircraft. By comparing optimized box-wings to optimized baseline designs, the desirable and deleterious aspects of the box-wing configuration could be attributed to underlying properties of a box-wing rather than non-optimal design choices for either the baseline or box-wing configuration.

The goal of the analysis was to determine if box-wing aircraft had an advantage over conventional wing designs with respect to their impact on the environment. The fuel burnt during the main mission was used as a metric for environmental impact as it was proportional to the volume of products of combustion released into the air. It was chosen as the objective for both

the baseline and box-wing optimization problem. Two other objectives were considered: minimizing the total fuel weight, including reserves; and minimizing the maximum takeoff weight for a given payload. Considering the former objective, from an environmental perspective it would not be preferable if an aircraft traded greater fuel consumption during cruise for savings in the reserve mission, even if the total fuel mass were reduced. Likewise, considering the second objective, if significant savings in structural weight came at a penalty to fuel burn, the design would not be preferable from an environmental standpoint even if the maximum takeoff weight were reduced.

This choice of objective led to the optimization problem formulation:

$$\begin{aligned} & \min. W_{fuel} \\ & \text{such that } \begin{cases} h_i = 0 & i \in 1 \dots n_{eq} \\ g_j < 0 & j \in 1 \dots n_{ineq} \end{cases} \\ & \text{with respect to } \{X_i \quad i \in 1 \dots n_{com}\} \end{aligned} \quad (6.1)$$

where: h_j were the n_{eq} equality constraints placed on the design, g_j were the n_{ineq} inequality constraints placed on the design and X_i were the n_{com} disciplinary analysis variables. There were four groups of disciplinary analysis variables: planform geometry variables, effector geometry variables, landing gear geometry variables, and aircraft performance variables. There were six groups of constraints placed on the design: aircraft geometry constraints, landing gear constraints, cruise stability constraints, cruise trim constraints, takeoff constraints and aircraft performance constraints. The definition of these variables and constraint groups are discussed further in Sections 6.3.1 and 6.3.2, respectively.

In order to determine the values of the objective and constraints arising from a given set of variables, the various disciplinary models used in this analysis were combined into a multidisciplinary design analysis procedure. This procedure accounted for the interactions between the disciplinary analyses while reducing the number of interdisciplinary couplings. The structure of this design procedure is discussed further in Section 6.1. Details of the various disciplinary analyses are provided in Section 6.2. More details of variables, constraints and algorithms used in the optimization problem are given in Section 6.3.

6.1 Multidisciplinary analysis procedure

The structure of the aircraft design analysis procedure is shown in Figure 6.1. To reduce the number of times each discipline was called during the analysis

procedure, the analyses were ordered so as to reduce the off-diagonal coupling feedbacks between disciplines. Only two off-diagonal couplings remained, the Maximum Takeoff Weight (MTOW) and the cruise distance. These two couplings were resolved using an interdisciplinary feasible multidisciplinary optimization approach [89]. A new set of interdisciplinary coupling variables and constraints were added to the problem formulation given in (6.1). The resulting optimization problem is given by (6.2). This was the optimization problem formulation used for both the box-wing and baseline analysis.

$$\begin{aligned}
 & \min. W_{fuel} \\
 & \text{such that } \begin{cases} h_i & = 0 & i \in 1 \dots n_{eq} \\ g_j & < 0 & j \in 1 \dots n_{ineq} \\ Y_k - \hat{Y}_k & = 0 & k \in 1 \dots n_{coup} \end{cases} \quad (6.2) \\
 & \text{with respect to } \begin{cases} X_i & i \in 1 \dots n_{com} \\ Y_k & k \in 1 \dots n_{coup} \end{cases}
 \end{aligned}$$

where: Y_k were the n_{coup} interdisciplinary coupling variables calculated during the analysis and \hat{Y}_k were the best estimates of these values, provided each time the analysis procedure was called.

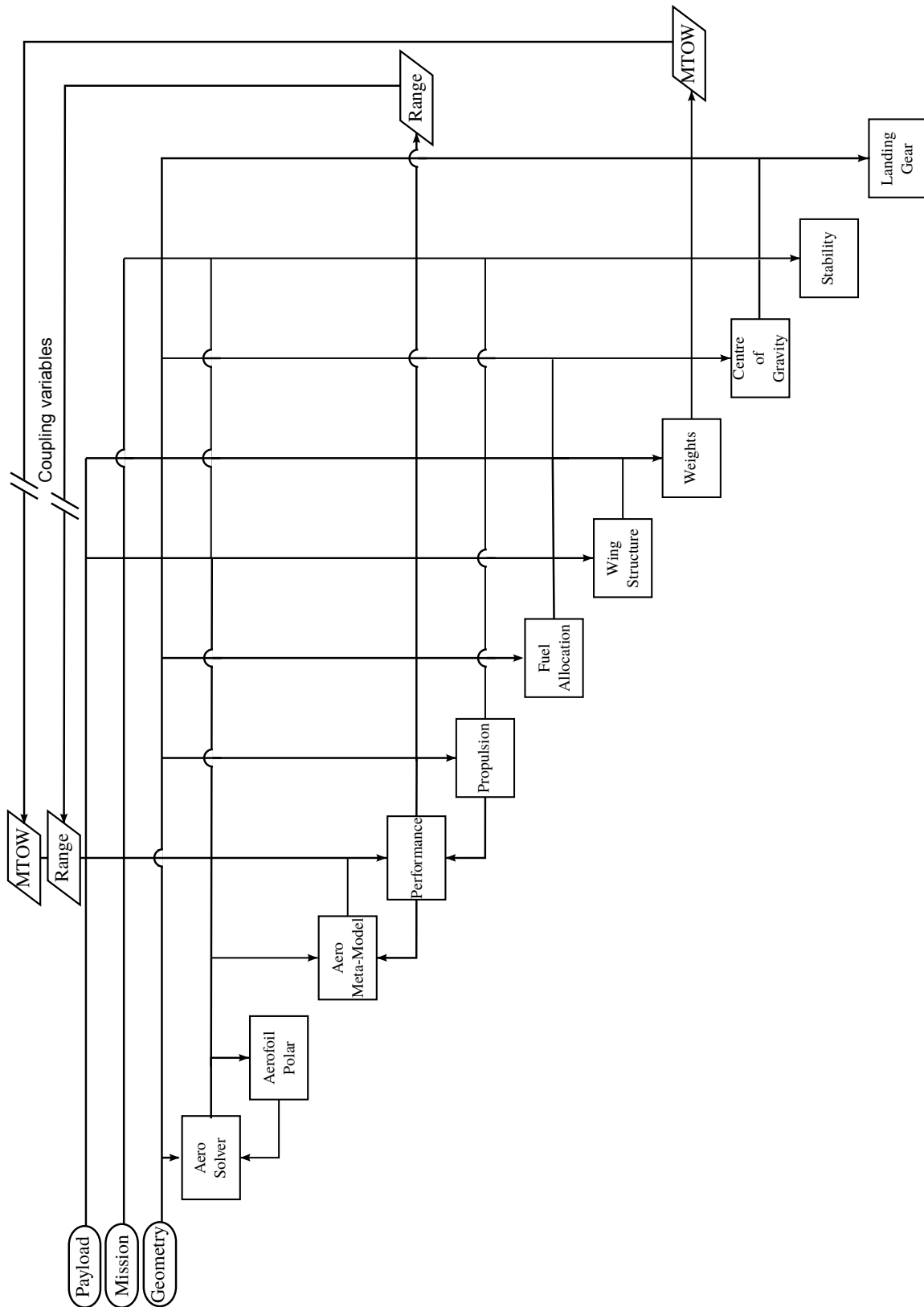


Figure 6.1: Aircraft design analysis procedure for conventional and box-wing aircraft

6.2 Disciplinary models

6.2.1 Geometry

The geometry of the wing was generated in the same manner as in the parametric study in Chapter 4. However, the sweep of the fore and aft wings as well as the vertical segment were each variables rather than dependant on a specified stagger as in Chapter 4. The box-wing aircraft used a NACA 63-312 aerofoil profile for the entire wing. The baseline aircraft, shown in Figure 6.3, used NACA 22013 aerofoil profile at the wing root, tapering to a NACA 63-310 profile at the tip of the main wing. The winglets of the baseline aircraft tapered to a NACA 0005 section. The box-wing geometry used a constant thickness-to-chord ratio along the span to limit the degrees of freedom of the optimization problem. The theoretical box-wing loading shown in Figure 2.3 as well as the optimal loading computed in Chapter 4 showed that box-wings carry more lift near the tip of the wing than a conventional design. This higher loading at the wing tips meant that reducing the thickness-to-chord ratio along the span may not be as advantageous for box-wing aircraft as for conventional designs. Though the thickness-to-chord ratio of the box-wing remained constant, the wing thickness did taper along the span due to the reduction of the local chord length.

In order to model takeoff performance, flaps and elevators were located on the trailing edge of the box-wing aircraft. Slats could be also installed along the leading edge of box-wing to allow a fair comparison to baseline aircraft. Flaps were installed between an inboard spanwise station and extended out to 85% of the span to allow space for ailerons at the wing tips. Flaps and elevators were co-located on the box-wing designs. For this reason, flaps on the box-wing aircraft were modelled as plain flaps rather than as single slotted flaps, used on the baseline aircraft. A representative box-wing aircraft with flaps, elevators and slats installed is shown in Figure 6.2. The size and positions of the high lift devices on the baseline aircraft were measured from three-view drawings [64].

The landing gear was assumed to be connected to the fuselage of the box-wing aircraft. The landing gear's location was parametrized with four variables: the axial station of the nose and main gear; the length of the main gear strut; shown in Figure 6.4; and the offset outboard of the fuselage, shown in Figure 6.2. Details of how the tires were sized and the geometric constraints on the landing gear are given in Section 6.2.14.

The dimensions of the box-wing's fuselage and vertical tail were specified to be the same as the comparable baseline aircraft. These data were obtained from measurements of the baseline aircraft geometries [64].

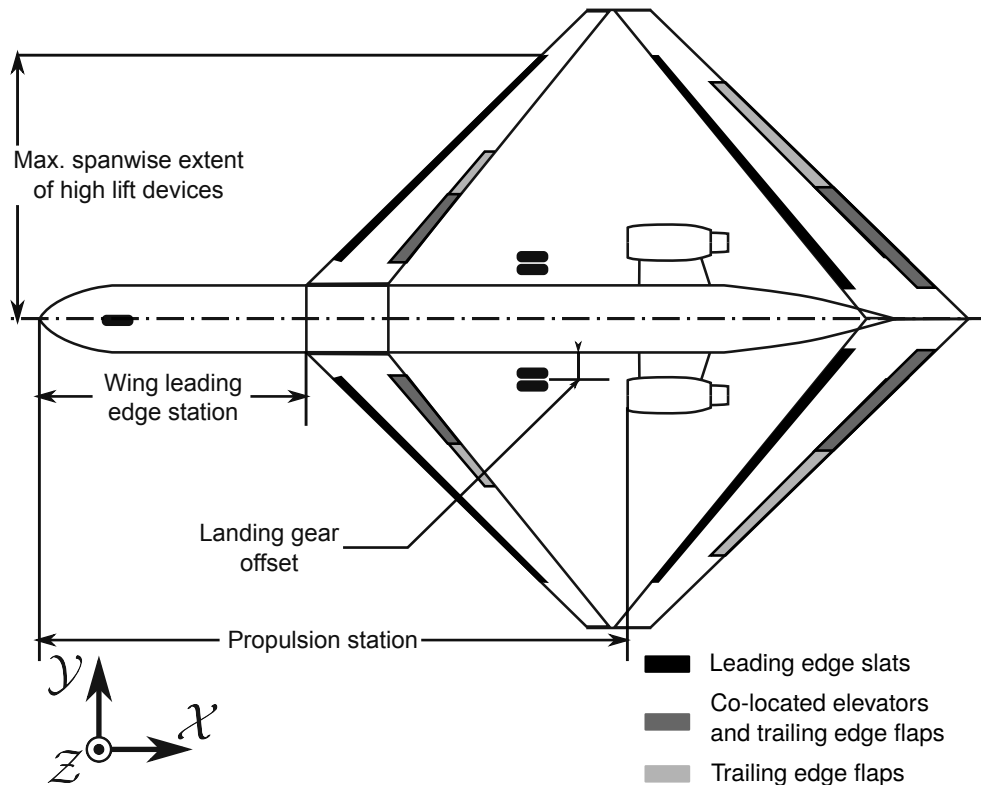


Figure 6.2: Planform geometry of the box-wing aircraft showing the location of high lift devices. In this generic design, the flap and elevator area has been biased towards the aft wing.

6.2.2 Payload

The payload consisted of both passengers and baggage. For simplicity, the payload was modelled as two lumped masses. Each passenger and their carry-on baggage were assumed to weight 185 lb_f , the centre of gravity of the passenger compartment was located at the midpoint of the first and last row of passenger seats. The weight of the baggage was estimated as 35 lb_f per passenger and the lumped mass of the baggage was located at the aft cargo door. Figure 6.4 shows the location of these two payload components. Guidance on the weights of passengers and baggage were given by [90, 67]. The payload weights and centre of gravity locations were shared between box-wing and baseline aircraft with the same mission specification.

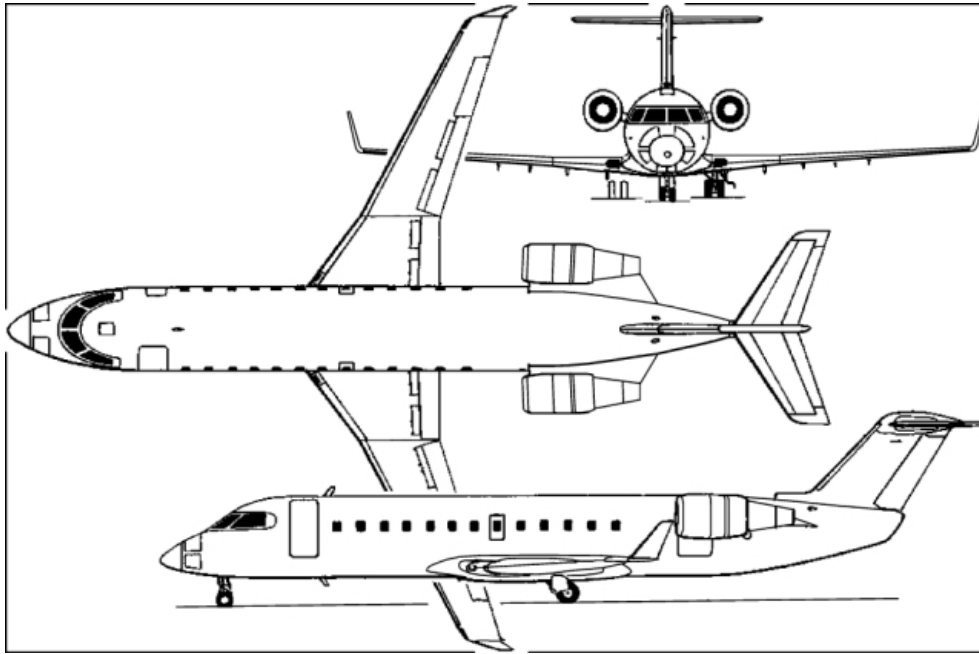


Figure 6.3: Three-view drawings of the Bombardier CRJ-200 aircraft, one of the baseline aircraft [64].

6.2.3 Mission

The aircraft were designed to perform a typical regional jet transport mission, shown in Figure 6.5. There were three segments to the climb profile. First, the aircraft accelerated at constant altitude from the limit of 150 knots Calibrated Air Speed (CAS) to 250 knots CAS at 10000 ft. Then, the aircraft climbed at constant CAS until the local Mach number matched the cruise Mach number. Past this point, the aircraft climbed at constant local Mach number until it reached the cruise altitude. The mission specified a cruise speed and altitude which represented the conditions at the start of the cruise phase. Descent followed the climb profile but in reverse, starting from the initial cruise altitude.

The fuel reserves required by 14CFR§121.639 only specify the loiter time [91] and not the diversion distance. The aircraft must have sufficient reserves to divert to an alternate airport and then loiter for the specified 45 min. The 100 nmi diversion distance was chosen as a reasonable mean distance to an alternate airport during a regional jet mission.

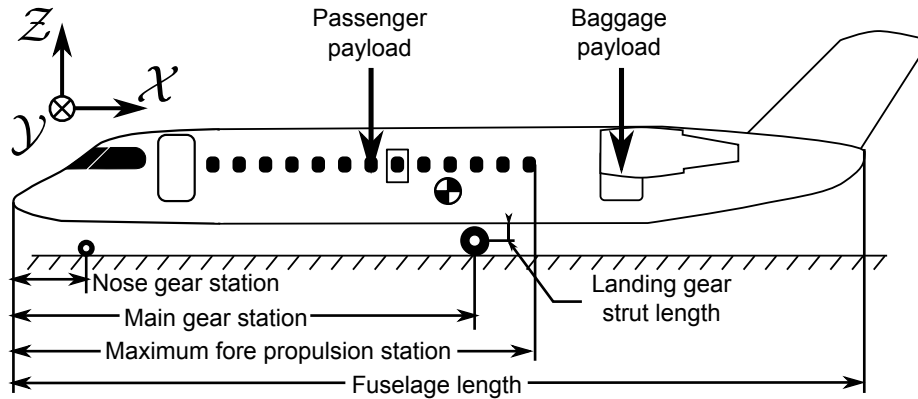


Figure 6.4: Payload location for the baseline and box-wing aircraft.

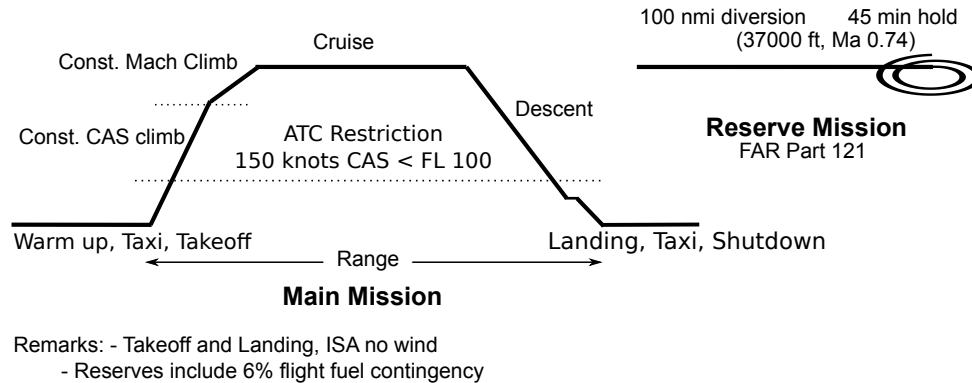


Figure 6.5: Regional jet mission specification.

6.2.4 Aerodynamic model

The aerodynamic model used to assess the cruise aerodynamic behaviour and stability derivatives of the box-wing and baseline aircraft was the `pyVORLIN` vortex panel aerodynamic solver [49, 82]. This algorithm determined the spanwise distribution of circulation on the wing assuming steady inviscid flow. From this circulation distribution, the lift, pitching moment, and induced drag of the wing could be estimated. The wing was modelled as a spanwise array of vortex rings, conforming to the wing's planform. To model the wake of the wing, each of these vortex rings were connected to a second vortex ring, meeting the Helmholtz condition [92]. The aerodynamic influence of each wing and wake vortex ring on the other formed an $n \times n$ \mathbf{A} matrix. The vector of n circulation strengths, $\mathbf{\Gamma}$, was related to the n component boundary condi-

tion vector, \mathbf{B} , by (6.3). The boundary condition vector was the component of incoming flow acting normal to each wing and wake vortex ring. Further details of how the \mathbf{A} and \mathbf{B} matrices were constructed are given in Chapter 12 of [92].

$$[\mathbf{A}] \{\Gamma\} = \{\mathbf{B}\} \quad (6.3)$$

Examples of the discretization of a baseline and box-wing aircraft are shown in Figure 6.6. The aerodynamic solver modelled the wing using a single chordwise panel and therefore needed aerofoil section data to determine the effect of the wing’s camber on the lift distribution. The circulation distribution given by (6.3) only predicted the induced drag of the wing. The parasitic drag was determined by evaluating the pressure and skin friction drag for each vortex panel on the wing using local aerofoil section data. These data were either provided as constants for each aerofoil profile or as a Reynolds number dependent polar, described in Section 6.2.5. Wave drag at transonic speeds was predicted using the Korn equation [13]. This equation predicted the wave drag on each vortex panel based on how close the free-stream Mach number was to the local drag divergence Mach number. The local drag divergence Mach number was itself a function of the local semi-chord sweep, the local thickness-to-chord ratio and an empirical technology factor, assumed as 0.87 to be representative of conventional aerofoils [13]. The aerodynamic model only predicted the drag from the lift generating surfaces of the aircraft. The drag resulting from the fuselage, nacelles, pylons and vertical tail were estimated using analytic methods presented in Chapter 3 of [70].

The aerodynamic model determined the aerodynamic forces and moments on the aircraft’s lifting surfaces as a function of angle of attack. A line search was used to determine the forces and moments corresponding to a specified lift coefficient. Sensitivities of the aerodynamic forces and moments were calculated using a finite difference method. The maximum lift coefficient of the aircraft was determined using a line search for the point where the local lift curve slope was 25% of its value at zero angle of attack. The ability of pyVORLIN to predict the lift, drag and moment of a variety of aircraft designs is shown in Annex A.

Aerodynamic forces in takeoff configuration were also predicted by pyVORLIN. The effect of high lift devices such as flaps and slats were accounted for by modifying aerofoil section data for C_{l_o} , C_{m_o} , C_{d_o} and $C_{l_{max}}$ based on empirical relations sensitive to effector size and deflection, as given by [60]. Similarly, the effects of elevator deflection were accounted for by modifying these aerofoil section properties based on the empirical relations given by [93]. The ground effect was modelled by reflecting an image of the wing and wake vortex rings

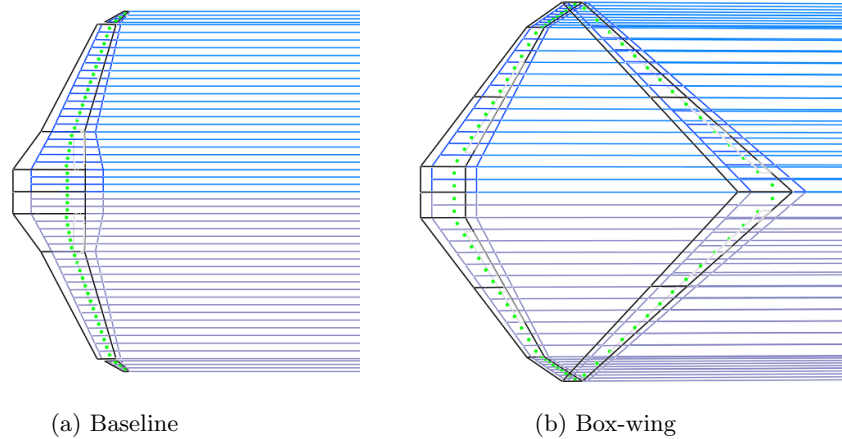


Figure 6.6: Examples of pyVORLIN discretization.

across the ground plane. Annex A gives validation examples of aircraft with high lift devices and in ground effect.

6.2.5 Aerofoil performance model

The section properties of different aerofoil designs were predicted using the V GK aerofoil solver [66]. This solver determined the inviscid flow over the aerofoil by solving the full potential equations for the steady compressible flow of a gas using a regular grid, conformally mapped from the aerofoil profile to a circle. The inviscid solver has been validated for transonic flows where the local Mach number upstream of any normal shock wave was less than 1.3 [66]. The effect of the boundary layer was modelled by the forward propagation of the boundary layer governing equations from the leading edge stagnation point. The solver did not model transition but rather assumed it at fixed chordwise positions on the aerofoil. The solver calculated lift, drag and pitching moment of the aerofoil for a range of angles of attack. These data were reduced to a set of coefficients which represented the aerofoil's behaviour in the attached flow regime. The aerofoil pitching moment, measured at the quarter chord point, was assumed constant. The lift at zero angle of attack, C_{l_0} , and lift curve slope C_{l_α} defined the section lift coefficient at any attached angle of attack. The maximum section lift coefficient was predicted using V GK's internal algorithms [94]. The skin friction and pressure drag of the aerofoil section was

modelled as a quadratic function of the section lift.

$$C_d = C_{d_{p_0}} + C_{d_{p_1}} C_l + C_{d_{p_2}} C_l^2 \quad (6.4)$$

These parameters could be used in the `pyVORLIN` aerodynamic solver either as constants at a given Reynolds number, as in Chapters 4 and 5, or as a Reynolds number dependent polar, as in the analysis presented in this Chapter. In the latter case, data for each aerofoil section were determined for six Reynolds numbers between 1×10^6 and 5×10^7 . The local Reynolds number for the aerofoil was calculated based on the local chord length and airspeed. The data were linearly interpolated to determine the coefficient at the given Reynolds number.

6.2.6 Aerodynamic meta-model

Though the vortex panel aerodynamic model was able to solve for the lift, drag and pitching moment of the aircraft on the order of one second, the performance algorithm, as discussed in Section 6.2.7, required aerodynamic forces to be evaluated on the order of one hundred times. Further calls were required to the aerodynamic model to match the angle of attack which produced the lift at each point in the performance analysis. To reduce the execution time of the performance model, tables of lift and drag data were calculated for the aircraft in takeoff and cruise configurations to allow the performance module to predict the aerodynamic forces on the aircraft quickly and accurately.

Over a range of Mach and altitude combinations, the aerodynamic model discussed in Section 6.2.4, `pyVORLIN`, was evaluated at two points, low and high angle of attack. From these two points, the four independent parameters in (6.5) and (6.6) could be evaluated for a given Mach number and altitude.

$$C_L = C_{L_o}(Alt., Ma) + C_{L_\alpha}(Alt., Ma)\alpha \quad (6.5)$$

$$C_D = C_{D_{p_0}}(Alt., Ma) + K(Alt., Ma)C_L^2 \quad (6.6)$$

To solve for the lift and drag at an arbitrary point, these coefficients were linearly interpolated to the target Mach number and altitude using a multidimensional interpolation algorithm [95]. From (6.5) and (6.6), the lift and drag could be estimated for either a given incidence or lift coefficient. The maximum aircraft lift coefficient was calculated once for each flight configuration.

Tests showed that when the aerodynamic meta model, rather than `pyVORLIN`, was used to predict aerodynamic forces across the mission, the computation time was reduced from 62.1 s to 2.2 s and the results differed by only 0.1%

from those obtained from the vortex panel solution. Similar accuracy and increase in speed were observed for box-wing designs.

6.2.7 Performance

The fuel burnt and distance travelled for each segment of the mission, shown in Figure 6.5, were evaluated in the performance module to estimate the weight of fuel required to perform both the main and reserve missions. The warm-up, taxi, landing and cool-down segments were estimated using fixed fuel fractions given by [90]. The method of Powers [96] was used to estimate the takeoff balanced field length. Climb and descent segments were modelled by numerically integrating the aircraft equations of motion at constant steps of 1500 ft as the aircraft followed the altitude and speed schedules specified by the mission. The descent rate was also limited by the maximum allowable rate of cabin de-pressurisation. The climb and descent phases used the aerodynamic meta-model described in Section 6.2.6 while the cruise and loiter phases used the full vortex panel aerodynamic model discussed in Section 6.2.4. Cruise and loiter fuel consumption were calculated using (1.1) and (6.7) [67], respectively.

$$W_{fuel} = W_s \left(1 - \exp \left(\frac{-E \cdot SFC_T}{L/D} \right) \right) \quad (6.7)$$

6.2.8 Propulsion

The performance of the turbofan engines used on the baseline and box-wing aircraft were modelled using the empirical relations of Bartel and Young [97]. This model predicted the thrust and specific fuel consumption of a turbofan engine at a given altitude, speed and throttle setting. The bypass ratio of the engine was fixed in the analysis but the sea level maximum thrust was a variable.

A map of engine performance, generated by this model over a range of Mach numbers and altitudes, is shown in Figure 6.7 for an engine with sea level thrust and bypass ratio set to match the CF34-3B1 engine used on the CRJ-200. The thrust was sensitive to both speed and altitude. The available thrust decreased with increasing altitude and speed, up to the cruise Mach number of approximately 0.7.

6.2.9 Fuel allocation

The available fuel volume in the wings was derived from the wing's internal structure and surface coordinates. Tanks were located between the fore and

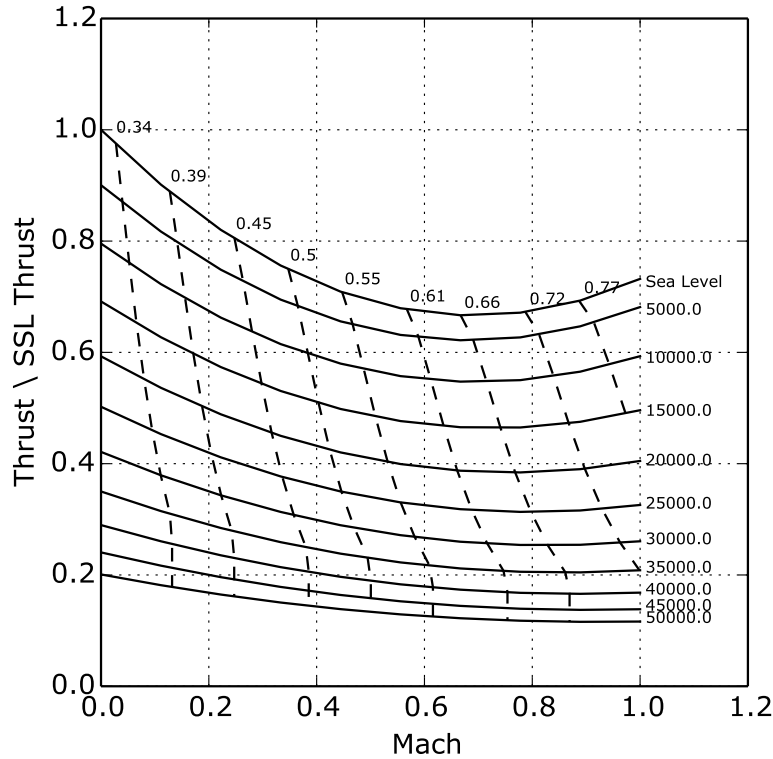


Figure 6.7: Performance map of a turbofan engine with the same thrust and bypass ratio as the CF34-3B1. Solid horizontal lines are the trend in thrust with Mach number and altitude at full throttle. Dashed vertical lines represent constant values of specific fuel consumption in $\frac{\text{lb}_f}{\text{lb}_f \text{ hr}}$.

aft spars, as specified by the structural model, and extended outward to 85% of the wing span to allow for vent boxes at the wing-tips. The cross sectional shape of the tanks was an aerofoil-conforming hexagon, to represent the volume available between the wing's two main spars. A representative box-wing aircraft with fuel tanks located in the fore and aft wings is shown in Figure 6.8.

The fuel tanks were filled in a fixed order. First the centre tank formed by the constant chord section of the wing passing through the fuselage was filled, followed by the wing tank(s). For box-wing aircraft, if there was empty volume in the wing tanks, the empty volume could be shifted fore or aft to allow for some control over the centre of gravity. The centre of gravity for each tank was specified at the tank's centroid, whose location was independent of

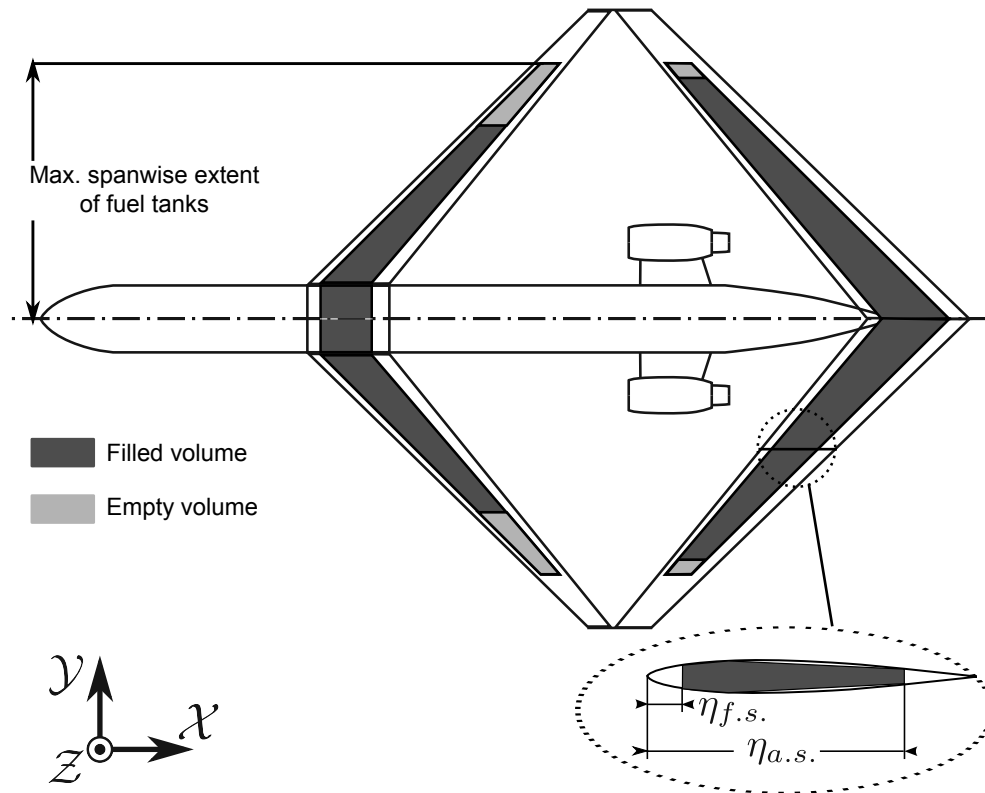


Figure 6.8: Example of fuel tanks placed in the fore and aft wings of a box-wing aircraft. There is empty volume in the wing tanks and the empty volume has been biased towards the fore wing.

the fuel volume. For the baseline aircraft, fuel tanks were located and filled in a similar manner. As there was only one pair of wing tanks, there was no allocation of empty volume between the tanks.

6.2.10 Wing structure

The weight of the main wing structure for both baseline and box-wing aircraft was estimated using the model presented in Chapter 5. The critical design condition was a $2.5g$ manoeuvre plus a gust at the start of cruise.

6.2.11 Weights

The weight of all aircraft components other than the main wing were estimated using empirical predictions based on the aircraft's total weight and geometry.

Table 6.1: Weight categories

Component	Weight model source	Centre of gravity rule [98]
Wing	Chapter 5	0.3 to 0.7 of wing MAC
Horizontal tail	VDEP [99]	
Vertical tail	VDEP [99]	
Fuselage	VDEP [99]	0.4 to 0.6 of fuselage length
Nacelle	FLOPS [100]	0.45 to 0.60 of nacelle length
Pylon	NACA CR 151970 [84]	0.45 to 0.60 of pylon MAC
Landing Gear	Raymer [67]	weighted average of nose and main gear locations
Anti Ice	FLOPS [100]	0.15 to 0.45 of wing MAC
APU	NASA CR 15970 [84]	0.75 to 0.98 of fuselage
Hydraulics	NASA CR 15970 [84]	Area weighted average of effector centroid
Flight Control	NASA CR 15970 [84]	Area weighted average of effector centroid
Electrical	NASA CR 15970 [84]	0.4 to 0.70 of wing MAC
Air conditioning	NASA CR 15970 [84]	0.45 to 0.85 of wing MAC
Furnishing	NASA CR 15970 [84]	0.35 to 0.54 of wing MAC
Avionics	Perez [101]	0.09 to 0.11 of fuselage length
Engines	Perez [101]	0.45 to 0.6 of engine length

The different component and system weight groups are shown in Table 6.1 as well as the source of the equations used to estimate the weight and predict a range of axial centre of gravity locations. This model was used to predict the weight of several in-service transport aircraft and, for regional jet aircraft, was able to predict the operational empty weight to within $\pm 20\%$. More details are contained in Annex A.

6.2.12 Centre of gravity and inertia

The centre of gravity was calculated as the weighted average of the component weights estimated using the model of Section 6.2.11. The centre of gravity was evaluated with both full and empty fuel tanks to ensure that all constraints based on the centre of gravity were met at both the start and end of the mission. The centre of gravity model provided a point location for the vertical and spanwise location of the centre of gravity and a range for the streamwise centre of gravity location. This range arose from the spread of possible centre of gravity locations for various systems and was based on guidelines given

in [98]. Though it would be ideal to design the aircraft to meet all constraints at the extreme fore and aft limits of the expected centre of gravity location, this range was so broad that feasible designs could not be located. Therefore, fore and aft limits within this axial range were included as design variables. It was assumed that in the detailed design of the aircraft, the centre of gravity of each component could be tuned to place the centre of gravity of the aircraft anywhere within the expected centre of gravity range.

The moment of inertia of the aircraft was calculated based on each component as a lumped mass located at the component's centre of gravity. As an initial approximation, the moment of inertia of each component about its own centre of gravity was not considered.

6.2.13 Stability

As in the parametric study presented in Chapter 4, the static stability and trim of the aircraft were assessed using the `pyVORLIN` vortex panel aerodynamic model in order to constrain the design. However, in the aircraft design procedure discussed in this chapter, a wider range of centre of gravity conditions and aircraft configurations were considered. The longitudinal stability at cruise was estimated with both full and empty fuel tanks at the specified fore and aft limits of the centre of gravity. As the aircraft could not be trimmed at all these points with a given twist distribution, the aircraft was constrained to be trimmed with zero elevator deflection with full fuel tanks at the forward centre of gravity limit. The trim constraint was evaluated at the forward centre of gravity limit, as the aft limit was already constrained by the static margin requirements. For all other points, the zero lift pitching moment was constrained to be positive so that the aircraft could be trimmed at some positive angle of attack.

Stability and control was also assessed during the takeoff run, specifically the ability of the aircraft to rotate on takeoff. The rotation speed was chosen as 1.2 times the stall speed. The forces and moments acting on the aircraft during takeoff rotation are shown in Figure 6.9 and their magnitudes were estimated using (6.8), given in [102]. The meaning of each of these forces is described in more detail below.

$$M_{ell_{mg}} > I_{yy_{mg}} \ddot{\Theta} - \left(\frac{W}{g} \right) \dot{u}(z_{c.g.} - z_{mg}) + T(z_t - z_{mg}) + W(x_{mg} - x_{c.g.}) - M_{a.c.mg} \quad (6.8)$$

Rotational inertia ($I_{yy_{mg}} \ddot{\Theta}$) The aircraft had to pitch up at a specified angular acceleration of 8 deg/sec². The inertia of the aircraft resisted this rotation and created an apparent moment resisting takeoff rotation.

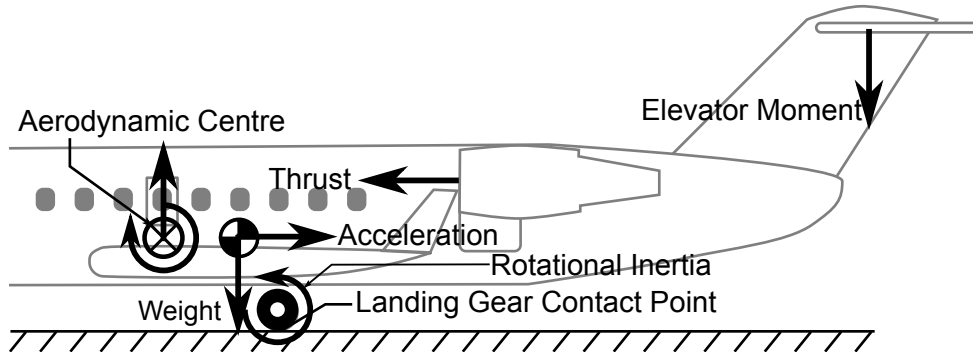


Figure 6.9: Forces acting on baseline aircraft during takeoff rotation. Arrows show forces acting in the positive sense. Adapted from [64]

Acceleration inertia $\left(\left(\frac{W}{g}\right)\dot{u}(z_{c.g.} - z_{mg})\right)$ The aircraft was accelerating during the takeoff roll. The acceleration of the aircraft's centre of mass created a pitch up moment promoting takeoff rotation as the aircraft's centre of gravity was above the landing gear's ground contact point.

Thrust $(T(z_t - z_{mg}))$ The engines were located above the ground contact point and created a pitch down moment which resisted takeoff rotation.

Mass moment $(W(x_{mg} - x_{c.g.}))$ The moment generated by the aircraft's centre of gravity, located ahead of the landing gear contact point.

Aerodynamic moment $(M_{a.c.mg})$ The aerodynamic moment generated by the aircraft about the landing gear could either create a net pitch up or pitch down moment depending on the design. In the case of the baseline aircraft, the stabilator could be given a fixed initial incidence to create a positive pitching moment overall for the aircraft about the landing gear.

Effector moment (M_{ellmg}) The elevator(s) deflected 20 deg to create a pitch-up moment to promote rotation. For the case of the baseline aircraft the elevator on the horizontal tail was given an upward deflection. For the box-wing aircraft, elevators ahead of the centre of gravity were given a downwards deflection and those aft of the centre of gravity an upwards deflection.

All aerodynamic forces and moments were evaluated using the pyVORLIN aerodynamic solver with the aircraft in takeoff configuration and in ground effect. In addition to ensuring that the aircraft had sufficient elevator authority to rotate at the specified rotation speed, it was also constrained to have a negative net pitching moment without elevator deflection so the aircraft would not rotate without a pitch-up pilot input (autorotate). Finally, the longitudinal

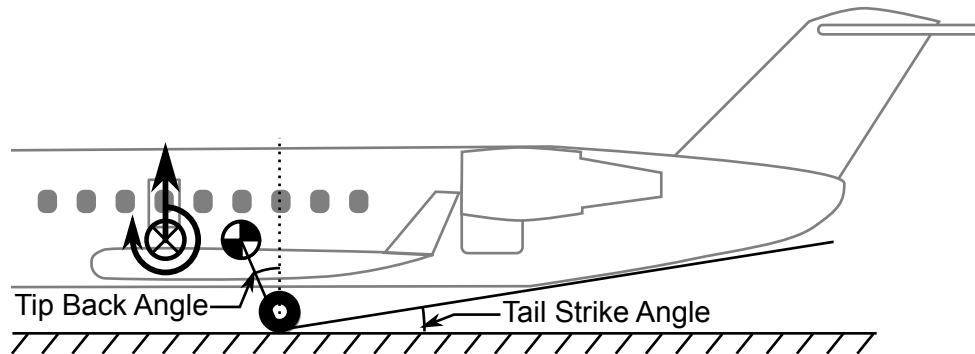


Figure 6.10: Critical landing gear geometry. Adapted from [64]

nal stability of the aircraft was checked at the rotation speed in ground effect. As the aircraft was only in ground effect for a short period of time, the constraints on the static stability of the aircraft were relaxed. However, at all times the aircraft maintained a positive static margin.

6.2.14 Landing gear

Initial estimates of the landing gear geometry and constraints were made using the methods presented in Chapter 3 of [103]. The main gear was assumed to consist of two main struts each with two tires. The nose gear had one strut and a single tire. The tire deflection was calculated to determine the height of the aircraft from the ground at the design weight.

There were four critical landing gear geometry checks which were evaluated for the landing gear.

Tip back The angle between the centre of gravity and the landing gear contact point. Prevented the aircraft from falling on its tail when on the ground. This angle was greater than 15 deg [103]

Tail strike The angle between the landing gear and the lowest point of the tail. Prevented the aircraft from striking its tail on the runway during takeoff. This angle was greater than 10 deg [103]

Tip over Prevented the aircraft from tipping over sideways when performing a turn on the ground. This angle was less than 63 deg [103]

Ground clearance Separation between the ground and the lowest point of the aircraft. This value was greater than 2 ft

The most critical geometry tests were the tip back and tail strike constraints. These two angles are shown in Figure 6.10.

Table 6.2: Mission specifications

Property	Units	Class	
		200	900
Cruise altitude [64]	ft $\times 10^3$	37	37
Cruise Mach number [64]	–	0.74	0.78
Passengers [64]	–	50	86
Range [64]	nmi	965	1540
Fuselage length [64]	ft	87.83	118.75
Takeoff field length limit[64]	ft	5511	6754
Engine bypass ratio	–	6.2	5.0

6.3 Test Cases

Using the multidisciplinary design analysis procedure, a comparison between box-wing and conventional aircraft was made for two regional transport aircraft missions. Previous chapters have focused on box-wing aircraft designed for the same payload and mission as the Bombardier CRJ-200. The aircraft design procedure could also consider a larger variant in the Bombardier CRJ family, the CRJ-900. This aircraft was designed to carry a larger payload and had a greater range than the CRJ-200. Considering different payloads and missions provided more information on the types of missions for which box-wing aircraft were best suited. The box-wing aircraft designed for the CRJ-200 mission was referred to as the 200 class box-wing and the box-wing designed for the CRJ-900 mission was referred to as the 900 class box-wing. The variables and bounds of each test case are given in Section 6.3.1, and the constraints on the problem are given in Section 6.3.2.

Details of the two test cases which were considered in this analysis are given in Table 6.2. These values were constant for both the baseline and box-wing when comparing aircraft designed for the same mission.

6.3.1 Variables

The variables and bounds for the box-wing optimization differed from those for the baseline aircraft. Both sets of variables and bounds are discussed in the following sections.

6.3.1.1 Box-wing analysis

The variables used in the box-wing optimization problem are shown in Table 6.3. There were five major categories of variables: those which resolved interdisciplinary couplings, those which defined the planform geometry, those which defined the effector geometry, those which defined the landing gear geometry and those which were used in the disciplinary analyses to predict aircraft performance. The interdisciplinary coupling variables were required by the problem formulation, as discussed in Section 6.1. The planform geometry of the box-wing aircraft was defined according to the rules given in Section 6.2.1 and Chapter 4. Flap and elevator areas were defined as a fraction of the total wing planform and had additional variables to bias their allocation to the fore or aft wing. The landing gear was assumed to connect to the aircraft fuselage and was located according to four variables, discussed in Section 6.2.1. The final group of variables were those which were used by one or more of the disciplinary models. The sea level static thrust of the aircraft was allowed to vary to values less than the published data for the baseline aircraft to give the box-wing the possibility of using smaller engines than the baseline aircraft if possible. The fore and aft spar locations were also variables to allow box-wing designs to increase the available fuel volume by increasing the separation between the fore and aft spars. The constant CAS climb speed was made a variable to allow the mission specification to best match the box-wing aircraft's aerodynamic performance. Allocation of the empty fuel tank volume fore and aft allowed some degree of control over the aircraft's centre of gravity. The fore and aft centre of gravity limits modified the ranges of the longitudinal centre of gravity as determined from the weights analysis. These variables allowed narrower bounds on the centre of gravity travel to enable the aircraft to meet stability and control constraints.

Table 6.3: Design variable names and bounds for the box-wing problem

Variable Name	Units	Lower bound		Upper bound	
		Class	Class	Class	Class
		200	900	200	900
Interdisciplinary coupling variables					
Maximum takeoff weight	[klbf]	30.0	60.0	60.0	100.0
Manoeuvre angle of attack	[deg]	0	0	20	20
Cruise range	[nmi]	200	500	950	1540
Geometry variables					
Planform area	[ft ²]	350	500	850	2000
Relative fore wing area	[–]	0.2	0.2	0.8	0.8
Height-to-span ratio	[–]	0.0625	0.0625	0.5	0.5
Small wing aspect ratio	[–]	4.0	4.0	10	10
Small wing taper	[–]	0.2	0.2	1.0	1.0
Wing leading edge station	[/l _{fuse}]	0.24	0.17	0.80	0.80
Fan face station	[/l _{fuse}]	0.64	0.70	0.90	0.80
Wing segment sweeps (x3)	[deg]	0.0	0.0	60.0	60.0
Wing section twist (x6)	[deg]	–1.0	–1.0	20.0	20.0
Effector variables					
Main wing flap area	[/S _n]	0.0	0.0	0.3	0.3
Main wing elevator area	[/S _n]	0.0	0.0	0.3	0.3
Fore to aft flap area ratio	[–]	0.0	0.0	1.0	1.0
Fore to aft elevator area ratio	[–]	0.0	0.0	1.0	1.0
Landing gear variables					
Main landing gear axial location	[/l _{fuse}]	0.4	0.4	0.9	0.9
Main landing gear offset	[/d _{fuse}]	0.0	0.0	1.0	1.0
Landing gear strut length	[ft]	0.0	0.0	5.0	5.0
Nose gear axial location	[/l _{fuse}]	0.01	0.01	0.40	0.40
Performance variables					
Maximum sea level thrust	[klbf]	7.0	9.0	11	11
Fore to aft empty tank empty volume ratio	[–]	0.05	0.05	20.0	20.0
Constant CAS climb speed	[knots]	250	250	400	400
Fore spar location	[/c]	0.05	0.05	0.25	0.25
Aft spar location	[/c]	0.75	0.75	0.90	0.90
Fore centre of gravity limit*	[–]	0.01	0.01	0.99	0.99
Aft centre of gravity limit*	[–]	0.01	0.01	0.99	0.99

* Centre of gravity limits were the normalized distance between the fore and aft limits predicted by the centre of gravity analysis.

6.3.1.2 Baseline aircraft analysis

The variables for the baseline aircraft are shown in Table 6.4. The planform geometry of the baseline aircraft was fixed and the effector areas were measured from three-view drawings [64]. The only geometric variables were the twist angles. The two effector variables were the two stabilator incidences during takeoff with fore and aft centre of gravity locations. Since the centre of gravity location and aerodynamic details of the baseline aircraft could not be matched exactly to the real values of the baseline aircraft, some of the landing gear geometry was made variable to allow critical takeoff and landing gear constraints to be met. The spanwise station of the landing gear was constant and taken from published data [64]. The axial station of the main gear was allowed to vary between the leading and trailing edge of the wing at the main gear's spanwise station, and the strut length was also variable. The installed thrust of the baseline aircraft was variable and allowed to drop to below the installed thrust of the in-service aircraft. This was necessary to allow a fair comparison between the optimized baseline and box-wing aircraft.

Table 6.4: Design variable names and bounds for the baseline aircraft problem

Variable Name	Units	Lower bound		Upper bound	
		CRJ	CRJ	CRJ	CRJ
		200	900	200	900
Interdisciplinary coupling variables					
Maximum takeoff weight	[klb _f]	25.0	45.0	100.0	110.0
Manoeuvre angle of attack	[deg]	0	0	20	20
Cruise range	[nmi]	400	600	950	1540
Geometric variables					
Wing section twist (x3)	[deg]	0.0	-2.0	10.0	10.0
Winglet section twist (x2)	[deg]	-5.0	-5.0	10.0	10.0
Effector variables					
Takeoff stabilator, fore c.g.	[deg]	-15.0	-15.0	10.0	10.0
Takeoff stabilator, aft c.g.	[deg]	-15.0	-15.0	10.0	10.0
Landing gear variables					
Main gear axial location	[/ <i>l_{fuse}</i>]	0.410	0.458	0.585	0.611
Landing gear strut length	[ft]	1.5	1.5	10.0	10.0
Nose gear axial location	[/ <i>l_{fuse}</i>]	0.0	0.0	0.4	0.4
Performance variables					
Maximum sea level thrust	[klb _f]	8.0	9.0	15.0	21.0
Constant CAS climb speed	[knots]	250	250	400	400
Fore centre of gravity location*	[-]	0.05	0.05	0.99	0.99
Aft centre of gravity location*	[-]	0.05	0.05	0.99	0.99

* Centre of gravity limits were the normalized distance between the fore and aft limits predicted by the centre of gravity analysis.

6.3.2 Constraints

The box-wing and baseline aircraft were subject to the same set of common constraints. There were six groups of common constraints: interdisciplinary coupling constraints, geometric constraints, landing gear constraints, cruise stability constraints, takeoff constraints and performance constraints. These constraint groups are shown in Table 6.5, the constraint bounds which were dependent on the aircraft mission are given in Table 6.6.

The interdisciplinary coupling constraints ensured that the assumed values of the interdisciplinary coupling variables matched their calculated values.

The common geometric constraints ensured that the fore centre of gravity location was ahead of the aft, and that the angle of twist along the wing did not change too rapidly. The latter constraint was used to prevent the optimizer from exploiting any advantages from rapid changes in twist angle but this constraint was never active in any of the final results used in the analysis. The landing gear constraints ensured that all the critical landing gear geometric parameters met or exceeded the guidelines given in Section 6.2.14. The stability and control constraints both during cruise and takeoff were discussed in Section 6.2.13. The performance constraints ensured that the balanced field length and one engine inoperative second segment climb gradient (C2OEICG) limits were met. The balanced field length limit was chosen as 110% of the published value for the baseline aircraft. The C2OEICG limit was a certification requirement and given in [67]. If there was insufficient thrust when evaluating the aircraft’s performance (Sections 6.2.7), the thrust was increased to the minimum required thrust and the difference noted as the aircraft’s ‘thrust deficit’ (T_{def}). For all converged cases, the thrust deficit was zero. The fuel volume constraint ensured that the volume of fuel which the tanks could accommodate (V_{avail}) was sufficient to hold the fuel required to complete the mission (V_{req}). As in the parametric study in Chapter 4, the stall constraints ensured that no wing panel exceeded its maximum section lift coefficient during a 2.5 g manoeuvre.

6.3.2.1 Exclusive box-wing constraints

There were additional geometric constraints on the box-wing design as its planform geometry was variable. The maximum spanwise extent was limited by the FAA airport gate area guidelines [15]. The maximum vertical limits of the box-wing had an upper bound of the top of the vertical stabilizer and a lower bound of the bottom of the fuselage. The aft wing location was constrained so that, if the aft wing could be attached to the fuselage, the quarter chord point of the aft wing could connect to any point on the fuselage. If the vertical separation was great enough that the aft wing had to connect to the vertical tail, the quarter chord point of the aft wing had to be located so that it passed through the vertical tail. This ensured that the aft wing could connect to the fixed structure of the aircraft. The final geometric constraint was that there was sufficient area available on the wing to place the desired flaps and elevators. Since the optimization problem allowed a wide range of box-wing geometries, there was the possibility that the iterative processes of the structural solver, discussed in Chapter 5, would not converge. If this was the case, the residual remaining after the iterative process exhausted its maximum iterations was added as a constraint. This constraint was zero for all

Table 6.5: Constraints common to baseline and box-wing aircraft

Interdisciplinary coupling constraints	
Cruise lift	$C_L = C_W$
Manoeuvre lift	$C_{L_{mvr}} = 2.5C_W$
MTOW	$MTOW_{in} = MTOW$
Mission range	$R_{in} = R$
Geometric constraints	
Twist rate	$< 2.0 \text{ deg/ft}$
Fore to aft CG	aft c.g. $>$ fore c.g.
Landing gear constraints (with and without fuel, aft c.g.)	
Tip back angle	$> 15.0 \text{ deg}$
Tail strike angle	$> 10.0 \text{ deg}$
Tip over angle	$< 63.0 \text{ deg}$
Ground clearance	$> 2 \text{ ft}$
Nose loading	$0.05 < \frac{W_{n.g.}}{MTOW} < 0.2$
Cruise stability constraints (with and without fuel, fore and aft c.g.)	
Static stability	$0.07 < -\frac{C_{m\alpha}}{C_{L\alpha}} < 2.0$
Negative pitch stiffness	$C_{m\alpha} < 0$
Trimable	$0 < C_{m_o}$
Cruise trim constraint (with fuel, fore c.g.)	
Trimmed	$C_m = 0$
Takeoff constraints (with fuel, fore and aft c.g.)	
No autorotation	$0 > \text{RHS of (6.8)}$
Takeoff rotation	$M_{ell_{mg}} > \text{RHS of (6.8)}$
Takeoff stability	$0.04 < -\frac{C_{m\alpha}}{C_{L\alpha}} \Big _{takeoff} < 2.0$
Performance constraints	
Balanced field length	$\text{BFL} < \text{Max BFL}$
Takeoff second segment OEI CG	$\text{C2OEICG} > \text{Min C2OEICG}$
Performance thrust deficit	$T_{def} < 0$
Fuel volume	$V_{avail} > V_{req}$
Manoeuvre C_l margin	$C_{l_i} < C_{l_{max}} \{i \in 1..n_{pan}\}$

Table 6.6: Design specific constraint bounds

Property	Units	Class	
		200	900
Takeoff field length limit [64]	[ft]	5511	6754
Span limit [15]	[ft]	79	118
Minimum second segment OEI climb gradient [67]	[—]	0.024	0.024

results presented in the following chapter, showing that the structural analysis converged.

6.3.3 Optimization algorithm

A gradient-based optimization algorithm was used to solve the optimization problems for both the baseline and box-wing aircraft where the objective was minimized with respect to the variables given in Section 6.3.1, subject to the constraints given in Section 6.3.2. An existing algorithm, `SNOPT` [68], implemented in the `pyOpt` [69] optimization framework was used as the optimizer. The feasibility tolerance of the `SNOPT` algorithm was set to 1×10^{-7} , and the optimality tolerance set to 1×10^{-4} . All other parameters of the `SNOPT` algorithm were kept at their default values.

Gradient based algorithms had the advantage of locating a mathematically exact optimum which satisfied all constraints to a given tolerance. However, such algorithms cannot perform a thorough search of the designs space and the results are highly dependent on the choice of initial point. Therefore, the results from the parametric study in Chapter 4 were used to locate feasible initial points with low mission fuel consumption.

7 Comparison of Conventional and Box-Wing Aircraft

The aircraft design procedure shown in Chapter 6 was used in the optimization of both a conventional and box-wing aircraft for two missions of varying payload and range. To assess the ability of the analysis to predict the performance of conventional aircraft, the results for the CRJ-200 and CRJ-900 aircraft were compared to published data for these in-service aircraft in Section 7.1. A comparison between the major performance metrics for the two box-wing designs and their conventional counterparts is made in Section 7.2. Sections 7.2.1 to 7.2.4 investigate, respectively, how the disciplines of aerodynamics, mission performance, structures and stability and control affected the performance of the box-wing designs. The critical variable bounds and constraints in the optimization problem are identified and justified in Sections 7.3 and 7.4, respectively. Changes to the mission specification which would be more advantageous to a box-wing aircraft are discussed in Section 7.5.

7.1 Comparison of reference aircraft to published results

Two regional-jet aircraft, the Bombardier Canadian Regional Jet (CRJ)-200 and -900, were used as the baseline aircraft for the present analysis. The CRJ-200 was a short range regional jet while the CRJ-900 was designed for a larger payload and range. Both aircraft were members of the same family of designs and shared a common fuselage diameter, while the CRJ-900 accommodated the increased payload with lengthened fuselage. The results from the optimized reference aircraft, using the problem formulation given in Section 6.3, were compared to the data published by Jane's [64] for these two aircraft. These data are shown in Table 7.1 and the variables defining the optimal designs of both aircraft are given in Table 7.2.

Table 7.1: Comparison of multidisciplinary optimization results with published data for baseline reference aircraft

		CRJ 200			CRJ 900		
		Jane's	Model	Diff.	Jane's	Model	Diff.
Passengers	–	50			86		
Range	nmi	940			1540		
MTOW	lb _f	47500	47500	+0.2%	80500	81500	+1.3%
OEW	lb _f	30300	29600	–2.1%	47500	46400	–2.3
Thrust	lb _f	9220	9380	+1.7%	13100	15600	+19%
BFL	ft	5010	5100	+1.7%	6140	5560	–9.4%

The calculated maximum takeoff weight of both aircraft agree with the Jane's data to within $\pm 5\%$. Of the two designs, the CRJ-900 showed the largest discrepancy in weight and also had more installed thrust than the reference aircraft, indicating that there may be an over-prediction of drag for this design. The takeoff field length of the CRJ-200 was in good agreement with published data, showing the ability of the aerodynamic code to predict maximum lift coefficient and flap effectiveness. The takeoff field length of the CRJ-900 predicted by the model was much smaller than the published data as the sea-level thrust of the optimised design was larger than the existing aircraft.

7.2 Comparison of box-wing and conventional aircraft

The results of the conventional and box-wing optimization problems are shown in Table 7.3. These data are also presented in Figure 7.1 as a 'spider-plot', where the value of each parameter for both the 200- and 900-class box-wing aircraft were normalized by the value for the corresponding baseline aircraft. The variables which defined the optimized box-wing aircraft are given in Table 7.4 and the geometries of these aircraft are shown in Figure 7.2, superimposed on the geometry of the corresponding baseline aircraft.

The cruise lift-to-drag ratio of both the 200- and 900-class box-wing aircraft was superior to the baseline aircraft, as predicted by the parametric study in Chapter 4. The total fuel consumption for the main mission, however, was in both cases larger than the corresponding baseline designs. The planform area of both box-wing designs was more than 20% greater than the corresponding

7.2. Comparison of box-wing and conventional aircraft

Table 7.2: Variables defining the optimized designs of the two baseline aircraft

Variable Name	Units	CRJ	
		200	900
Interdisciplinary coupling variables			
Maximum takeoff weight	[klb _f]	48.2	82.2
Manoeuvre angle of attack	[deg]	2.14	2.57
Cruise range	[nmi]	699	1270
Geometric variables			
Wing root section twist	[deg]	3.18	3.44
Wing crank section twist	[deg]	3.57	4.30
Wing tip section twist	[deg]	4.52	6.04
Winglet root section twist	[deg]	4.86	5.38
Winglet tip section twist	[deg]	6.17	4.40
Effector variables			
Takeoff stabilator, fore c.g.	[deg]	−9.19	−1.26
Takeoff stabilator, aft c.g.	[deg]	−8.92	2.99
Landing gear variables			
Main gear axial location	[/ <i>l_{fuse}</i>]	0.585	0.609
Landing gear strut length	[ft]	3.24	1.97
Nose gear axial location	[/ <i>l_{fuse}</i>]	0.251	0.000
Performance variables			
Maximum sea level thrust	[klb _f]	9.38	15.6
Constant CAS climb speed	[knots]	252	254
Fore centre of gravity location	[−]	0.479	0.168
Aft centre of gravity location	[−]	0.497	0.282

baseline aircraft. Though the lift-to-drag ratio of the box-wings was superior, the total drag of both designs was larger, requiring more fuel to complete the mission. In addition, the wing weights of both the 900- and 200-class box-wing aircraft were larger than the reference aircraft, unlike the findings presented in Chapter 5. The increase in wing weight and main mission fuel weight was driven by the increased planform area.

Though the fuel required to complete the design mission remained almost constant between the baseline and box-wing aircraft, the fuel volume available in the wings to carry this fuel was significantly reduced in the box-wing design, as discussed in Section 2.4. Though the 200-class box-wing required slightly more fuel to complete its mission than the baseline designs, it had roughly 80%

7.2. Comparison of box-wing and conventional aircraft

Table 7.3: Comparison of conventional (CRJ) and box-wing (NPL) aircraft for the 200- and 900-class mission

		200-Class			900-Class		
		CRJ	NPL	delta	CRJ	NPL	delta
Cruise L/D	—	15.8	16.1	+2.0%	16.3	17.4	+6.2%
Planform area	ft ²	587	727	+24%	739	1120	+51%
Fuel weight	lb _f	5630	5910	+5.0%	13600	13800	+1.6%
Total wing weight	lb _f	4550	7290	+60%	7340	12600	+72%
OEW	lb _f	29600	33100	+12%	46400	53600	+16%
MTOW	lb _f	47500	51400	+8.0%	81500	88600	+8.7%
Sea level thrust	lb _f	9380	9650	+2.9%	15600	14700	-5.8%
BFL	ft	5100	5040	-1.1%	5559	5460	-2.1%
Height-to-span	—	-	0.308		-	0.250	
Stagger	$/\frac{1}{2}b$	-	0.890		-	0.957	
Fore wing area	$/S_n$	-	0.500		-	0.498	

of the fuel storage capacity of the baseline aircraft. The CRJ-200 had excess volume available in its wings, so the planform area of the 200-class box-wing did not need to increase as much as the 900-class to accommodate the mission fuel. In Figure 7.1, the 900-class aircraft was shown to have the same fuel capacity as the baseline aircraft. The fuel volume constraint was active for both designs and led to the 51% increase in planform area between the 900-class box-wing and baseline design. The effect of this fuel volume constraint on the design of the 900-class box-wing is examined further in Section 7.4.

Subsequent sections will examine the effects that the key disciplines of aerodynamics, mission performance, structures and stability had on the performance of the box-wing aircraft and discuss how they contributed to the overall findings shown in Table 7.3 and Figure 7.1

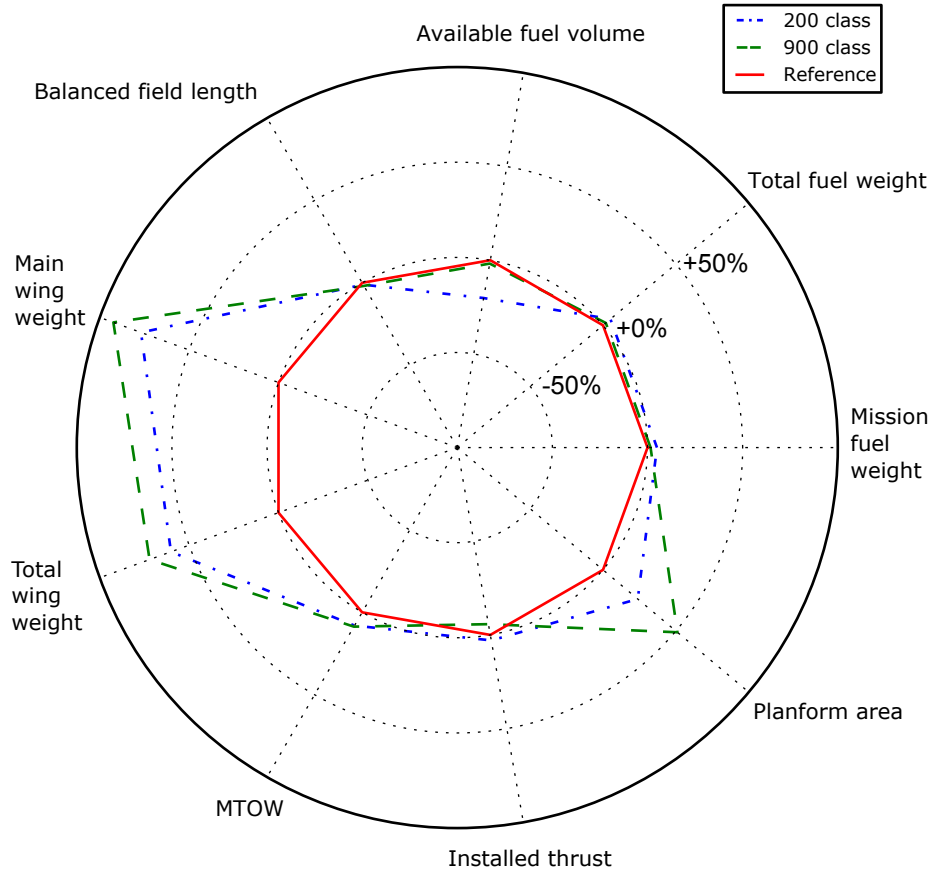


Figure 7.1: Comparison of major performance metrics of the 200- and 900-class box-wings, relative to conventional designs

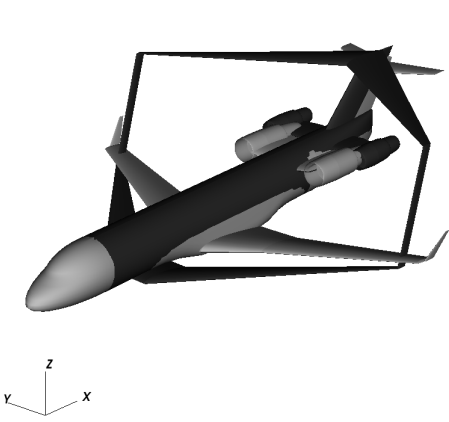
7.2. Comparison of box-wing and conventional aircraft

Table 7.4: Variables defining the optimal designs for the two box-wing aircraft

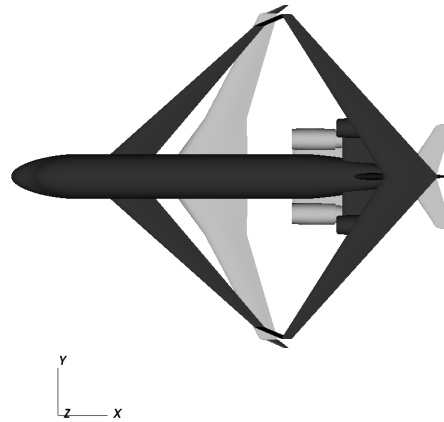
Variable Name	Units	Class	
		200	900
Interdisciplinary coupling variables			
Maximum takeoff weight	[klb _f]	51.3	88.8
Manoeuvre angle of attack	[deg]	2.18	2.38
Cruise range	[nmi]	690	1200
Geometry variables			
Planform area	[ft ²]	727	1120
Relative fore wing area	[–]	0.500	0.493
Height-to-span ratio	[–]	0.308	0.250
Small wing aspect ratio	[–]	10.0	9.45
Small wing taper	[–]	0.218	0.357
Wing leading edge station	[/ <i>l_{fuse}</i>]	0.241	0.310
Fan face station	[/ <i>l_{fuse}</i>]	0.819	0.704
Fore wing sweep	[deg]	48.4	45.9
Vertical wing sweep	[deg]	16.7	19.0
Aft wing sweep	[deg]	32.4	39.7
Fore wing root twist	[deg]	3.68	4.66
Fore wing midspan twist	[deg]	5.62	7.84
Fore wing tip twist	[deg]	7.00	2.96
Aft wing tip twist	[deg]	4.12	1.92
Aft wing midspan twist	[deg]	3.00	2.03
Aft wing root twist	[deg]	0.89	4.08
Effector variables			
Main wing flap area	[/ <i>S_n</i>]	0.00	0.024
Main wing elevator area	[/ <i>S_n</i>]	0.151	0.120
Fore to aft flap area ratio	[–]	0.634	0.419
Fore to aft elevator area ratio	[–]	0.421	0.369
Landing gear variables			
Main landing gear axial location	[/ <i>l_{fuse}</i>]	0.611	0.606
Main landing gear offset	[/ <i>d_{fuse}</i>]	0.991	0.556
Landing gear strut length	[ft]	3.90	4.95
Nose gear axial location	[/ <i>l_{fuse}</i>]	0.335	0.274

Table 7.4 (continued): Variables defining the optimal designs for the two box-wing aircraft.

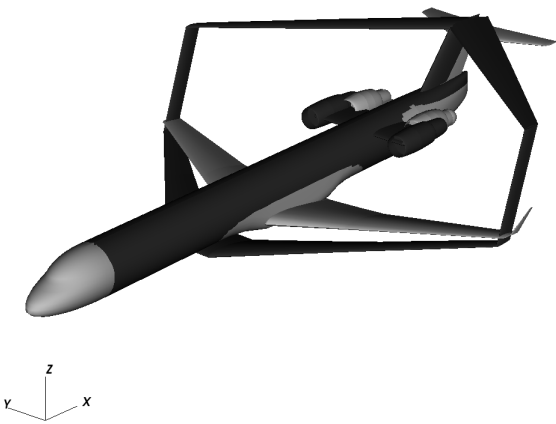
Performance variables			
Maximum sea level thrust	[klbf]	9.65	14.7
Fore-to-aft empty tank empty volume ratio	[-]	11.6	5.94
Constant CAS climb speed	[knots]	255	255
Fore spar location	[/c]	0.057	0.093
Aft spar location	[/c]	0.789	0.808
Fore centre of gravity limit	[-]	0.912	0.180
Aft centre of gravity limit	[-]	0.912	0.396



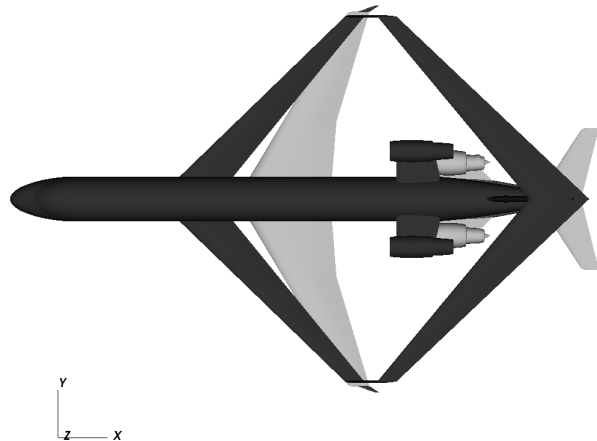
(a) 200-class



(b) 200-class



(c) 900-class



(d) 900-class

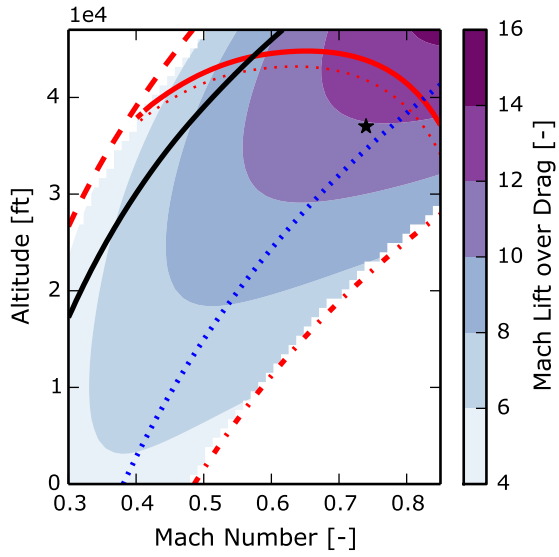
Figure 7.2: Comparison of optimized baseline and box-wing aircraft geometries

7.2.1 Aerodynamics

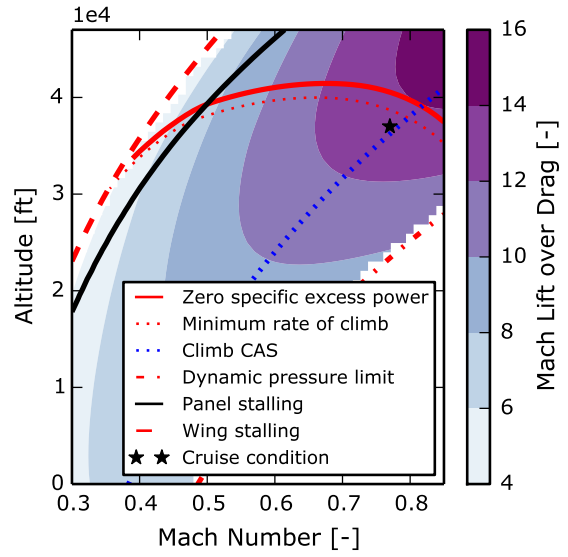
The aerodynamic performance of the box-wing aircraft was examined throughout their performance envelope. These data are presented as ‘sky-maps’ [104] where contours of independent variables were plotted over a range of Mach and altitude combinations. These contours were bounded by the aircraft’s operating envelope. At low speeds, the envelope was limited by stall. The contours of both where local stalling first occurs on the wing and where the wing is fully stalled are shown. At high altitudes, the performance of the aircraft was limited by the available power of the engines, shown by the contours of zero specific excess power. At high speed and low altitudes, the performance envelope was defined by the maximum dynamic pressure the structure could withstand, assumed to be $350 \text{ lb}_f/\text{ft}^2$. This was the dynamic pressure when the CRJ-200 aircraft was operating at its cruise speed +15% at the manoeuvre altitude.

Sky maps of product of Mach number and lift-to-drag ratio (MLD) ratio are shown for both the 200- and 900-class box-wing aircraft. In addition, contours of the difference between the MLD of the box-wing and baseline aircraft at each Mach and altitude are shown, with positive values indicating an advantage for the box-wing. The MLD ratio was used as the independent variable as it represented the aerodynamic terms of the fuel weight equation (1.1) at a fixed altitude. The MLD value at a given altitude is inversely proportional to the fuel consumed for a fixed range mission with a fixed weight at the start of cruise and an engine of fixed specific fuel consumption.

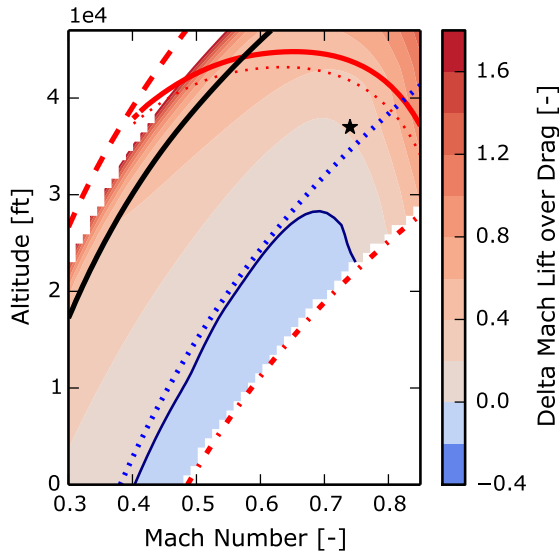
Both the 900- and 200-class aircraft operated near their maximum achievable MLD values. For both aircraft, the engines were sized such that the box-wing had sufficient excess power to climb at the design point but were operating close to their service ceiling at the cruise Mach number. The contours of the delta MLD showed the regions where the box-wing designs had an advantage over the baseline aircraft. In both cases, the delta MLD increased as the design Mach number decreased and cruise altitude increased. These regions required the aircraft to operate with a larger lift coefficient than at the design point, showing the box-wing’s induced drag advantage.



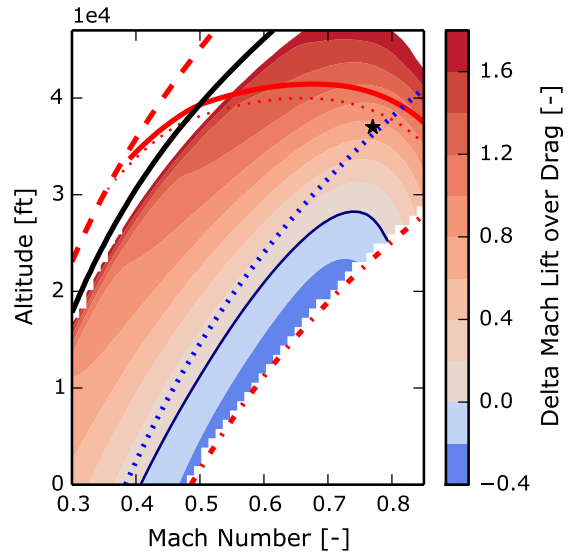
(a) 200-class box-wing



(b) 900-class box-wing

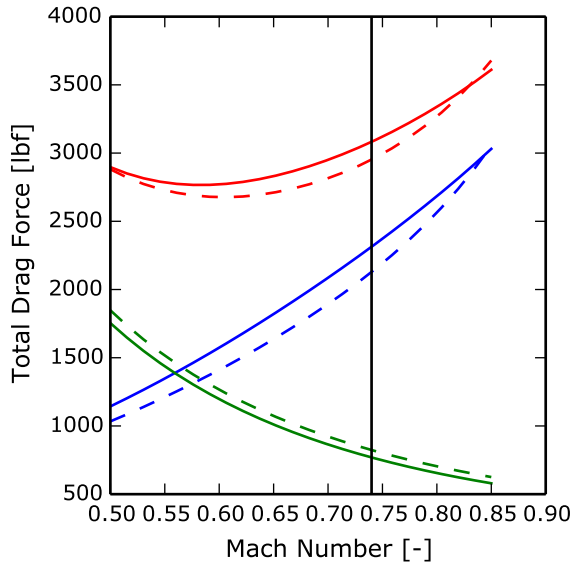


(c) 200-class box-wing less reference

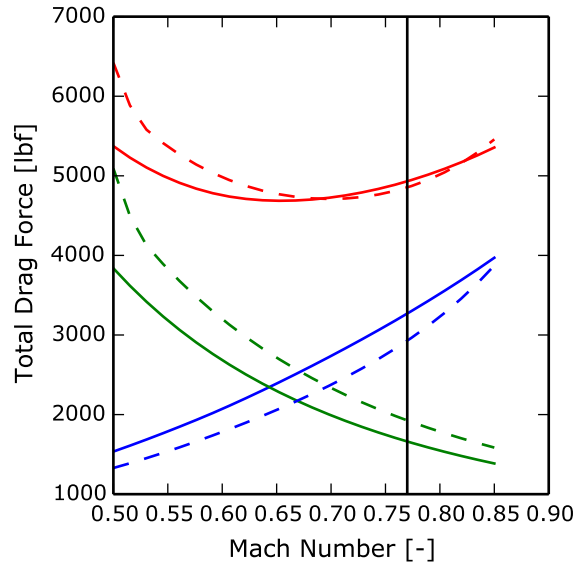


(d) 900-class box-wing less reference

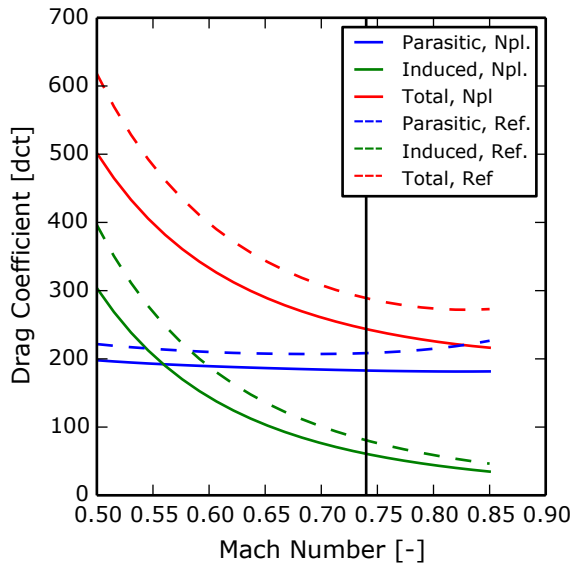
Figure 7.3: Sky-maps showing the Mach-lift-to-drag ratio of both aircraft sizes



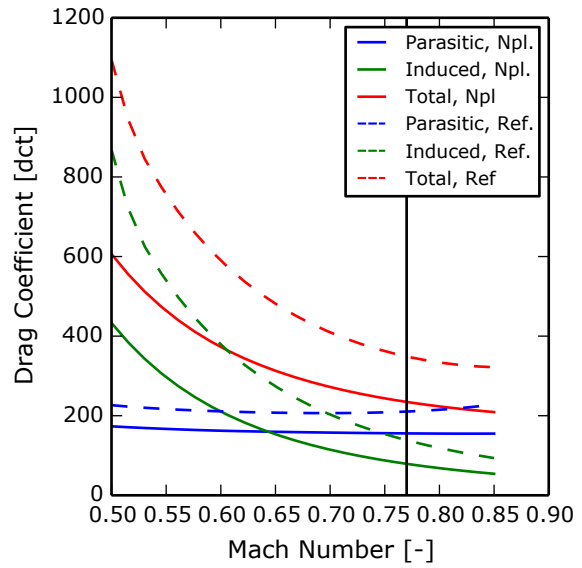
(a) 200-Class



(b) 900-Class



(c) 200-Class



(d) 900-Class

Figure 7.4: Comparison of drag forces and drag coefficients of the box-wing to the baseline aircraft for the 200- and 900-class missions over a range of Mach numbers at the cruise altitude. The vertical line represents the cruise Mach number.

The contributions of induced and parasitic drag to the total drag force of the 200- and 900-class box-wing aircraft are shown in Figures 7.4a and 7.4b. The 200-class box-wing did not show an advantage in total drag force over the baseline aircraft at speeds below the cruise Mach number. Though the 200-class aircraft had a lower induced drag force than the baseline aircraft, the increased parasitic drag led to an increase in total drag force compared to the baseline. At the design Mach number, the total drag force on the 900-class aircraft was slightly greater than that of baseline aircraft. However, unlike the 200-class box-wing, at Mach number less than 0.65, the reduced induced drag of the 900-class aircraft gave it a significant advantage in terms of total drag force, despite the increased planform area of the 900-class aircraft. Both the 900- and 200-class box-wings showed an advantage in total drag at high Mach numbers due to the larger sweep angle of the fore and aft wings compared to the baseline aircraft. This was the speed regime where the Lockheed transonic biplane concept was intended to operate [9]. Though the box-wing designs had an advantage over the baseline aircraft at these speeds, they still would consume significantly more fuel than at the design mission and would not be preferable on an environmental basis.

The breakdown of the drag coefficients of the 200- and 900- aircraft are compared to their corresponding baseline designs in Figures 7.4c and 7.4d. The total drag coefficient of both box-wing aircraft designs was lower than the baseline aircraft, showing that it was the increased planform area which led to the increased drag force of the box-wing designs. For all speeds, both the induced and parasitic drag coefficients of the box-wing aircraft were less than the baseline designs, showing that the box-wing design did have aerodynamic advantages when compared to an aircraft of equal planform area.

The 900-class box-wing achieved greater reductions in induced drag compared to the baseline aircraft than the 200-class box-wing. This may be attributed to the reduced stagger between the fore and aft wings. Though the difference in the separation, shown in Table 7.3, was small, it corresponded to the point in the parametric study shown in Figure 4.3, when lift-to-drag ratio began to decrease significantly with reduced stagger. The stagger of the 200-class aircraft was limited by the requirement that the fore wing attach to the fuselage aft of the main cabin door so gate servicing equipment could access the cabin. The 900-class aircraft carried more passengers than the 200-class but had the same fuselage diameter. The extra passengers were accommodated in a lengthened fuselage. This allowed increased stagger of the 900-class box-wing without interfering with the cabin door. The difference in stagger between the 200- and 900-class box-wings can be seen by comparing the top views of both aircraft shown in Figure 7.2.

The parametric study in Chapter 4 predicted that there would be an advantage in lift-to-drag ratio for designs smaller fore wing areas. The optimized results for both the 200- and 900- class box-wings, however, had equal area wings. In the parametric study the centre of gravity could be placed freely while in the multidisciplinary study, the centre of gravity was dependent on the weights of the individual aircraft components. A small fore wing and large aft wing would force the centre of gravity aft, making it challenging to meet takeoff rotation and trim constraints. The optimization has traded the slight lift-to-drag advantage of a smaller fore wing for a more forward centre of gravity position.

7.2.2 Mission performance

The climb and cruise portions of the design mission of the 200- and 900-class box-wing aircraft are shown in Figure 7.5. The most efficient climb profile occurs when the contours of constant specific excess power are tangent to contours of constant energy height. The baseline aircraft were designed to climb at 270 knots CAS and the lower limit on climb speed was 250 knots CAS. Even at the lower speeds, the box-wing aircraft could not climb at the most efficient point, but both the box-wing and baseline aircraft climbed close to 250 knots CAS to improve their performance.

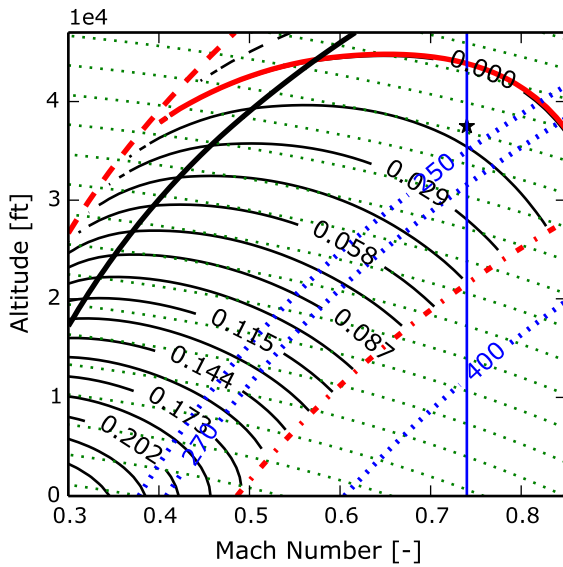
The cumulative fuel consumption of the box-wing and baseline aircraft as a function of distance travelled is shown in Figures 7.5c and 7.5d for the 200- and 900-class box-wings. The 200-class box-wing climbed at roughly the same rate as the baseline aircraft as both aircraft had similar performance during climb in terms of fuel consumed per nautical mile travelled. The 900-class box-wing, however, climbed more slowly over a longer distance as the aircraft had a performance advantage at lower speeds. Though the aircraft burnt more fuel to reach cruise altitude, it covered more distance over the ground and spent less time in the cruise phase, where the 900-class box-wing burnt more fuel per nautical mile travelled than the baseline aircraft.

The aerodynamic advantages at cruise of the box-wing design were discussed in Section 7.2.1. However, both the engine size and weight of the box-wing aircraft differed from the baseline design. A more meaningful comparison of the aircraft's performance during the cruise phase of the mission was a comparison of the Specific Air Range (SAR) of the aircraft.

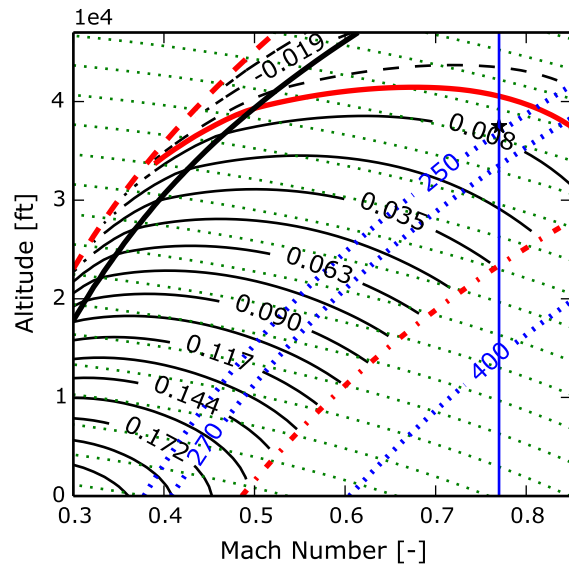
$$SAR = \frac{a Ma C_L}{SFC_T C_D} \frac{1}{W_s} \quad (7.1)$$

Specific air range represented the distance travelled, in feet, per pound of fuel consumed by the aircraft. Increased values of SAR corresponded to

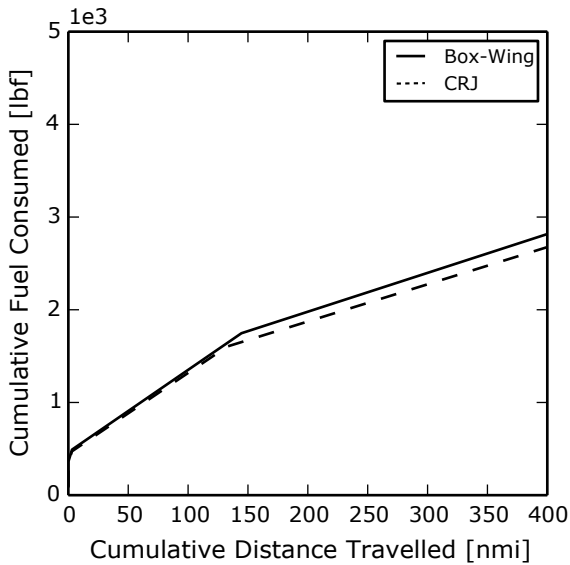
increases in the MLD value and decreases in the engine specific fuel consumption, SFC_T , and weight at the start of cruise, W_s . Figures 7.6c and 7.6d show the difference between the SAR of the two box-wing and baseline aircraft over a range of Mach numbers and altitudes. The 200-class aircraft had inferior performance over almost the entire operating envelope. The aerodynamic advantages of the 900-class aircraft at Mach numbers below the design point translated into an advantage in specific air range at Mach numbers below approximately 0.65. The absolute value of specific air range, however, decreased with decreasing Mach number. The box-wing aircraft was operating close to its optimal point. These results indicate, however, that were the box-wing and baseline aircraft re-sized to operate at a lower Mach number, the box-wing may have a fuel burn advantage.



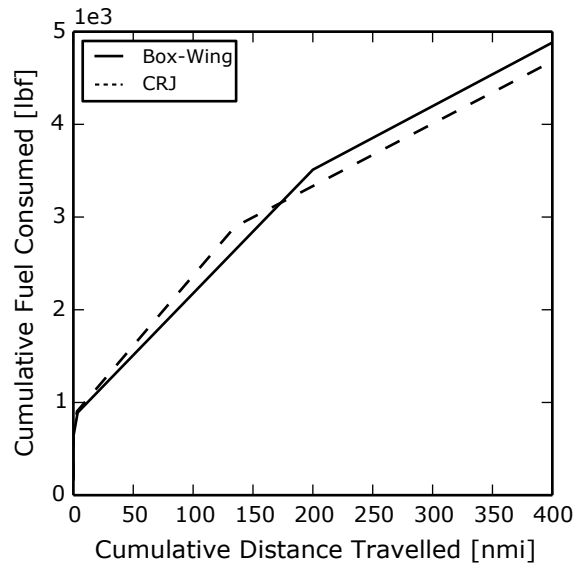
(a) 200-Class



(b) 900-Class

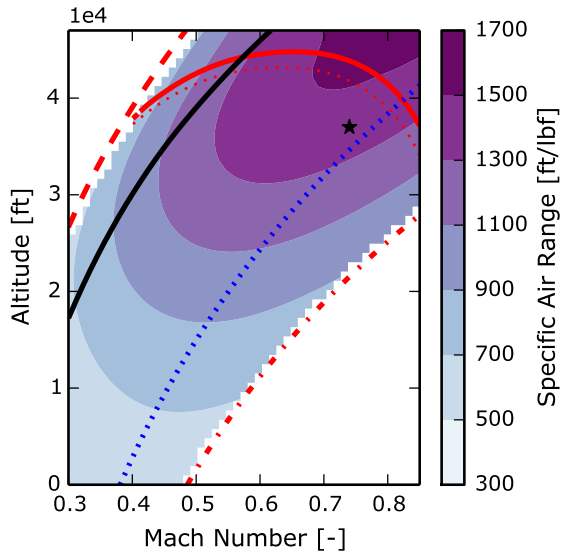


(c) 200-Class

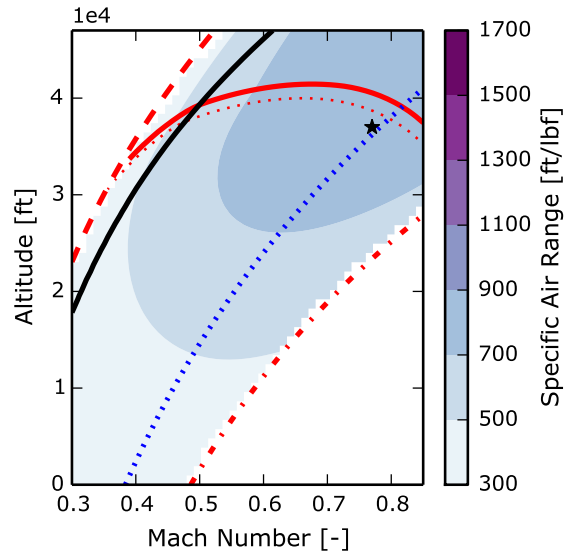


(d) 900-Class

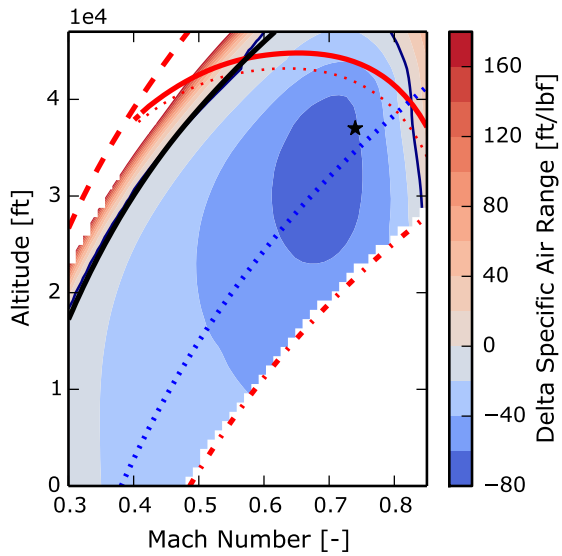
Figure 7.5: Details of box-wing performance throughout the missions. Contours of constant dimensionless specific excess power within the flight envelope are shown in Figures (a) and (b). The dotted green lines in these figures represent constant values of energy height and the dotted blue lines represent constant values of CAS in knots; otherwise these figures share the same legend as in Figure 7.3.



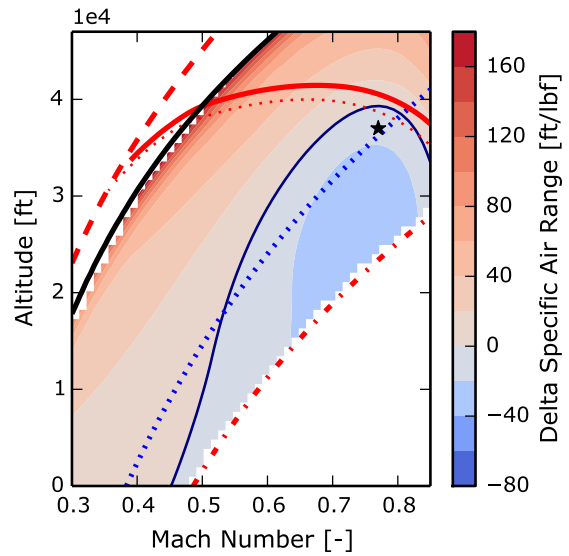
(a) 200-class box-wing



(b) 900-class box-wing



(c) 200-class box-wing less reference



(d) 900-class box-wing less reference

Figure 7.6: Sky maps showing the specific air range for both aircraft sizes.

Table 7.5: Comparison of optimized 200-class box-wing and baseline aircraft with various structural cases

		Baseline	200-Class	Case I	Case II	Case III
Total wing weight	lb _f	4550	7290	5910	4430	3950
Primary structure	lb _f	2580	5840	4770	3230	2800

7.2.3 Structures

The increase in wing weight of the 200- and 900-class box-wings compared to the baseline aircraft was significantly larger than predicted based on the results of Chapter 5. The analysis in Chapter 5 assumed that the planform area and spar placements were the same between the box-wing and baseline aircraft whereas in the present analysis, they could vary. Table 7.5 compares the structural weight of the baseline aircraft to the optimized 200-class box-wing aircraft as well as to designs which have been manually adjusted to match the baseline aircraft in various respects. Case I set the planform area of the baseline and box-wing to be equal, as well as set the height-to-span ratio to 0.25. Case II also changed the fore and aft spar positions from their optimized values of 0.057 and 0.789 to the baseline values of 0.15 and 0.75. Case III changed the aspect ratio of the main wing and the MTOW of the aircraft to match the baseline. It should be noted that Cases I - III were not optimized so many of the stability and control constraints were violated in these analyses, which were only focused on the weight of the wing.

The changes in Case I brought the planform shape of the wing inline with the analysis in Chapter 5 which showed box-wing and baseline wings of approximately equal weight. However, the Case I results were still significantly heavier than the baseline aircraft. Only by returning the spar placement to the original positions was the wing weight brought in-line with the baseline.

Increasing the separation of the fore and aft spars increased the weight of the wing for two reasons. First, it increased the area of the wing skins and spar webs, which were noted in Chapter 5 to be constrained by the minimum gauge thickness along most of the span. Second, the local thickness of the aerofoil section was smaller close to the leading and trailing edge of the aerofoil compared to near the quarter chord point. This meant that the fore and aft spar booms were located closer to the neutral axis of the cross section and needed to have a larger area to create the same moment of inertia to resist bending moments than if they were located at their baseline positions.

7.2.4 Stability and control

Unlike aerodynamics and structures, the degree of stability of the box-wing designs cannot be quantified in a single value. The stability and control requirements of the aircraft were enforced through the many constraints placed on the aircraft. The design was tested at fore and aft centre of gravity positions, both during cruise and takeoff, as described in Section 6.3.2.

All these constraints were met in feasible designs but the box-wing designs showed some unusual trends compared to the baseline aircraft during takeoff. There was only a small subset of box-wing designs which could meet the takeoff rotation constraint. There were four principal reasons for this. The first was that the aft wing, though located as far aft as possible while remaining attached to the vertical tail, did not have as large an effective moment arm as horizontal tail of the baseline aircraft. The baseline aircraft's horizontal tail was swept aft of the vertical tail, while the aft-most surface of the box-wing had to be swept forward, see Figure 7.2. Second, the baseline aircraft had an all-moving tail which was able to be set at a negative incidence during takeoff to generate a pitch-up moment to counteract the pitch-down moments of the aircraft mass, rotational inertia and thrust. This reduced the elevator moment required for takeoff rotation. Third, the centre of gravity of the box-wing was located higher than the baseline aircraft. This meant that the landing gear had to be located farther aft of the centre of gravity to meet the landing gear tip-back constraint. Fourth, the static margin of the box-wing aircraft was significantly reduced in ground effect, limiting how far aft of the centre of gravity the aerodynamic centre could be located and making it challenging for the box-wing design to generate significant pitch-up moments without elevator deflections.

The final point is shown in more detail in Figure 7.7 which compared the static margin in ground effect to the value when the aircraft was out of ground effect. Both the box-wing and baseline aircraft showed a reduction in static margin. Though the ground effect reduced the strength of the downwash, promoting stability [58], it also caused a greater increase of lift on wings closer to the ground plane. In both the box-wing and baseline aircraft, the fore, or main wing, was located much closer to the ground than the aft wing, or horizontal tail. As the fore and main wings were located ahead of the centre of gravity, this created a destabilizing effect, which counteracted the stabilizing influence of the reduced downwash. Chapter 3 showed that the static stability of the box-wing was sensitive to the area distribution between the fore and aft wings as the larger fore wing increased the strength of the destabilizing fore wing's downwash. The increased lift of the fore wing had a similar effect to increasing its effective area and led to the decrease in static margin.

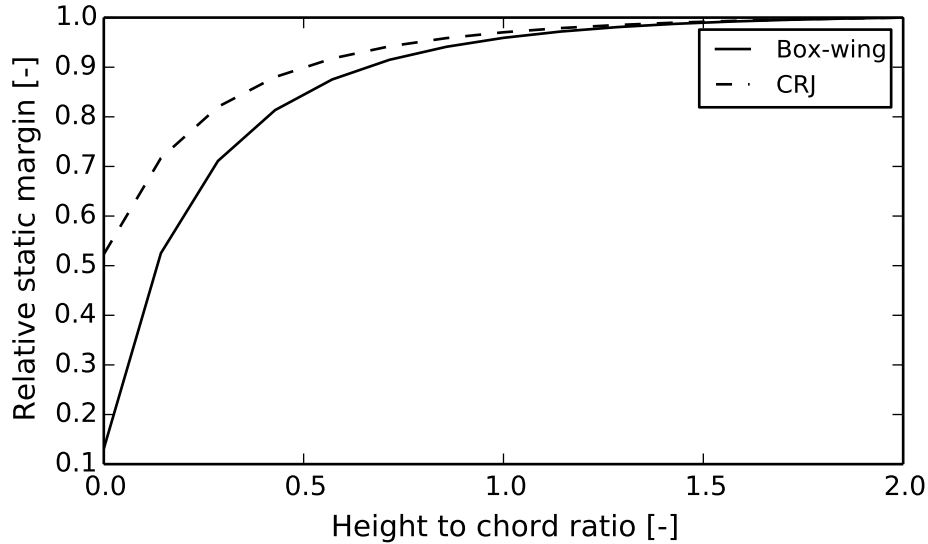


Figure 7.7: Static margin relative to the value when out of ground effect for the 200-class box-wing and CRJ 200 . The horizontal axis shows the distance of the aircraft’s centre of gravity to the ground, normalized by the reference chord

7.3 Active variable bounds

Some of the choices made for the bounds of the variables of the optimization problem were found to limit the performance which the box-wing designs were able to achieve. The following sections detail these critical variable bounds and provide justification for their choice.

7.3.1 Aspect ratio

The maximum span of the box-wing aircraft was limited by the FAA airport guidelines. However, this constraint was not sufficient to prevent the fore and aft wings of the box-wing aircraft from adopting extremely high aspect ratios. If the planform area of the CRJ-200 was divided equally between fore and aft wings, each wing would have an aspect ratio of 21 if the span constraint was active. A much lower bound of 10 was imposed on the designs as this was the largest aspect ratio used in the validation study of aircraft wing weights, presented in Chapter 5. Studies of the 900-class aircraft with a higher aspect ratio bound of 15 showed a cruise lift-to-drag ratio of 19.5

and an improvement in fuel burn of 10%, indicating that there is a fuel burn advantage to increasing the aspect ratio beyond the limit of 10. However, this comparison was against the baseline CRJ-900 model with an aspect ratio of 7. If a generic cantilevered wing with a winglet was also designed with an aspect ratio of 15, the advantages would be less significant.

7.3.2 Engine location

The forward location of the engines was an active variable bound in the analysis. The forward limit was chosen so that the engines were aft of the passenger compartment so passengers were clear of damage resulting from a burst rotor. The aft limit of engine position was chosen so that the engine could be attached to the cylindrical portion of the fuselage to allow the engine's thrust to be transferred to the aircraft.

7.3.3 Wing leading edge station

The forward limit on the wing leading edge station was chosen so that the wing would be located aft of the main passenger door of the reference aircraft. This would allow the aircraft to be serviced with existing airport equipment as well as meet certification requirements for an emergency exit. Chapter 4 showed that the performance of a box-wing aircraft increased with increasing stagger of the wings. In the case of the 200-class box-wing aircraft, with a short fuselage, this variable bound was active and limited the possible aerodynamic performance of the aircraft.

7.4 Dominant constraints

Several constraints dominated the design and limited the performance which the box-wing designs could achieve. This section examines their impact in more detail.

7.4.1 Fuel volume

The previous sections have highlighted the negative effects which the increased planform area and fore-aft spar spacing of the 900-class wing had on the fuel burn of this box-wing design. Another optimization was performed with the fuel constraint removed and the planform area of the aircraft reduced to that of the baseline aircraft. All stability and control as well as takeoff field length constraints were met and the aircraft achieved an improvement in both the cruise lift-to-drag ratio and the weight of fuel required for the mission.

Table 7.6: Comparison of a 900-class CRJ and box-wing aircraft with and without the fuel volume constraint.

		CRJ	NPL	Diff.
MTOW	lb _f	81500	83200	+2.1%
Wing weight	lb _f	7340	8570	+16%
Planform area	ft ²	739	739	+0.0%
Fuel weight	lb _f	13600	13439	-1.2%
Lift-to-drag	–	16.3	17.1	+4.9%
Volume deficit (surplus)	ft ³	(60.3)	129	

The aircraft, however, had a significant volume of fuel which could not be accommodated in the wing tanks and was modelled as a point mass at the centre of gravity of the fuel tanks. The unallocated volume of fuel was almost equal to the volume of fuel carried in one of the baseline aircraft’s port or starboard wing tanks. This volume of fuel would be difficult to integrate into the baseline aircraft cabin without making significant changes to the fuselage geometry.

However, it is important to note that volume constraints rather than stability, takeoff rotation or field length constraints led to the increased planform area of the optimized 900-class box-wing design.

Even if the design of the fuselage was modified to accommodate sufficient fuel stores, there are certification requirements, given by the United States’ Code of Federal Regulations, which would have to be addressed when storing fuel within the fuselage. Applicable regulations include 14CFR§25.963(d) [91]

Fuel tanks must, so far as it is practicable, be designed, located, and installed so that no fuel is released in or near the fuselage, or near the engines, in quantities that would constitute a fire hazard in otherwise survivable emergency landing conditions...

The definition of a “survivable emergency landing” is elaborated on in 14CFR§25.721(b) [91]

The airplane must be designed to avoid any rupture leading to the spillage of enough fuel to constitute a fire hazard as a result of a wheels-up landing on a paved runway...

The added projected area and wetted area of the fuselage as well as the increased structural weight to meet the certification requirements shown above may erode any of the performance advantages provided by storing fuel internally.

7.4.2 Takeoff constraints

The choice of the tip-back angle and minimum takeoff static margin both affect the performance of the box-wing aircraft. The 15 deg limit used in the present study was not a certification requirement but a guideline. If the tip-back angle was reduced slightly, the landing gear would be located closer to the centre of gravity, reducing the moment generated by the aircraft's mass acting against takeoff rotation. Likewise, the certification requirement for static stability is only that the static margin be positive; the choice of 4% was a guideline rather than a requirement and if the centre of gravity was located further aft of the aircraft's neutral point, the wings could generate a larger pitch-up moment during the takeoff roll to assist in takeoff rotation.

7.5 Changes to make the box-wing preferable

The comparison of box-wing aircraft to equivalent conventional designs showed that though box-wings had some advantages in aerodynamic performance, they were ill suited to the regional jet transportation mission. For both short and long range regional jet aircraft, the box-wing design did not yield any savings in fuel burn.

There were two significant factors that prevented box-wings from achieving a sufficient reduction in fuel burn to be considered as a next-generation regional-jet design. The first was the Mach number of the design mission. Box-wing aircraft achieve reductions in induced rather than parasitic drag and at the design Mach number, the aircraft had a low required lift coefficient. If the Mach number of the design mission were reduced to between Mach 0.5 and 0.6, the box-wing designs, particularly the long range regional jet, would have an advantage in terms of both total drag and specific air range which could translate into fuel savings relative to the baseline aircraft. The second factor limiting the box-wing design was the reduced fuel volume inherent to the wing geometry. The box-wing was designed to carry all its fuel in wing tanks. This led to significant increases in the planform area of the box-wing designs to accommodate the fuel required to complete the mission. If sufficient space was found in the cabin to accommodate the extra fuel, the box-wing showed a slight fuel burn advantage.

A better mission choice for box-wing aircraft may be a high-altitude long-endurance uninhabited aerial vehicle. Without the requirement of carrying passengers or crew, the aircraft's fuselage would not be as constrained by available volume and could carry a large fraction of the mission fuel. In addition, the shape of the body could be long and slender, allowing significant

7.5. Changes to make the box-wing preferable

separation of the wings, which was shown to increase aerodynamic performance. The aircraft would loiter at low speed and high altitude, increasing the lift required from the wings. In addition, induced drag reductions are more advantageous to loiter missions compared to cruise.

8 Conclusions

Unconventional aircraft configurations are an important field of research in order to limit the growth of transport aircraft's environmental impact. There are many such designs being investigated; however, box-wings have the advantage that they comply with existing regulations and airport design guidelines. The results of Chapter 3 and 4 showed that the box-wing designs can be made inherently stable and Chapter 7 showed that such a design can meet takeoff field constraints. Existing aircraft regulations would not need to be amended to enable the operation of a box-wing aircraft. In addition, the box-wing design met all airport gate constraints and was able to be serviced by existing airport facilities. Compared to other unconventional aircraft designs such as truss-braced wing aircraft or blended-wing-body aircraft, this would reduce the modifications required to airport infrastructure necessary to incorporate a novel aircraft design.

Box-wings were unique amongst various unconventional aircraft configurations discussed in Chapter 1 as they presented the opportunity to include an unconventional aircraft design into existing infrastructure and regulatory frameworks. However, the most important metric for assessing the merit of an unconventional aircraft was the reduction in fuel burn which such a configuration could achieve when compared to the best possible conventional aircraft design. In this respect, the box-wing configuration did not provide an advantage over conventional aircraft. Though a box-wing aircraft could achieve a greater lift-to-drag ratio than conventional designs, and met all operation constraints, the requirement to carry all mission fuel in the wings increased the planform area of the box-wing to the point where the total drag on the aircraft during its design mission was greater than that of a conventional design. The aircraft could carry fuel in the fuselage; however, it would have to meet several challenging certification requirements in order to do so.

Though box-wing aircraft were found to be ill suited to the passenger transport mission, the results of the box-wing studies presented in this thesis showed several important trends in the design of such aircraft which indicate

that the design may be well suited to alternate missions. Chapter 3 presented a novel analytic formulation for modelling the stability of aircraft designs which use two main wings to both generate lift and achieve trim and stability. It was shown that box-wing aircraft could be made stable but that the configuration with the highest lift-to-drag ratio was also statically unstable. In addition, it was noted that increasing the separation between the main wings decreased the stability of the design. The reason for these two behaviours was attributed to the asymmetric distribution of the downwash upstream and downstream of a wing. These results showed that the desire for a large lift-to-drag ratio in a box-wing aircraft was in conflict with the requirement for static longitudinal stability. A more detailed aerodynamic model was used in Chapter 4 to carry out a parametric study of box-wing designs to estimate the performance penalty which stability requirements imposed. The results of this study showed that designs with large streamwise and vertical spacing between the wings incurred a negligible penalty in lift-to-drag ratio when maintaining trim and longitudinal stability. Stable box-wing designs could achieve higher lift-to-drag ratios than a conventional wing plus horizontal tail.

These investigations showed that box-wings have an aerodynamic advantage over conventional aircraft; however, it was unclear what impact the closed wing design would have on the weight of the main wing structure. A novel wing weight estimation model was developed in Chapter 5. This model idealised the internal structure of the wing into an aerofoil conforming hexagon and was able to solve for the statically indeterminate distribution of internal moments and forces resulting from the applied loading. This model showed that there was a conflict between designs with the lowest structural weight and designs with the best aerodynamic performance. However, the structural penalty from the aerodynamically preferable design had a much smaller impact on the fuel required to complete the mission than if the wing were designed for minimum structural weight.

The studies performed in Chapters 3 to 5 showed that there were important interactions between the desire for both high lift-to-drag ratio and low structural wing weight and the requirement for static longitudinal stability in a box-wing design. A multidisciplinary study was discussed in Chapters 6 and 7 which investigated the couplings between these three disciplines as well as considered the aircraft's performance throughout its mission, takeoff constraints, propulsion system sizing, landing gear constraints and fuel tank sizing. The addition of these disciplines to the multidisciplinary analysis allowed the performance of the box-wing aircraft to be compared against in-service aircraft designs to determine the suitability of the box-wing design to the transport mission.

Though the multidisciplinary study determined that there was no advantage with respect to fuel burn from using a box-wing design for a regional transport mission, the trends observed in this study showed that the box-wing would be well suited to alternate missions, specifically an unmanned high altitude surveillance aircraft. In addition, the multidisciplinary study showed that it was the fuel volume constraint, rather than stability or take-off performance constraints, which was the primary reason that the box-wing design was not preferable for the transport mission.

Though the box-wing did not compare favourably to the best conventional aircraft designed for the regional-jet transport mission, alternate mission specifications were identified where the box-wing configuration had superior performance. Investigations of the individual disciplines of stability, aerodynamics and structures as well as the multidisciplinary study showed important trends in the design of box-wing aircraft which will enable aircraft with performance superior to conventional designs for these alternate missions.

Bibliography

- [1] Andrews, S. A. and Perez, R. E., “Parametric Study of Box-Wing Aerodynamic Design for Minimum Drag Under Stability and Maneuverability Constraints,” *33rd AIAA Applied Aerodynamics Conference*, 2015-3291, AIAA, Dallas TX, June 2015.
- [2] Andrews, S. A., Perez, R. E., and Wowk, D., “Wing weight model for conceptual design of nonplanar configurations,” *Aerospace Science and Technology*, Vol. 43, June 2015, pp. 51–62.
- [3] U.S. Department of Transportation Bureau of Transportation Statistics, “National Transportation Statistics,” Tech. rep., Washington, DC, 2014.
- [4] Bradley, M. K. and Droney, C. K., “Subsonic Ultra Green Aircraft Research: Phase I Final Report,” CR- 2011-216847, NASA, Washington, DC, 2011.
- [5] Bradley, M. K. and Droney, C. K., “Subsonic Ultra Green Aircraft Research Phase II: N+4 Advanced Concept Development,” CR- 2012-217556, NASA, Washington, DC, 2012.
- [6] Schäfer, A. W., Evans, A. D., Reynolds, T. G., and Dray, L., “Costs of mitigating CO2 emissions from passenger aircraft,” *Nature Climate Change*, Nov. 2015.
- [7] Prandtl, L., “Induced Drag of Multiplanes,” TN- 182, NACA, Washington, DC, 1924.
- [8] Dal Canto, D., Frediani, A., Ghiringhelli, G. L., and Terraneo, M., “The Lifting System of a PrandtlPlane, Part 1: Design and Analysis of a Light Alloy Structural Solution,” *Variational Analysis and Aerospace Engineering: Mathematical Challenges for Aerospace Design*, edited by G. Buttazzo and A. Frediani, No. 66 in Optimization and Its Applications, Springer, 2012.
- [9] Lange, R. H., Cahill, J. F., Bradley, E. S., Eudaily, R. R., Jenness, C. M., and MacWilkinson, D. G., “Feasibility Study of the Transonic Bi-

-
- plane Concept for Transport Aircraft Application,” CR- 132462, NASA, Washington, DC, 1974.
- [10] McMasters, J. H. and Kroo, I. M., “Advanced configurations for very large transport airplanes,” *Aircraft Design*, Vol. 1, No. 4, 1998, pp. 217–242.
- [11] Jones, R. T., “Theory of Wing-Body Drag at Supersonic Speeds,” TR 1284, NACA, Washington, DC, 1956.
- [12] Liebeck, R. H., “Design of the Blended Wing Body Subsonic Transport,” *Journal of Aircraft*, Vol. 41, No. 1, 2004, pp. 10–25.
- [13] Gur, O., Mason, W. H., and Schetz, J. A., “Full-Configuration Drag Estimation,” *Journal of Aircraft*, Vol. 47, No. 4, 2010, pp. 1356–1367.
- [14] Gern, F., Ko, A., Grossman, B., Haftka, R., Kapania, R. K., and Mason, W. H., “Transport Weight Reduction through MDO: The Strut-Braced Wing Transonic Transport,” *35th AIAA Fluid Dynamics Conference and Exhibit*, 2005-4667, AIAA, Toronto, ON, Canada, June 2005.
- [15] Federal Aviation Administration, “Airport Design,” Advisory Circular AC 150/5300-13A, U.S. Department of Transportation, Washington, DC, 2014.
- [16] Kroo, I., “Nonplanar Wing Concepts for Increased Aircraft Efficiency,” *Innovative Configurations and Advanced Concepts for Future Civil Aircraft*, VKI Lecture Series, June 2005.
- [17] Jansen, P. W. and Perez, R. E., “Effect of Size and Mission Requirements on the Design Optimization of Non-Planar Aircraft Configurations,” *13th AIAA/ISSMO Multidisciplinary Analysis Optimization Conference*, 2010-9188, AIAA, Fort Worth, TX, 2010.
- [18] Nangia, R. K., Palmer, M. E., and Tilmann, C. P., “Unconventional high aspect ratio joined-wing aircraft with aft- & forward-swept wing-tips,” *41st AIAA Aerospace Sciences Meeting and Exhibit*, 2003-0605, AIAA, Reno, NV, Jan. 2003.
- [19] Fullerton, J. D., “Notes on the Phillips Flying Machine,” *The Aeronautical Journal*, July 1908, pp. 55–59.
- [20] von Kármán, T. and Burgers, J. M., *General Aerodynamic Theory - Perfect Fluids*, Vol. II of *Aerodynamic Theory*, Dover, New York, NY, 1963.
- [21] Frediani, A., “The Prandtl Wing,” *Innovative Configurations and Advanced Concepts for Future Civil Transport Aircraft*, VKI Lecture Series, June 2005.

-
- [22] Schiktanz, D. and Scholz, D., “The Conflict of Aerodynamic Efficiency and Static Longitudinal Stability of Box Wing Aircraft,” *3rd CEAS Air & Space Conference*, Venice, Italy, 2011, pp. 910–921.
- [23] Demasi, L., “Investigation on the Conditions of Minimum Induced Drag of Closed Wing Systems and C-Wings,” *Journal of Aircraft*, Vol. 44, No. 1, 2007, pp. 81–99.
- [24] Munk, M. M., “General Biplane Theory,” Report 151, NACA, Washington, DC, 1923.
- [25] Gall, P. D. and Smith, H. C., “Aerodynamic Characteristics of Biplanes with Winglets,” *Journal of Aircraft*, Vol. 24, No. 8, 1987, pp. 518–522.
- [26] Wolkovitch, J., U.S. Patent No. 4365773, Dec. 1982.
- [27] Miranda, L. R., U.S. Patent No. 3834654, Sept. 1974.
- [28] Kroo, I., Gallman, J., and Smith, S., “Aerodynamic and Structural Studies of Joined-Wing Aircraft,” *Journal of Aircraft*, Vol. 28, No. 1, 1991, pp. 74–81.
- [29] Cahill, F. J. and Stead, D. H., “Preliminary Investigation at Subsonic and Transonic Speeds of the Aerodynamic Characteristics of a Biplane Composed of Sweptback and Sweptforward Wing Joined at the Tips.” RM L53L24b, NACA, Washington, DC, 1954.
- [30] Wolkovitch, J., “The Joined Wing: An Overview,” *Journal of Aircraft*, Vol. 23, No. 3, 1986, pp. 161–178.
- [31] Henderson, W. P. and Huffman, J. K., “Aerodynamic Characteristics of a Tandem Wing Configuration at Mach Number of 0.3,” TM X-72779, NASA, Washington, DC, 1975.
- [32] Frediani, A., Lombardi, G., Chiarelli, M., Longhi, A., Alessandro, M. D., and Bernardini, G., “Proposal for a New Large Airliner with a Non-Conventional Configuration,” *Proceedings of the XIV AIDAA Congress*, Naples, Italy, 1996.
- [33] Bernardini, G., Frediani, A., and Morino, L., “Aerodynamics for MDO of an Innovative Configuration,” *Aerodynamic design and optimization of flight vehicles in a concurrent multi-disciplinary environment*, ADA388284, NATO, Ottawa, ON, Oct. 1999.
- [34] Frediani, A., Balis Crema, L., Chiocchia, G., Ghiringhelli, G. L., and Morino, L., “Development of an Innovative Configuration for Transport Aircraft; a Project of Five Italian Universities,” *XVII Congresso Nazionale AIDAA III*, AIDAA, Rome, Italy, 2003, pp. 2089–2104.

-
- [35] Divoux, N. and Frediani, A., “The Lifting System of a Prandtl-Plane, Part 2: Preliminary Study on Flutter Characteristics,” *Variational Analysis and Aerospace Engineering: Mathematical Challenges for Aerospace Design*, edited by G. Buttazzo and A. Frediani, No. 66 in Optimization and Its Applications, Springer, 2012.
- [36] Gagnon, H. and Zingg, D., “Aerodynamic Optimization Trade Study of a Box-Wing Aircraft Configuration,” *56th AIAA/ASCE/AHS/ASC Structures, Structural Dynamics, and Materials Conference*, 2015-0695, AIAA, Kissimmee, FL, Jan. 2015.
- [37] Rhodes, M. D. and Selberg, B. P., “Dual Wing, Swept Forward Swept Rearward Wing and Single Wing Design Optimization for High Performance Business Airplanes,” ICAS-82-1.4.2, 1982, pp. 496–511.
- [38] Crowe, J. H., “Tandem-Wing Aeroplanes: An Examination of the Characteristics of this Type of Wing Arrangement,” *Aircraft Engineering and Aerospace Technology*, Vol. 7, No. 10, 1935, pp. 243–248.
- [39] Hartshorn, A. S., “Tests of the Pou-du-Ciel in the 24 ft. tunnel of the Royal Aircraft Establishment,” Tech. Rep. B. A. 1333, Royal Aircraft Establishment, Farnborough, Hampshire, Sept. 1935.
- [40] Wolkovitch, J., “Application of the Joined Wing to Cruise Missiles.” Tech. Rep. ONR-CR212-266-1, US Department of the Navy, Office of Naval Research, Arlington, VA, Nov. 1980.
- [41] Caja, R. and Scholz, D., “Box Wing Flight Dynamics in the Stage of Conceptual Aircraft Design,” Deutscher Luft- und Raumfahrtkongress 281383, 2012.
- [42] van Ginneken, D. A. J., Voskuijl, M., van Tooren, M. J. L., and Frediani, A., “Automated Control Surface Design and Sizing for the Prandtl Plane,” *51st AIAA/ASME/ASCE/AHS/ASC Structures, Structural Dynamics, and Materials Conference*, 2010-3060, AIAA, Orlando, FL, April 2010.
- [43] Frediani, A., Rizzo, E., Cipolla, V., Chiavacci, L., Bottoni, C., Scanu, J., and Iezzi, G., “Development of ULM Prandtlplane Aircraft and Flight Tests on Scaled Models,” *XIX Congresso Nazionale AIDAA*, AIDAA, Forli, Italy, Sept. 2007.
- [44] Samuels, M. F., “Structural Weight Comparison of a Joined Wing and a Conventional Wing,” *Journal of Aircraft*, Vol. 19, No. 6, 1982, pp. 485–491.

-
- [45] Smith, S. C. and Stonum, R. K., “Experimental Aerodynamic Characteristics of a Joined-Wing Research Aircraft Configuration,” TM-101083, NASA, 1989.
- [46] Hajela, P. and Chen, J. L., “Preliminary Weight Estimation of Conventional and Joined Wings Using Equivalent Beam Models,” *Journal of Aircraft*, Vol. 25, No. 6, 1988, pp. 574–576.
- [47] Cronin, D. L. and Somnay, R. J., “Estimating the Weight of Generally Configured Dual Wing Systems,” *26th Structures, Structural Dynamics, and Materials Conference*, 85-0641, AIAA, Orlando, FL, 1985, pp. 173–177.
- [48] Gallman, J. W., Smith, S. C., and Kroo, I. M., “Optimization of Joined-Wing Aircraft,” *Journal of Aircraft*, Vol. 30, No. 6, 1993, pp. 897–905.
- [49] Jansen, P. W., Perez, R. E., and Martins, J. R. R. A., “Aerostructural Optimization of Nonplanar Lifting Surfaces,” *Journal of Aircraft*, Vol. 47, No. 5, September-October 2010, pp. 1490–1503.
- [50] Jemitola, P. O., Fielding, J., and Stocking, P., “Joint fixity effect on structural design of a box wing aircraft,” *The Aeronautical Journal*, Vol. 116, No. 1178, 2012, pp. 363–372.
- [51] Jemitola, P. O., Monterzino, G., Fielding, J., and Lawson, C., “Tip fin inclination effect on structural design of a box-wing aircraft,” *Proceedings of the Institution of Mechanical Engineers Part G: Journal of Aerospace Engineering*, Vol. 227, No. 1, 2013, pp. 175–184.
- [52] Jemitola, P. O., Monterzino, G., and Fielding, J., “Wing mass estimation algorithm for medium range box wing aircraft,” *The Aeronautical Journal*, Vol. 117, No. 1189, 2013, pp. 329–340.
- [53] Demasi, L., Cavallaro, R., and Márquez Razón, A., “Postcritical Analysis of PrandtlPlane Joined-Wing Configurations,” *AIAA Journal*, Vol. 51, No. 1, 2013, pp. 161–177.
- [54] Cuerno-Rejado, C., Alonso-Albir, L., and Gehse, P., “Conceptual design of a medium-sized joined-wing aircraft,” *Proceedings of the Institution of Mechanical Engineers Part G: Journal of Aerospace Engineering*, Vol. 224, 2010, pp. 681–696.
- [55] Ramussen, C. C., Canfield, R. A., and Blair, M., “Joined-Wing Sensor-Craft Configuration Design,” *Journal of Aircraft*, Vol. 43, No. 5, 2006, pp. 1470–1478.
- [56] Sun, W.-C., Broichhausen, K., and Seifert, J., “Promising Future Aircraft Concept - ESTOL,” *26th International Congress of the Aeronautical Sciences*, ICAS 2008-509, Anchorage, AK, Sept. 2008.

-
- [57] Wolkovitch, J., “Subsonic VSTOL Aircraft Configurations with Tandem Wings,” *Journal of Aircraft*, Vol. 16, No. 9, 1979, pp. 605–611.
- [58] Phillips, W. F., *Mechanics of Flight*, John Wiley & Sons, Hoboken, NJ, 1st ed., 2004.
- [59] McGeer, T. and Kroo, I. M., “A Fundamental Comparison of Canard and Conventional Configurations,” *Journal of Aircraft*, Vol. 20, No. 11, 1983, pp. 983–992.
- [60] Roskam, J., *Preliminary Calculation of Aerodynamic, Thrust and Power Characteristics*, Vol. 6 of *Airplane Design*, DAR Corporation, Lawrence, KS, 2008.
- [61] Phillips, W. F. and Snyder, D. O., “Modern Adaptation of Prandtl’s Classic Lifting-Line Theory,” *Journal of Aircraft*, Vol. 37, No. 4, 2000, pp. 662–670.
- [62] Abbott, I. H. and von Doenhoff, A. E., *Theory of Wing Sections*, Dover Publications Inc, New York, NY, 2nd ed., 1959.
- [63] Goodrich, K. H., Sliwa, S. M., and Lallman, F. J., “A Closed-Form Trim Solution Yielding Minimum Trim Drag for Airplanes with Multiple Longitudinal-Control Effectors,” TP 2907, NASA, Washington, DC, 1989.
- [64] Jackson, P., editor, *All the World’s Aircraft*, Jane’s Information Group Ltd., Surrey, UK, 2004.
- [65] Roskam, J., *Component Weight Estimation*, Vol. 5 of *Airplane Design*, DAR Corporation, Lawrence, KS, 2003.
- [66] Engineering Sciences Data Unit, “VGK Method for Two-Dimensional Aerofoil Sections Part 1: Principles and Results,” ESDU 96028, 1996.
- [67] Raymer, D. P., *Aircraft Design: A Conceptual Approach*, AIAA Education Series, AIAA, Washington. DC, 1992.
- [68] Murray, G. P. and Saunders, M., “SNOPT: An SQP Algorithm for Large-Scale Constraint Optimization,” *SIAM Journal on Optimization*, Vol. 12, No. 4, 2002, pp. 979–1006.
- [69] Perez, R. E., Jansen, P. W., and Martins, J. R. R. A., “pyOpt: A Python-Based Object-Oriented Framework for Nonlinear Constrained Optimization,” *Structures and Multidisciplinary Optimization*, Vol. 45, No. 1, 2012, pp. 101–118.
- [70] Jansen, P. W., *Robust Coupled Optimization of Aircraft Family Design and Fleet Allocation for Multiple Markets*, Ph.D. thesis, Royal Military College of Canada, Kingston, ON, March 2015.

-
- [71] Howe, D., “The Prediction of Aircraft Wing Mass,” *Proceedings of the Institution of Mechanical Engineers Part G: Journal of Aerospace Engineering*, Vol. 210, No. 2, 1996, pp. 135–145.
- [72] Elham, A., Rocca, G. L., and van Tooren, M. J. L., “Development and implementation of an advanced, design-sensitive method for wing weight estimation,” *Aerospace Science and Technology*, Vol. 29, 2013, pp. 100–113.
- [73] Torenbeek, E., “Development and Application of a Comprehensive, Design-sensitive Weight Prediction Method for Wing Structures of Transport Category Aircraft,” LR 693, TU Delft, 1992.
- [74] Ardema, M. D., Chambers, M. C., Patron, A. P., Hahn, A. S., Miura, H., and Moore, M. D., “Analytical Fuselage and Wing Weight Estimation of Transport Aircraft,” TM 110392, NASA, Washington, DC, 1996.
- [75] Liu, W. and Anemaat, W. A. J., “A Refined Method for Wing Weight Estimation and A New Method for Wing Center of Gravity Estimation,” *Aviation Technology Integration and Operation Conference*, 2013-4371, AIAA, Los Angeles, CA, 2013.
- [76] Petermeier, J., Radtke, G., Stohr, M., Woodland, A., Takahashi, T. T., Donovan, S., and Shubert, M., “Enhanced Conceptual Wing Weight Estimation Through Structural Optimization and Simulation,” *13th AIAA/ISSMO Multidisciplinary Analysis Optimization Conference*, 2010-9075, AIAA, Fort Worth, TX, Sept. 2010.
- [77] Liem, R. P., Mander, C. A., Lee, E., and Martins, J. R. R. A., “Aerostructural design optimization of a 100-passenger regional jet with surrogate-based mission analysis,” *Aviation Technology, Integration and Operations Conference*, 2013-4372, AIAA, Los Angeles, CA, 2013.
- [78] Gern, F. H., Naghshineh-Pour, A. H., Sulaeman, E., Kapania, R. K., and Haftka, R. T., “Structural Wing Sizing for Multidisciplinary Design Optimization of a Strut-Braced Wing,” *Journal of Aircraft*, Vol. 38, No. 1, 2001, pp. 154–163.
- [79] Ajaj, R. M., Friswell, M. I., Smith, D., and Isikveren, A. T., “A conceptual wing-box weight estimation model for transport aircraft,” *The Aeronautical Journal*, Vol. 177, No. 1191, 2013, pp. 533–551.
- [80] Gur, O., Bhatia, M., Mason, W. H., Schetz, J. A., Kapania, R. K., and Nam, T., “Development of Framework for Truss-Braced Wing Conceptual MDO,” *51st AIAA/ASME/ASCE/AHS/ASC Structures, Structural Dynamics, and Materials Conference*, Vol. 2010-2754, AIAA, Orlando, FL, April 2010.

-
- [81] Gallman, J. W. and Kroo, I. M., “Structural Optimization for Joined-Wing Synthesis,” *Journal of Aircraft*, Vol. 33, No. 1, 1996, pp. 214–233.
- [82] Perez, R. E. and Martins, J. R. R. A., “pyACDT: An Object-Oriented Framework for Aircraft Design Modelling and Multidisciplinary Optimization,” *12th AIAA/ISSMO Multidisciplinary Analysis and Optimization Conference*, Vol. AIAA 2008-5955, Victoria, BC, Canada, 2008.
- [83] Megson, T., *Aircraft Structures for Engineering Students*, Butterworth-Heinemann, Burlington, MA, 4th ed., 2007.
- [84] Beltramo, M. N., Trapp, D. L., Kimoto, B. W., and Marsh, D. P., “Parametric Study of Transport Aircraft Cost and Weight,” CR 151970, NASA, Washington, DC, 1977.
- [85] Taylor, J. W. R., editor, *All the World’s Aircraft*, Jane’s Yearbooks, London, England, 1973.
- [86] Taylor, J. W. R., editor, *All The World’s Aircraft*, Jane’s Yearbooks, Buckinghamshire, England, 1966.
- [87] Taylor, J. W. R., editor, *All the World’s Aircraft*, Jane’s Information Group Ltd., Surrey, UK, 1989.
- [88] Takahashi, T. T. and Lemonds, T., “Prediction of Wing Structural Mass for Transport Category Aircraft Conceptual Design,” *15th AIAA Aviation Technology, Integration, and Operations Conference*, 2015-3374, AIAA, Dallas TX, June 2015.
- [89] Cramer, E. J., jr. Dennis, J. E., Frank, P. D., Lewis, R. M., and Shubin, G., “Problem Formulation for Multidisciplinary Optimization,” *SIAM Journal on Optimization*, Vol. 4, No. 4, 1994, pp. 754–776.
- [90] Roskam, J., *Preliminary Sizing of Airplanes*, Vol. 1 of *Airplane Design*, DAR Corporation, Lawrence, KS, 2005.
- [91] U. S. National Archives and Records Administration, “Aeronautics and Space,” Title 14, Code of Federal Regulations, 2016.
- [92] Katz, J. and Plotkin, A., *Low Speed Aerodynamics*, McGraw-Hill, Singapore, 1st ed., 1991.
- [93] Nelson, C., R., *Flight Stability and Automatic Control*, Aerospace Science and Technology Series, McGraw-Hill, Boston, MA, 2nd ed., 1998.
- [94] Engineering Sciences Data Unit, “VGK Method for Two-Dimensional Airfoil Sections. Part 2: Estimation of a Separation Boundary in Transonic Flow,” ESDU 97030, 1998.

-
- [95] Math à la Carte, “Multi-Dimensional Table Look Up, Interpolation, and Differentiation,” Library 12.2, July 2015.
- [96] Powers, S. A., “Critical Field Length Calculations for Preliminary Design,” *AIAA Journal of Aircraft*, Vol. 18, No. 2, 1981, pp. 103–107.
- [97] Bartel, M. and Young, T. M., “Simplified Thrust and Fuel Consumption Models for Modern Two-Shaft Turbofan Engines,” *AIAA Journal of Aircraft*, Vol. 45, No. 4, 2008, pp. 1450 – 1456.
- [98] Chai, S., Crisafuli, P., and Mason, W. H., “Aircraft Center of Gravity Estimation in Conceptual Design,” *Aircraft Engineering, Technology, and Operations Congress*, 95-3882, AIAA, Los Angeles, CA, Sept. 1995.
- [99] Oman, B. H., “Vehicle Design Evaluation Program,” CR 145070, NASA, Washington, DC, 1977.
- [100] McCullers, L. A., “Aircraft Configuration Optimization Including Optimized Flight Profiles,” *Symposium on Recent Experiences in Multidisciplinary Analysis and Optimization*, edited by J. Sobieski, NASA, Hampton, VA, 1984.
- [101] Perez, R. E., *A multidisciplinary optimization framework for flight dynamics and control integration in aircraft design*, Ph.d. thesis, University of Toronto, Toronto, ON, Canada, 2007.
- [102] Roskam, J., *Determination of Stability, Control and Performance Characteristics: FAR and Military Requirements*, Vol. 7 of *Airplane Design*, DAR Corporation, Lawrence, KS, 2006.
- [103] Currey, S., N., *Aircraft Landing Gear Design: Principles and Practices*, AIAA Education Series, AIAA, Washington, DC, 1988.
- [104] Gedeon, C. and Takahashi, T. T., “Multi-Disciplinary Survey of Engine Parameters and its Impact on Performance and Energy Maneuverability,” *14th AIAA Aviation Technology, Integration, and Operations Conference*, 2014-2032, AIAA, Atlanta, GA, June 2014.
- [105] Wolkovitch, J., “Joined-Wing Research Airplane Feasibility Study,” *Aircraft Design Systems and Operations Meeting*, 84-2471, AIAA, San Diego, CA, 1984.
- [106] Morgan, H. J. and Paulson, J. W., “Low-Speed Aerodynamic Performance of a High-Aspect-Ratio Supercritical-Wing Transport Model Equipped With Full-Span Slat and Part-Span Double-Slotted Flaps,” TP 1580, NASA, Washington, DC, 1979.

- [107] Kjelgaard, S. O. and Paulson, J. W., "Effect of Sweep and Aspect Ratio on the Longitudinal Aerodynamics of a Spanloader Wing In- and Out-of-Ground Effect," TM 80199, NASA, Washington, DC, 1981.

Appendices

A Model Validation Cases

Three main aerodynamic models were used in this thesis: an analytic model of aircraft stability, a vortex panel aerodynamic model and an aerofoil section properties model. The ability of these three models to predict the aerodynamic forces, moments and derivatives of various aircraft configurations will be investigated in the following sections. Section A.1 examines the analytic stability model, Section A.2, the vortex panel model, and Section A.3 the aerofoil property model. Section A.4 validated the performance of the aircraft weight prediction model.

A.1 Analytic model verification

The analytic model presented in Chapter 3 was derived from the stability model of Phillips [58]. To ensure that the new analytic stability model was properly formulated, the results from the analytic model of Chapter 3 were compared to the results obtained by Phillips[58]. Two cases were considered, a conventional wing and horizontal tail aircraft and a canard aircraft.

Both aircraft configurations were tested over a range of cruise airspeeds and the angle of incidence and elevator deflection required for trimmed steady flight were calculated. Results from the conventional aircraft are shown in Figure A.1a and show very close agreement to the Phillips model. The static margin of the conventional aircraft was computed as 11.4% which is within 5% of the static margin of 12% given by Phillips. The results from modelling the canard aircraft, however, did not agree with the results from Phillips. The trends in angle of attack and elevator deflection, Figure A.1b, were not in agreement and the static margin of the modelled canard aircraft was negative while Phillips predicted a positive static margin of 5%. The analytic model of Chapter 3 accounted for the destabilizing effect of the canard's downwash reducing the lift of the stabilizing main wing while the model of Phillips did not. To make a fair comparison between the analytic model and Phillips' results, the centre of gravity of the canard aircraft was moved forward until the static

margin was equal in both models. These results are shown in Figure A.1c, where two canard aircraft with the same static margin are compared. The analytic model shows much better agreement with Phillips when the static margin of both aircraft were matched.

The analytic model developed in Chapter 3 showed similar trends to the model developed by Phillips, when the assumptions of the Phillips model were met. Specifically, that the normalwash of the control surface had a negligible effect on the aircraft's stability. However, when this was not the case, *i.e.* for a canard aircraft, the analytic model was able to predict the destabilizing influence of the control surface. This showed that the new analytic model was able to predict the static longitudinal stability of aircraft designs with two main lifting surfaces providing stability, where the influence of each wing's normalwash on the other was significant.

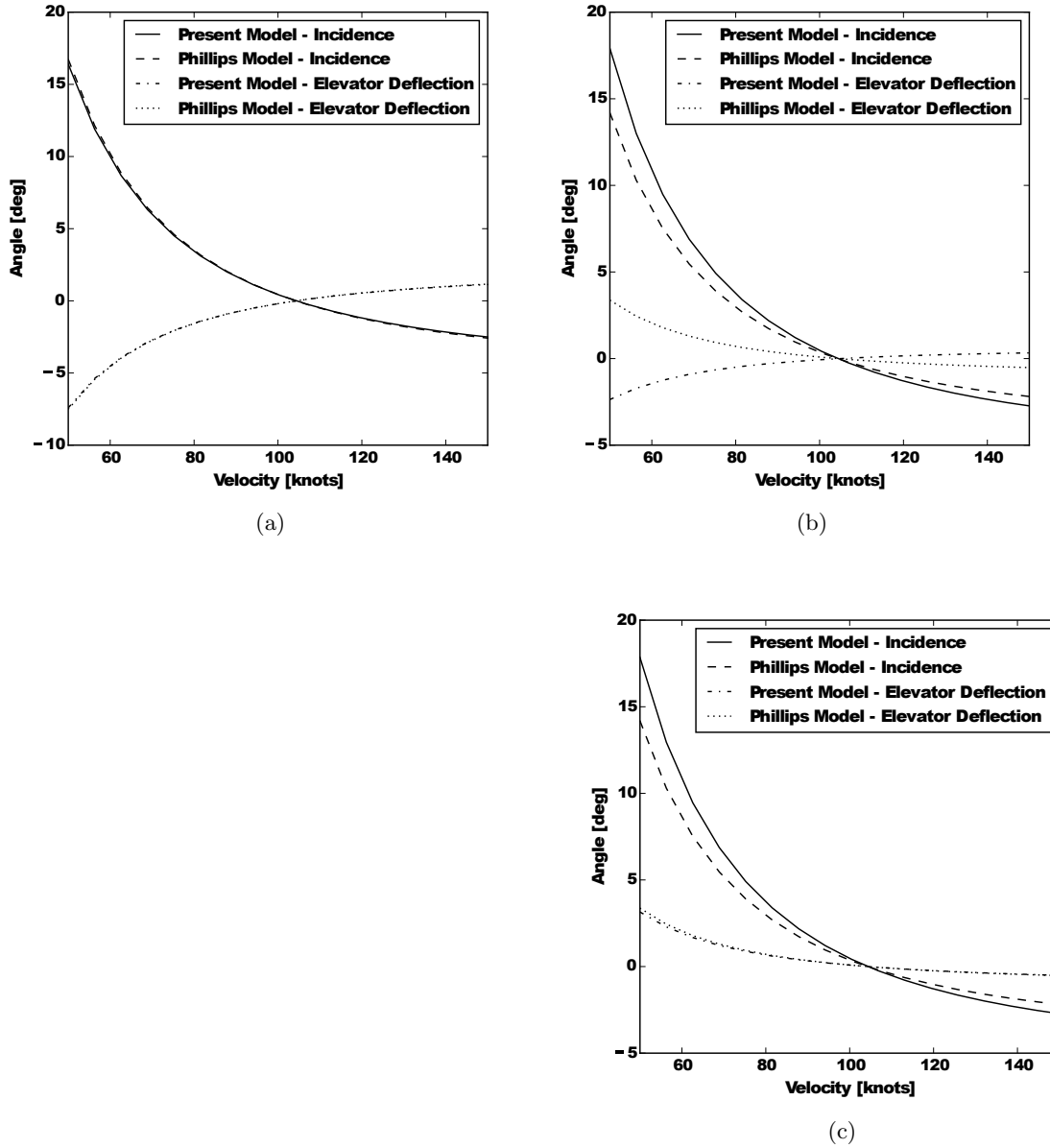


Figure A.1: Comparison of the current analytical aircraft stability model to the model of Phillips [58] for two aircraft configurations at sea level conditions. For both aircraft, total planform area was 216 ft^2 and weight was 2700 lb_f . (a) Conventional configuration using the nominal c.g. position, 11.4% static margin. (b) Canard configuration using the nominal c.g. position, -4.2% static margin. (c) Canard configuration with forward c.g. shift, 5.0% static margin.

A.2 Aerodynamic model validation

The vortex panel aerodynamic model, `pyVORLIN`, was used in the analyses discussed in Chapters 4 through 7 to predict the aerodynamic forces, moments and derivatives of conventional and box-wing aircraft in both cruise and takeoff configurations. Wind tunnel data from previous experiments were used to validate the aerodynamic model for a range of aircraft designs.

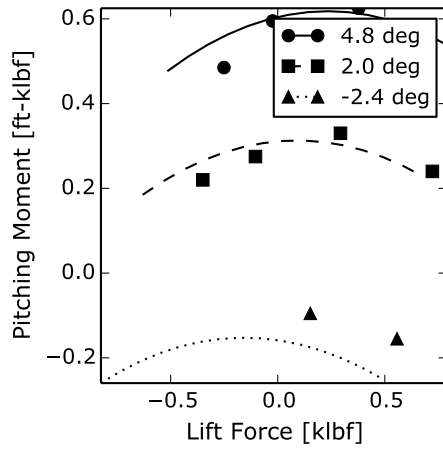
A.2.1 Mignet *pou-du-ciel*

The *pou-du-ciel* was a small general aviation aircraft with a dual-wing design. This aircraft attempted to achieve static longitudinal stability and control through two main wings, with the incidence of the entire first wing adjustable by the pilot's pitch control. The full scale aircraft, with a span of 19 ft was tested in the Royal Aircraft Establishment 24 ft wind tunnel at an airspeed of 100 ft/s. As the experimental data in Figure A.2 show, the aircraft was neither stable nor controllable when the centre of gravity moved aft to 60% of the fore wing chord. The pitch stiffness of the aircraft was positive. Even with maximum pitch up input, the aircraft could not generate a positive pitching moment if the wings generated negative lift forces, which could occur when the aircraft was descending.

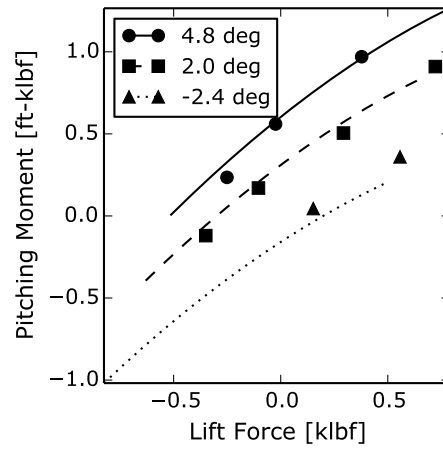
The predictions made with `pyVORLIN` agree well with the experimental data. The slope of the pitching moment curve was predicted properly, as was the effect of changing the fore wing incidence to adjust the pitching moment of the aircraft. These results show the ability of `pyVORLIN` to predict the static longitudinal stability and trim of aircraft designs using tandem wings to achieve stability. The *pou-du-ciel* was a challenging case as the two wings had very little stagger so the stability and trim were highly dependent on normalwash generated by both wings.

A.2.2 NASA joined-wing research model

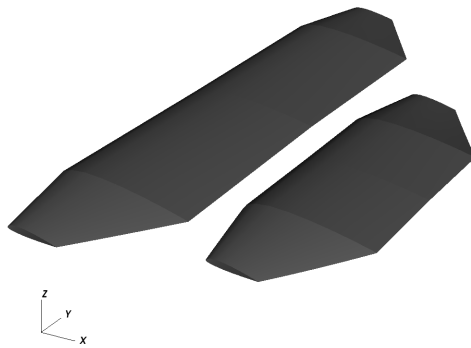
As part of an initial feasibility study for a joined-wing research aircraft, NASA performed a series of tests on three different joined-wing geometries. Two of these geometries are shown in Figure A.3. Both were based on the same fuselage, vertical tail and propulsion systems as the NASA AD-1 oblique wing research aircraft [105]. The JW1 configuration had the aft wing join the fore wing at 60% of the fore-wing span. The JW3 geometry was the same as the JW1 geometry but with the wing segments outboard of the aft-wing joint removed. The JW3 geometry had a smaller planform area than the JW1 but had the advantage of being in the most aerodynamically preferable joined-wing



(a) c.g. at 0.4c



(b) c.g. at 0.6c



(c)



(d)

Figure A.2: Pitching moment of the Mignet *pou-du-ciel*. Points represent experimental data, lines represent simulations. Figure (d) taken by the author.

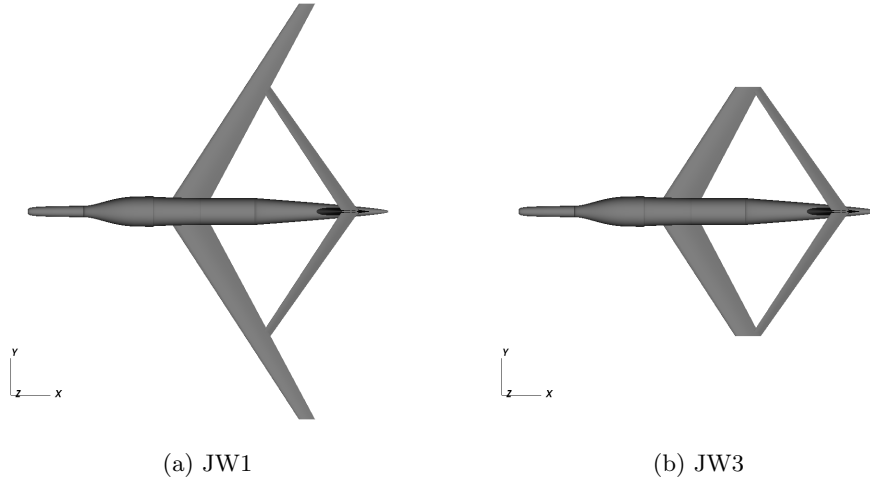


Figure A.3: NASA joined-wing research models

configuration, see Chapter 2. Tests were carried out at the NASA Ames 12 foot pressurised wind tunnel on a one-sixth scale model at a Mach number of 0.3 and Reynolds number, based on the model's mean aerodynamic chord of 1.0×10^6 [45].

Lift, drag and pitching moment data for the JW1, Figure A.4, and JW3, Figure A.5 were compared to the results of `pyVORLIN`. The `pyVORLIN` aerodynamic model predicted three important properties of the designs: the maximum lift coefficient, the pitch stiffness and the drag for attached flows. The maximum lift coefficient predicted by `pyVORLIN` is shown as a red square, this value was predicted to within $0.1 C_L$ which was acceptable accuracy given there was uncertainty associated with the maximum section lift coefficient of the custom aerofoil used in the joined-wing research model. The pitch stiffness of both the JW1 and JW3 aircraft showed good agreement with the experimental data, though there was a bias error between the experimental and computed results. Uncertainty in the exact moment centre of the experimental data and of the section properties of the custom aerofoils may have led to this error. Finally, the drag was predicted very accurately in the pre-stall regime. The `pyVORLIN` model accounted for neither the interference between the wing and the fuselage nor between the fore and aft wings at their junction. Neglecting these effects did lead to a notable bias in the drag results.

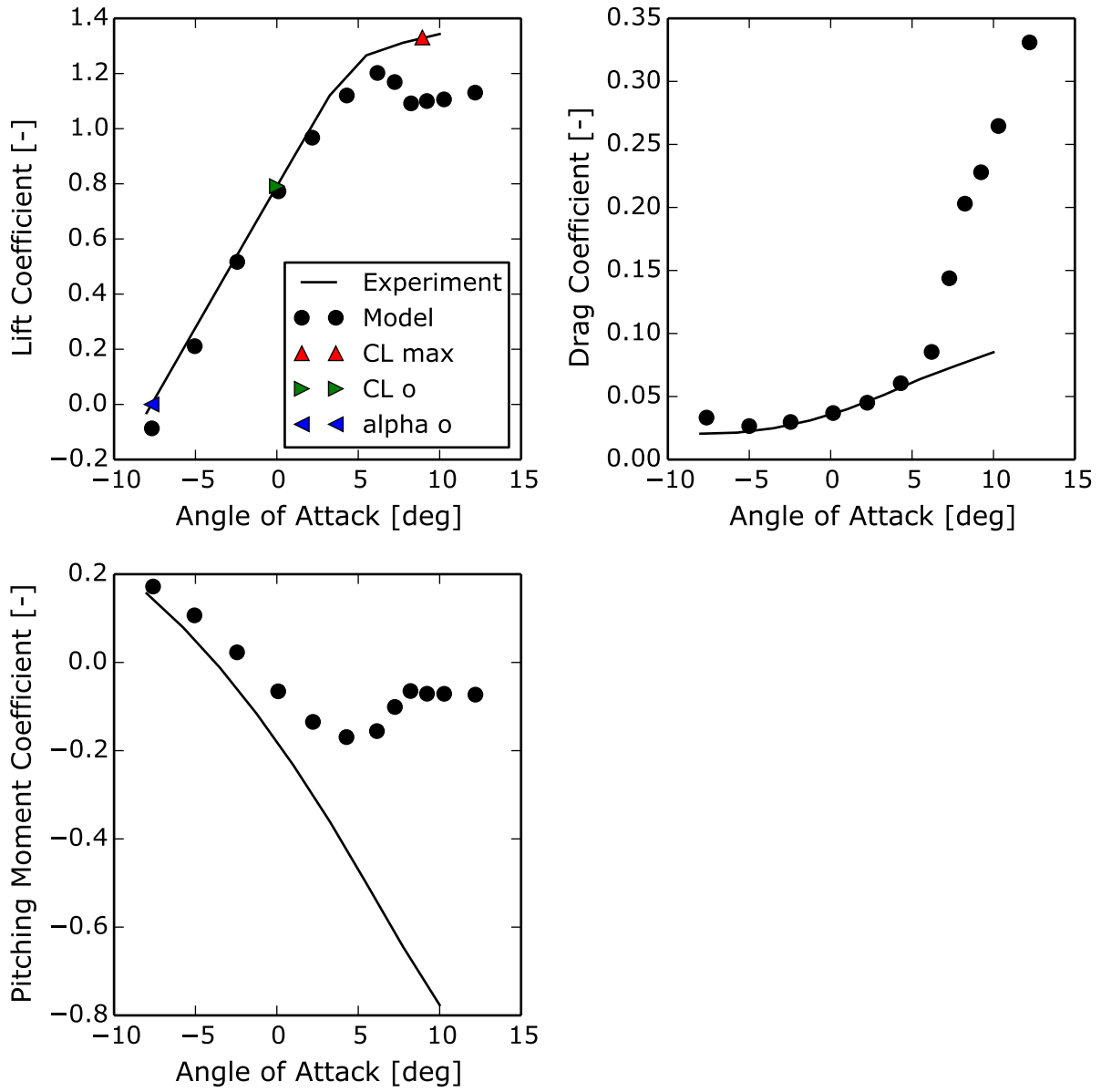


Figure A.4: NASA JW1 aerodynamic data

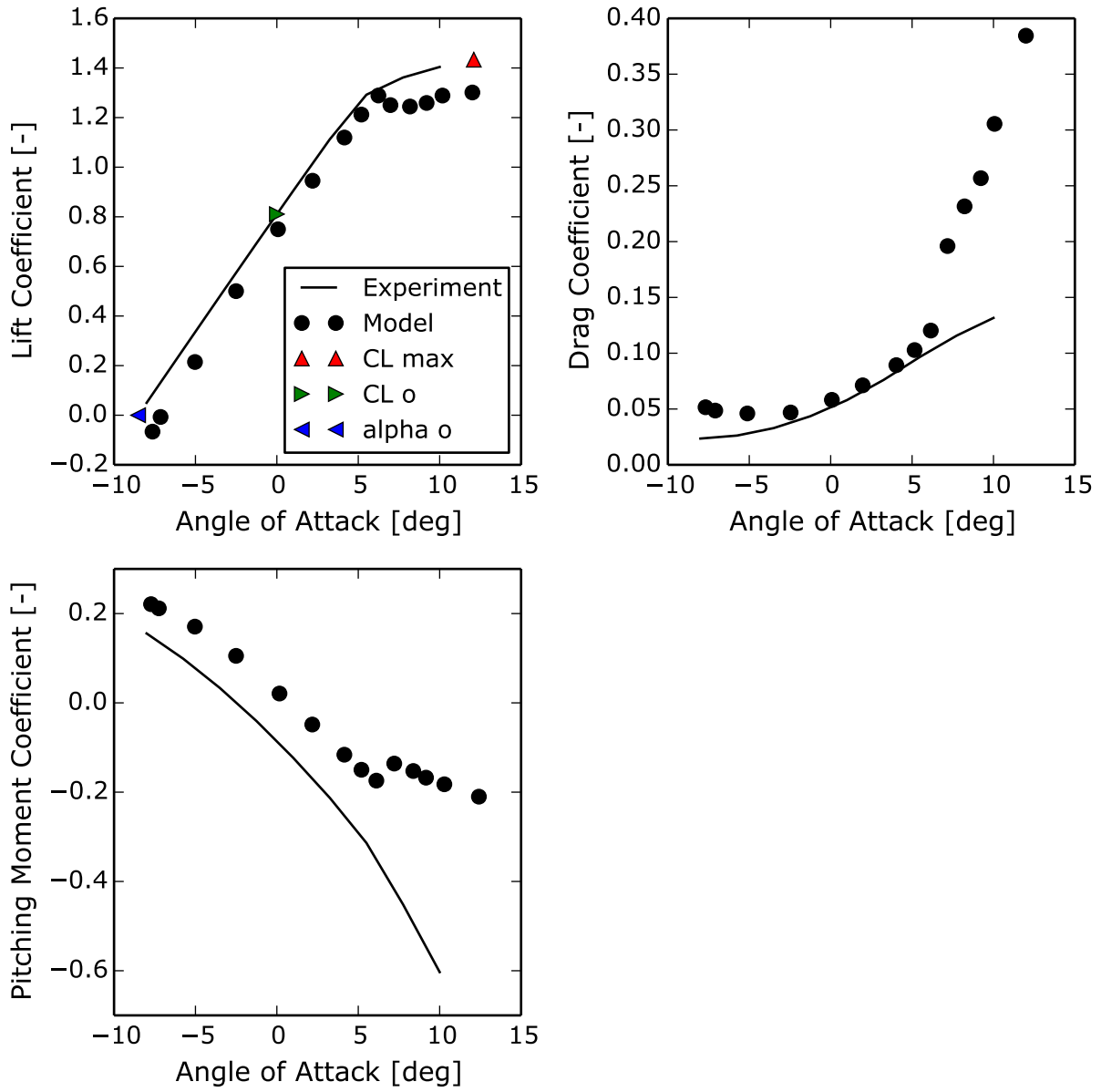


Figure A.5: NASA JW3 aerodynamic data

A.2.3 NASA supercritical-wing transport model

To investigate the ability of `pyVORLIN` to predict the performance of an aircraft with deployed high lift devices, `pyVORLIN` results were compared to data for the NASA Supercritical-wing transport model. Experimental data were obtained on a twin-engine wide-body civil transport model in both cruise and takeoff configurations. Tests were performed in the NASA Langley V/STOL wind tunnel on a large, 12 ft span model equipped with variable leading and trailing edge high lift devices. Tests were performed at a Mach number of 1.68 for cruise and 1.67 for takeoff and a Reynolds number based on mean aerodynamic chord of 1.35×10^6 for both configurations [106].

The geometry of the aircraft is shown in Figure A.6. The locations of leading and trailing edge high lift devices are shown as well as the locations of ailerons and spoilers, whose effects were not considered in this validation study.

The NASA supercritical wing transport aircraft used a complex leading edge slat and dual slotted trailing edge flap configuration. The exact magnitude of the changes to lift, drag, moment, and maximum lift coefficient of these devices could not be predicted exactly with the empirical methods used by `pyVORLIN` to model high lift devices [60]. More important than predicting the exact magnitude of the forces and moments was predicting the trends which occurred with the deployment of high lift devices.

The lift, drag and moment on the aircraft in cruise configuration are shown in Figure A.7. The results predicted by `pyVORLIN` were in good agreement with experiments, specifically, the lift at zero angle of attack, maximum lift coefficient, drag and pitch stiffness. With the leading edge slats and trailing edge flaps deployed, Figure A.8, `pyVORLIN` was not able to predict the trends in forces and moments as closely as at cruise. However, the results did show the correct sensitivity to high lift device deployment. The lift at zero angle of attack was increased significantly and agreed with experiments, as did the maximum lift coefficient. The pitch stiffness was predicted correctly, though there was a large bias in the pitching moment trends. The drag coefficient was also increased by the high lift devices but `pyVORLIN` under-predicted the magnitude of this increase.

Predicting the precise effects of high lift device deployment is a challenge for any aerodynamic solver and though `pyVORLIN` did not reproduce the experimental results exactly, it did predict several important parameters and the results showed the correct sensitivities to high lift devices.

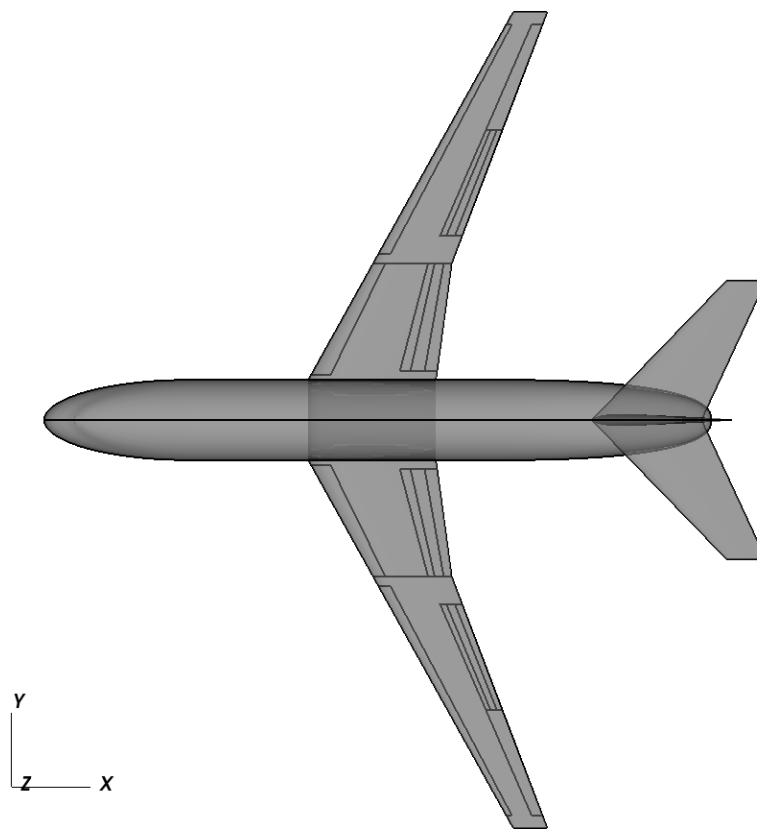
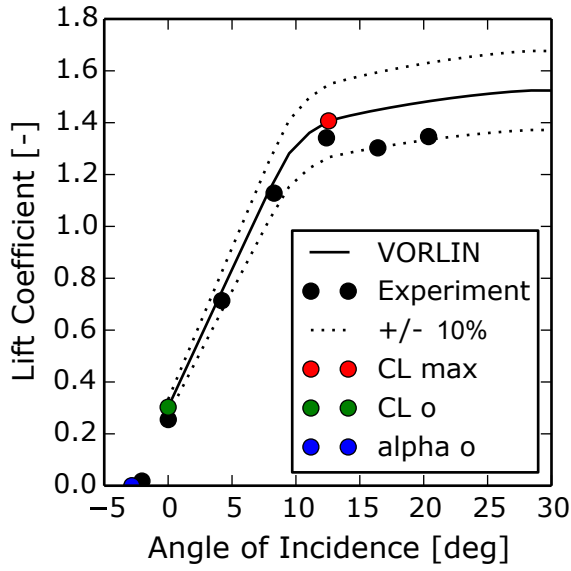
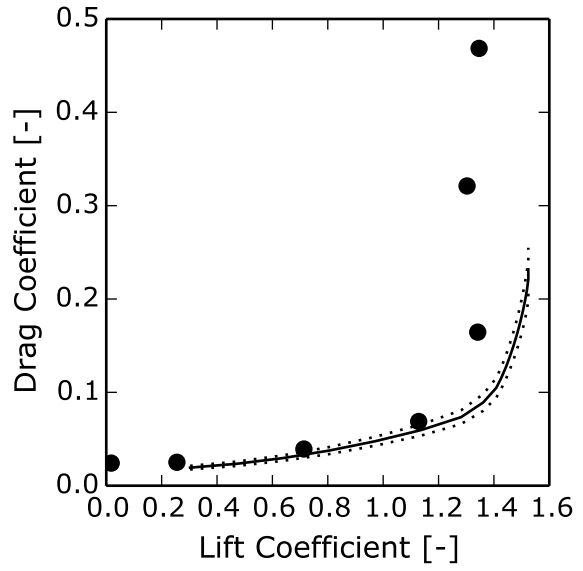


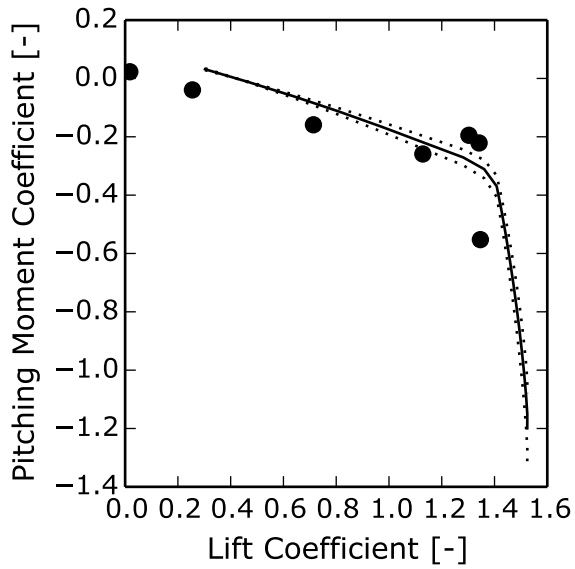
Figure A.6: NASA supercritical-wing transport research model.



(a) Lift Coefficient

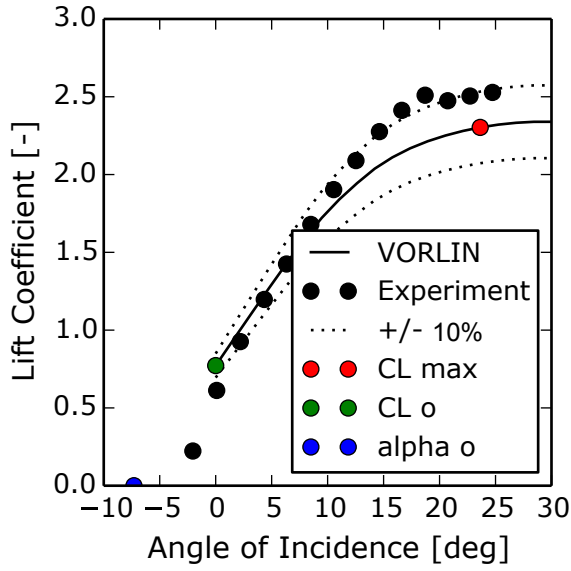


(b) Drag Coefficient

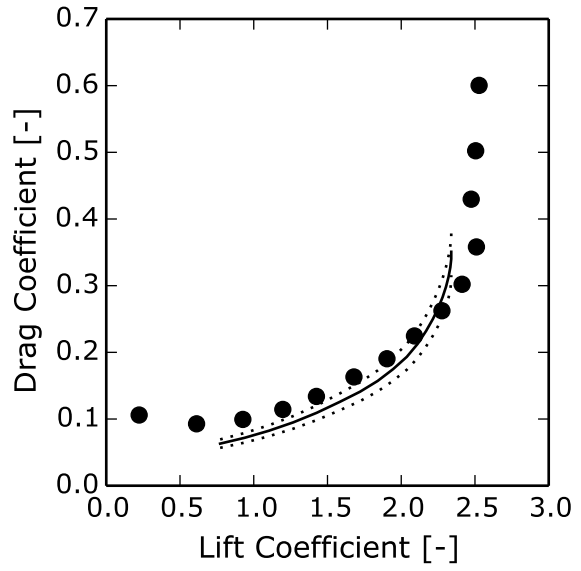


(c) Moment Coefficient

Figure A.7: NASA supercritical wing transport model, cruise aerodynamic data.



(a) Lift Coefficient



(b) Drag Coefficient



(c) Moment Coefficient

Figure A.8: NASA supercritical wing transport model, takeoff aerodynamic data.

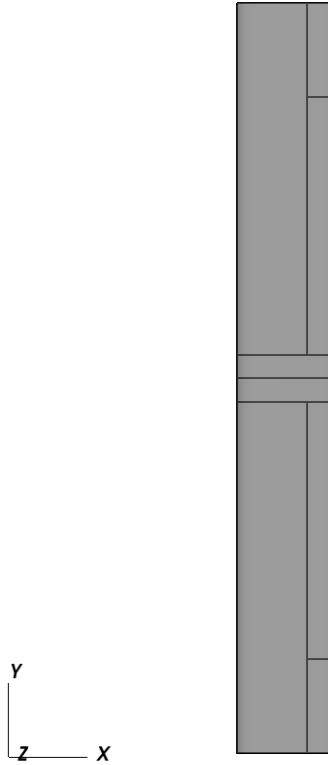


Figure A.9: NASA span-loader research model

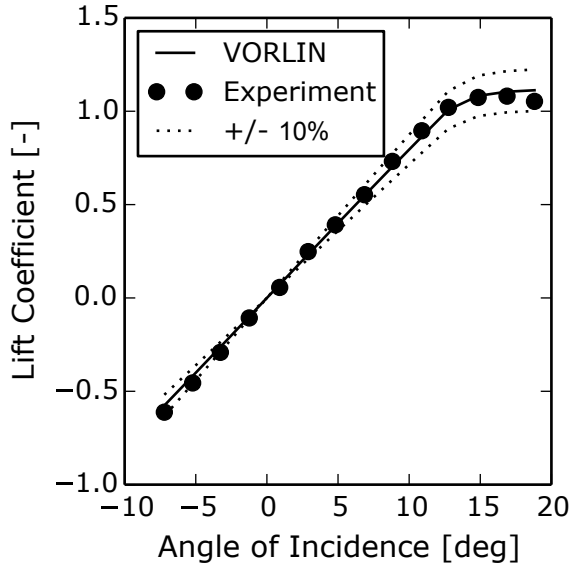
A.2.4 NASA span-loader aircraft in ground effect

Experimental data on the NASA span-loader aircraft were used to investigate the ability of `pyVORLIN` to predict the increase in lift generated by a wing in ground effect. This aircraft was designed as a high aspect ratio flying wing cargo transport, with the payload evenly distributed along the span to reduce the wing root bending moment. The geometry of the span-loader is shown in Figure A.9. The model was equipped with trailing edge flaps and ailerons. Tests were conducted on a 10 ft span model in the NASA Langley V/STOL tunnel at a Mach number of 0.14 and a Reynolds number of between 1.3×10^6 to 1.8×10^6 [107].

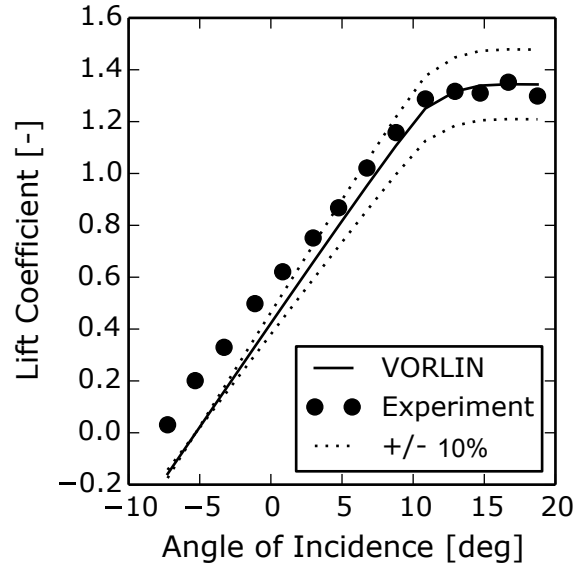
The NASA tests investigated the span-loader aircraft both in and out of

ground effect, with and without flaps deployed. When the model was out of the ground effect, `pyVORLIN` predicted the lift at a range of attached angles of attack and the maximum lift coefficient both with and without flaps. The span-loader aircraft used simple flap geometries whose performance was better predicted by the models used by `pyVORLIN` than the more complex flaps used in the NASA supercritical wing transport.

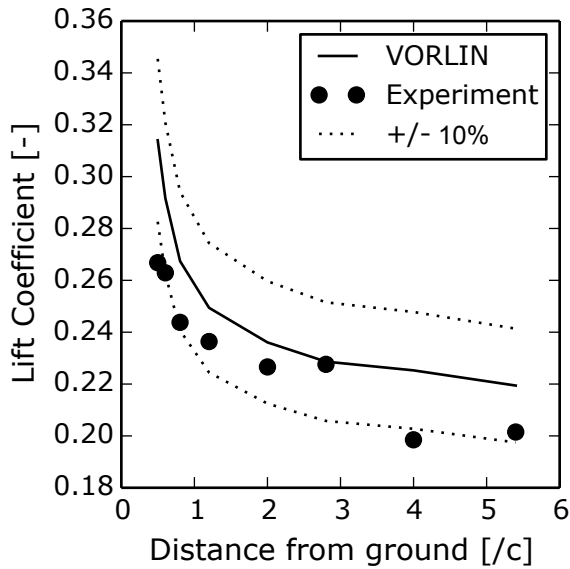
As the wing approached the ground, the lift generated by the wing increased continuously for the range of wing-to-ground distances considered. The `pyVORLIN` aerodynamic model predicted this increase in lift both with and without flaps deployed. These results show the ability of `pyVORLIN` to model wings in ground effect.



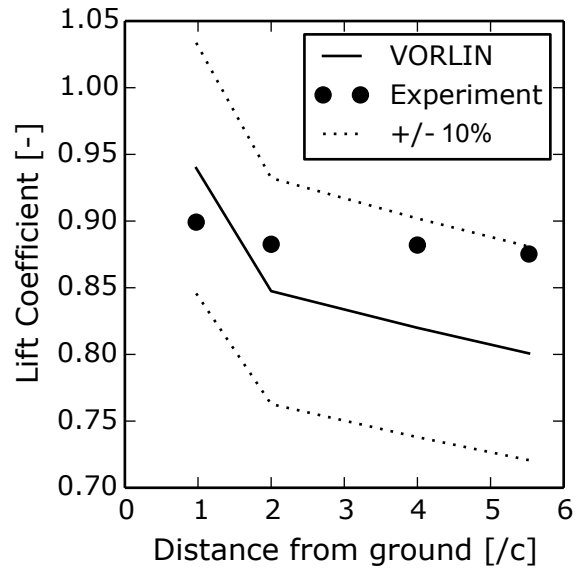
(a) No flaps, out of ground effect



(b) Flaps 20 deg, out of ground effect



(c) No flaps, in of ground effect



(d) Flaps 20 deg, in of ground effect

Figure A.10: NASA span-loader aircraft, lift coefficient in and out of ground effect with and without flaps deployed.

A.3 Aerofoil model validation

There were two components to the aerofoil model. The first was the solver used to generate tables of aerodynamic data for a given aerofoil section profile. This model is validated in Section A.3.1. The second component was the lookup routine which obtained data for a given Reynolds number. This model is discussed in Section A.3.2

A.3.1 NACA 6 series aerofoil

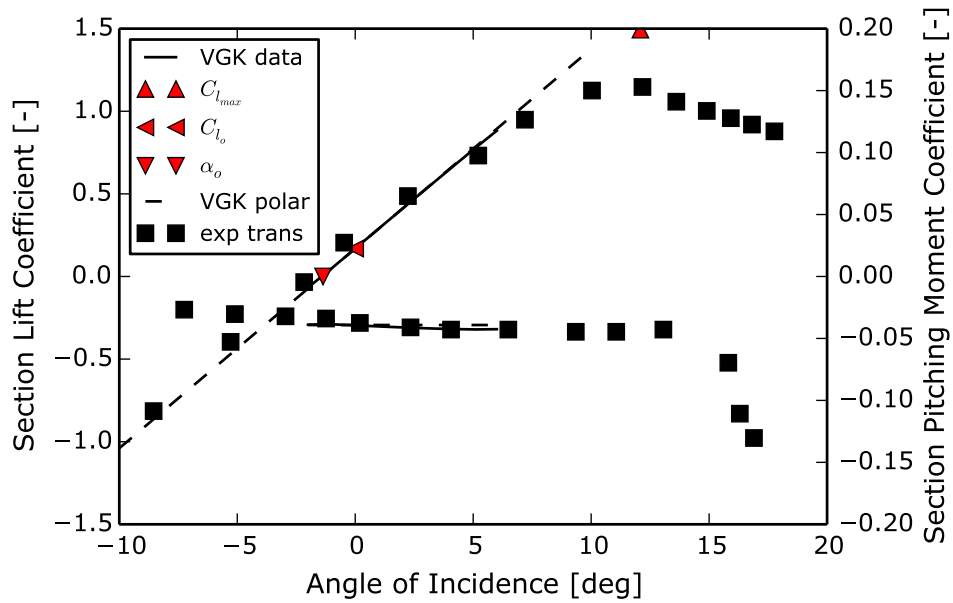
The VGK aerofoil performance model was used to predict the performance of a NACA 63212a=1 aerofoil at a Reynolds number of 6×10^6 . This aerofoil and Reynolds number was chosen so that the results could be compared to wind tunnel data [62].

Experimental data shown in Figure A.11 were shown for both a smooth aerofoil for an aerofoil where the flow was tripped to be turbulence near the leading edge. The VGK aerodynamic model could only predict the drag of an aerofoil with fixed transition points, set by default to 5% of the pressure and suction surfaces. This model was unable to predict the reduced drag on NACA 6 aerofoils due to extensive regions of laminar flow at low Reynolds numbers.

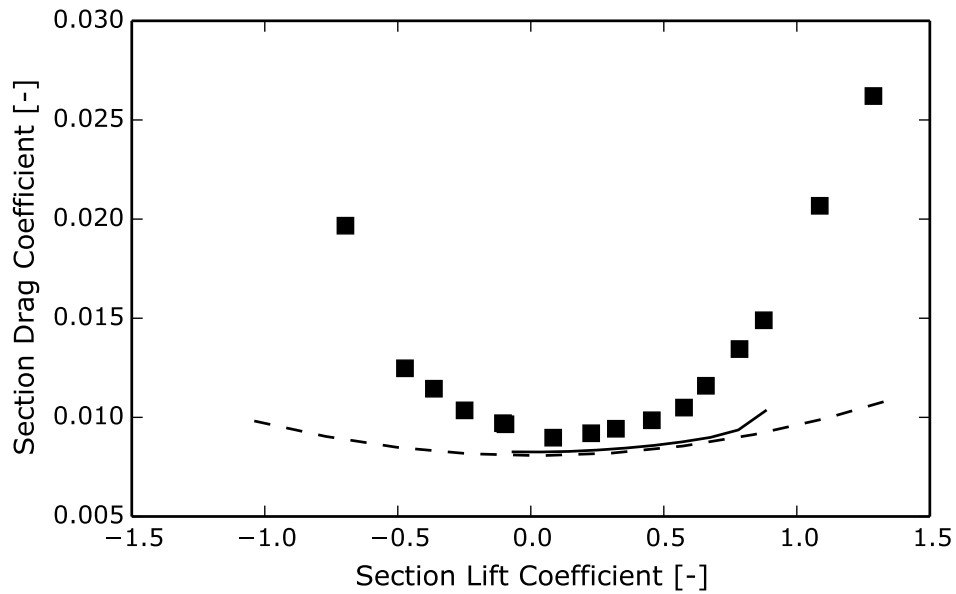
The maximum lift coefficient was estimated using an algorithm described in [94]. The maximum lift coefficient was over-predicted with respect to the data for the tripped flow but was predicted much more closely for the undisturbed flow. However, the drag coefficient was in closest agreement to the tripped flow. The VGK model showed a significantly reduced sensitivity of drag to the section lift coefficient, though it predicted the drag well about the design lift coefficient of 0.2.

The trend of section drag with lift for aerofoil section was represented by (6.4). The three unknown coefficients in this equations were obtained from the simulation data, shown as a solid line in Figure A.11b. The reconstructed drag polar using this data is shown as the dashed line in Figure A.11b and followed the the trend predicted by VGK closely.

Overall, the VGK model predicted the drag arising from fully turbulent flow over a NACA 6 aerofoil accurately for section lift coefficients close to the design point. The pitching moment, zero angle of attack lift and lift curve slope also showed close agreement to experimental data. The maximum section lift coefficient was more representative of the smooth aerofoil flow.



(a) Lift versus Angle of Attack



(b) Drag versus Lift

Figure A.11: Comparison of experimental and VGK results for a NACA 63212a=1 aerofoil.

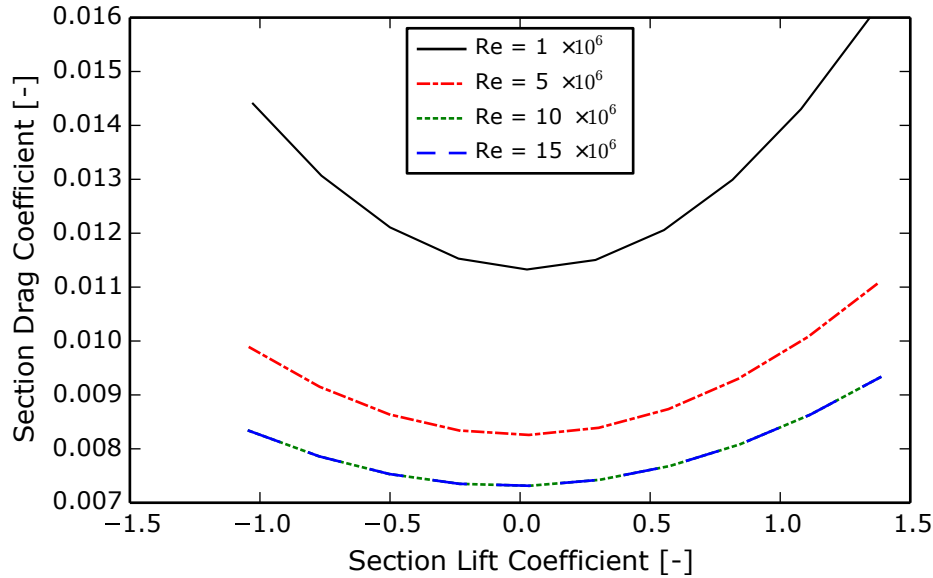


Figure A.12: Example of Reynolds number dependent polar results.

A.3.2 Reynolds number dependent polar

The VGK aerodynamic model was used to predict the trends in lift and drag of aerofoil sections at a range of Reynolds numbers. Unfortunately, lift and drag data for fully turbulence aerofoil sections were only available for a single Reynolds number so the VGK model could not be validated at other Reynolds numbers.

The VGK data were generated before running pyVORLIN simulations and the data corresponding to a given Reynolds number were obtained by linearly interpolating between the previously computed VGK data. A series of polars of section drag as a function of section lift are shown in Figure A.12. Since the data were for fully turbulent aerofoils, the drag increased with decreasing Reynolds number.

A.4 Weight model validation

The weight estimation module of pyACDT [82] was validated against published data for a range of transport aircraft. The aircraft ranged in size from regional jets to large twin-aisle transports. As-built data were obtained from Jane's All

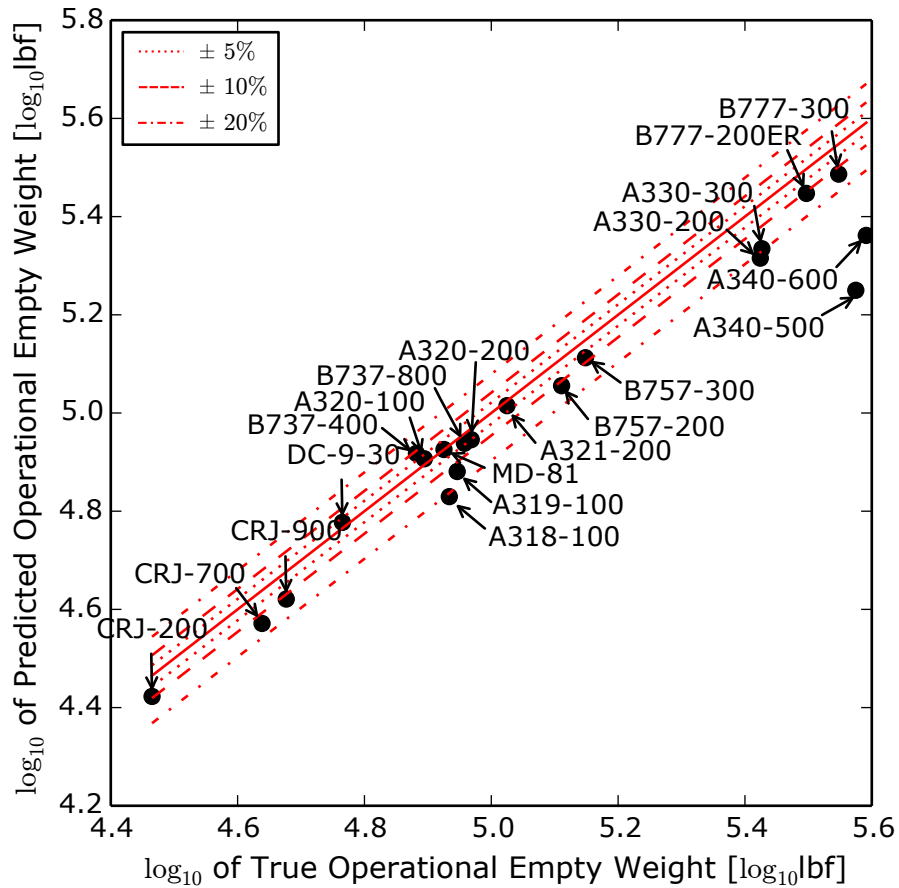


Figure A.13: Test of the pyACDT weight prediction model.

the World's Aircraft [64]. The weights module estimated the operating empty weight of the aircraft which included the aircraft structure and operational items but not the payload and fuel.

Though the weights module under-predicted the weight of some large transport aircraft by a significant margin, the accuracy for small transports of the size of the Bombardier CRJ aircraft was approximately $\pm 20\%$ which is acceptable accuracy for conceptual design purposes.

B Curriculum Vitae

Stephen Andrews

E-Mail: Stephen.Andrews@rmc.ca

Education

Royal Military College of Canada Kingston, Ontario

September 2011 – present Doctor of Philosophy

Thesis title: “Multidisciplinary Analysis of Closed, Nonplanar Wing Configurations for Transport Aircraft”

Advisor: Professor R.E. Perez

Royal Military College of Canada Kingston, Ontario

September 2007 – June 2009 Master of Applied Science

Thesis title: “Measurement and Computation of Losses from a Transonic Turbine Vane Cascade”

Advisor: Professor W. D. E. Allan and Dr. A. Mahallati

Queen’s University Kingston, Ontario

September 2003 – May 2007 Bachelor of Applied Science (Mechanical Engineering)

Graduated with first class honours

St. John’s-Kilmarnock School Breslau, Ontario

September 2000 – May 2003

Ontario Secondary School Diploma and Ontario Scholar

Experience

Los Alamos National Laboratory Los Alamos, New Mexico

Graduate Research Assistant, XCP-8 August 2015 – present

Royal Military College of Canada Kingston, Ontario

Teaching Assistant - Heat Transfer September – December 2014

Teaching Assistant - Aircraft Performance January – May 2014

Teaching Assistant - Fluids I September – December 2013

Teaching Assistant - Engineering Graphics January – May 2013

Lecturer - Engineering Graphics January – May 2012

Teaching Assistant - Fluids I January – May 2008

Teaching Assistant - Thermodynamics I September – December 2007

Research Assistant May – September 2007

MDS Aero-Support Corporation Ottawa, Ontario

Aerodynamicist September 2009 – June 2011

Queen's University
Research Assistant

Kingston, Ontario
May – September 2006

Academic Awards

- Mechanical and Aerospace Post Graduate Scholarship November 2012
- Milton Fowler Gregg V. C. Trust Fund Bursary November 2011
- Queen's University on Dean's Scholar 2003 – 2007
- Queen's University Entrance Scholarship September 2003

Publications

Articles Under Review:

- o **Andrews, S. A.** and Perez, R. E. Analytic Study of the Conditions Required for Longitudinal Stability of Dual-Wing Aircraft. *Proc IMechE Part G: J. Aerospace Engineering* (Submitted Oct 2015).

Journal Articles:

- o **Andrews, S. A.**, Perez, R. E. and Wowk, D. (2015) Wing weight model for conceptual design of nonplanar configurations *Aerospace Science and Technology* (43) pp 51-62.
- o **Andrews, S. A.** and Perez, R. E. (2013) Aerodynamic implications of gull's drooped wing-tips. *Bioinspiration & Biomimetics* (8)4.

Other refereed contributions:

- o **Andrews, S. A.** and Perez, R. E. (2015) Multidisciplinary Analysis of a Box-Wing Aircraft Designed for a Regional-Jet Mission. AIAA 2015-2793, *16th AIAA/ISSMO Multidisciplinary Analysis and Optimization Conference*, Dallas, USA.
- o **Andrews, S. A.** and Perez R. E. (2015) Parametric Study of Box-Wing Aerodynamic Design for Minimum Drag Under Stability and Maneuverability Constraints. AIAA-2015-3291, *33rd AIAA Applied Aerodynamics Conference*, Dallas, USA.
- o **Andrews, S. A.** and Perez, R. E. (2014) Stability and Control Effects on the Design Optimization of a Box-Wing Aircraft. AIAA-2014-2592, *14th AIAA Aviation Technology, Integration, and Operations Conference*, Atlanta, USA.
- o **Andrews, S. A.** and Perez, R. E. (2012) Sizing of a Short Range Civil Transport Aircraft Considering Aero-Structural and Stability Effects. AIAA 2012-1358288, *14th AIAA/ISSMO Multidisciplinary Analysis and Optimization Conference*, Indianapolis, USA.

-
- o **Andrews, S. A.**, Mahallati, A., Allan, W. D. and Benner, M. W. (2009) Experimental and Computational Investigation of the Mid-Span Flowfield in a Transonic Turbine Nozzle Cascade. ISABE-2009-1232, *19th International Symposium on Air Breathing Engines*, Montreal, Canada.
 - o Mahallati, A., Gostelow, J. P., **Andrews, S. A.**, and Carscallen, W. E. (2009) Measurement and Computation of Flowfield in Transonic Turbine Nozzle Blading with Blunt Trailing Edges. GT2009-59686, *ASME Turbo Expo*, Orlando, USA.
 - o **Andrews, S. A.** and Allan, W. D. (2008) Design of Streamwise Stagger Within a Pin-Fin Array to Minimize Pressure Loss. IMECE2008-66683, *ASME Congress*, Boston, USA.
 - o Allan, W. D. and **Andrews, S. A.** (2008) Experimental Investigation into the Influence of Varying Stagger on the Performance of a Pin-Fin Array. GT2008-50381, *ASME Turbo Expo*, Berlin, Germany.

Non-refereed contributions:

- o **Andrews, S. A.**, Perez, R. E. and Allan, W. D. E. (2015) The Drooped Wings of Gulls: Aerodynamic Optimum or Kinematic Constraint? *62nd CASI Aeronautics Conference and AGM*, Montreal, Canada. *Accepted for oral presentation.*
- o **Andrews, S. A.** and Perez, R. E. (2013) Design of Nonplanar Regional Jet Aircraft Considering Aero-Structural and Stability Couplings. *60th CASI Aeronautics Conference and AGM*, Toronto, Canada. *Accepted for oral presentation.*
- o **Andrews, S. A.** (2009). Measurement and Computation of Losses from a Transonic Turbine Vane Cascade. *Thousand Islands Fluids Meeting*, Gananoque, Canada.

Industrial reports:

- o Kabakov, Y. I., Finlay, S. and **Andrews, S. A.** (2011) ADD Altitude Engine Test Facility Aerodynamic Report. ER38020.4480.
- o **Andrews, S. A.** and Zitouni, G. (2010) CFD Validation Study of Free-jet Nozzles for ADD AETF. ER38020.4569.

Invited talks:

- o **Andrews, S. A.** "*Pin-Fin Heat Exchanger Research at the Royal Military College of Canada*". Presented to the National Research Council of Canada's Gas Turbine Aerodynamics and Combustion group, Nov 2007